Nano Scale Control On The Properties Of Perovskite Type Oxide

Thesis submitted for the degree of Doctor of Philosophy (Science)

In

Physics (Experimental)

by

Putul Malla Chowdhury

Department of Physics

University of Calcutta

August, 2019

.....

(*Putul Malla Chowdhury*)

Department of Condensed Matter Physics and Material Sciences,
S N Bose National Centre for Basic Sciences
Saltlake, Kolkata-700098, India.

.....

(*Prof. Arup Kumar Raychaudhuri*)

Dedicated to my family.....

Acknowledgement

I want to thank Prof. Arup Kumar Raychaudhuri, my supervisor for his constant support and encouragement during the course of this thesis work. Without his constant motivation it would not be possible to explain the physics coming from experiments. He is always being an inspiration for me.

I would like to thank my husband and senior Manotosh Chakravorty for his constant support and help in every hard situation. He always helped me in every complicated situation, which I have faced during experiments.

My Lab mates (seniors and juniors) are very co-operative. They need special thanks. I want to thank my friends and batch mates of S N Bose centre.

I want to thank my collaborators Dr. Barnali Ghosh Saha, Dr. S.D. Kaushik and Prof. V. Siriguri for their help in the sample preparation and structural analysis. In my early days of Ph. D Barnali di helped me lot to learned nanograined sample preparation.

Technical cell staffs especially Joy Bondopadhya helped me a lot during sample preparation. Finally I would like to thank my family for their constant support and encouragement.

I would like to thank CSIR-Govt. of India for fellowship.

Publications:

1. Stability of charge and orbital order in half-doped $Y_{0.5}Ca_{0.5}MnO_3$ nanocrystallites. Putul Malla Chowdhury, Barnali Ghosh, A. K. Raychaudhuri, S. D. Kaushik, V. Siruguri, *J Nanopart. Res*. **15**, 1585 (2013).

2. Resistance switching due to current driven oxygen motion in $La_{0.85}Sr_{0.15}MnO_3$ submicronstrip. Putul Malla Chowdhury, A. K. Raychaudhuri. (To be submitted).

3. A-site cation disorder dependent oxygen sensitivity of half doped manganite nanoparticle system of grain size 5 nm. Putul Malla Chowdhury, A. K. Raychaudhuri. (To be submitted).

4. Nanoscopic stoichiometry control of functional oxide nanoparticles by electro-chemical route. Putul Malla Chowdhury, A. K. Raychaudhuri. (To be submitted).

5. Oxygen diffusion study in perovskite oxide films near room temperature. Putul Malla Chowdhury, A. K. Raychaudhuri. (To be submitted).

Contents

List of figures:

Chapter 1

Chapter 2

Chapter 4

Chapter 5

Chapter 6

List of Tables:

Chapter 1

Introduction

Perovskite oxide manganites are interesting due to their strong coupling between electric, charge and orbital degrees of freedom. External perturbation (hole/electron doping, magnetic field, biaxial/uniaxial strain, hydrostatic pressure, internal pressure by changing cation radius, oxygen stoichiometry and size reduction of grain) can tune the ground state of these kind of oxides. These oxides have technological applications in solid oxide fuel cells, magnetic storage device, field effect transistors, spintronics and environmental applications as catalyst. The nano system has large surface to volume ratio. In addition often by making the manganites to nanometric regime (which we refer to as nano-manganites) one can also modify the electronic and magnetic interactions this can lead to tuning of the ground state. Few works have been done till today in the context of nano manganite. In this chapter we have given an overview of the research under going in the nano perovskite system and will place the thesis work in proper context.

1.1 Motivation

In the last few years nanomanganites (manganite nanoparticles and nanowires with diameter < 100 nm have attracted attraction to the research community due its interesting behaviour from its bulk counterpart [1-5]. The properties of nano manganite depend on a number of factors and are not properly understood till date. The most important question in this field is whether one can achieve control of physical properties of these materials at small scales ~ 100 nm or below. Two routes can be used to achieve such nano-level control: First is the control by size where one can synthesize nanocrystals of such oxides and study the Physical properties if it changes from bulk material. Second approach is to have control/variation of the composition and oxygen stoichiometry in nanoscales.

In this thesis we seek answer to some of the relevant questions that address to nanoscale modifications of physical properties of manganites:

(a) Can size reduction have strong effect on such systems that show robust charge and orbital ordering?
(b) Is it possible to electrochemically control the oxygen stoichiometry at room temperature without heating the sample?
(c) Is it possible to control oxygen stoichiometry locally by combining electrochemical oxidation along with lithographically fabricated structures?
(d) Can one in a controlled way migrate oxygen ions/vacancy by applying electric field and thus obtain control on its physical properties selectively?

Seeking answers to these questions built the main motivation of our work.

1.2 Basic Manganite and Nano-manganites

The parent compound crystallizes in $AMnO_3$ type perovskite structure which consists of a network of corner shared MnO_6 octahedra with the A – site cation situated at the centre of the cube (FIG.1.1). The ideal perovskite structure is cubic. Partial substitution of the trivalent A ion by divalent B ion ($A_{1-x}B_XMnO_3$) almost always leads to a distortion in the structure from its ideal cubic one. This distortion occurs due to a change in the average ionic size. This substitution also leads to the formation of a mixed valence state of Mn i.e. Mn^{3+} and Mn^{4+} in order to maintain charge neutrality of the system (e.g. $La_{1-x}^{3+}Ca_x^{2+}Mn_{1-x}^{3+}Mn_x^{4+}O_3^{2-}$). The degree of distortion in the unit cell is conveniently quantified by the "Goldsmith tolerance factor (*f*)" which when defined in orthorhombic. For a doped manganite, since there are two possible ions at the A site, the terms of the distance between the atoms in the lattice can be written as $f = r_{A-O}/\sqrt{2}r_{Mn-O}$.Thus, for an ideal cubic unit cell, f = 1(see FIG.1.1). An alternative (but equivalent) and more commonly used definition of f is that in terms of the ionic radii: $f = (r_A + r_O)/\sqrt{2}(r_{Mn} + r_O)$. In both cases, f has a simple geometric meaning and describes the degree of deviation of the lattice from the ideal cubic perovskite structure (for which f = 1, and the Mn-O-Mn angle is 180º). Rotations and deformations of the octahedra cause a lowering of the space group and $f < 1$. Thus, for $1 > f > 0.96$, the structure is rhombohedral, and for $f < 0.96$, the structure becomes orthorhombic. For a doped manganite, since there are two possible ions at the A site, the tolerance factor is defined as a density – weighted average of the individual tolerance factors.

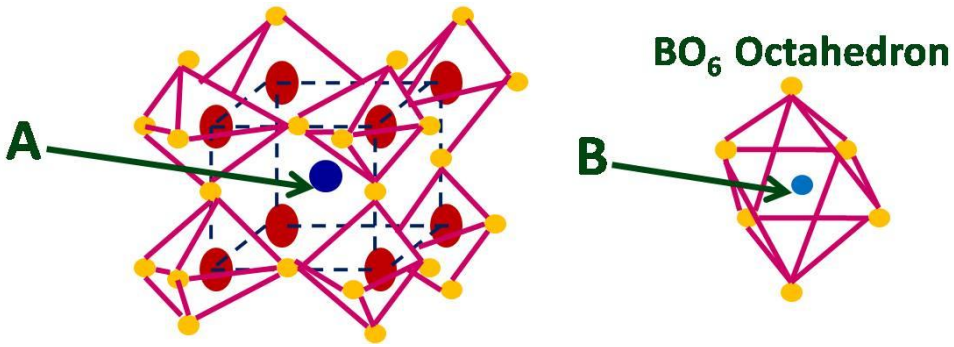

FIG.1.1. Ideal perovskite structure.

In perovskite manganites, the properties of the system are inherently linked with the degree of deviation from the ideal perovskite cubic structure. Thus, as the A radius is reduced, the MnO_6 octahedra rotate and tilt resulting in a decrease of the Mn-O-Mn bond angle (θ) from 180º. The hopping amplitude for carriers to move from one Mn site to the next also decreases as θ is reduced from 180º (for a 90º bond, the hopping involving a p-orbital at the oxygen is zero). As a consequence, as the tolerance factor decreases, the tendencies to charge localization increase due to carrier localization. The relevance of the crystal structure arises from the fact that in the manganites the three degrees of freedom – charge, spin and lattice – are coupled to each other [6-7]. In manganites structural, magnetic and electrical degrees of freedom interact with each other through "double exchange" mechanism and Jhan Teller interaction. Thus, a change in the structure (lattice) is reflected in a change in the magnetic state (spin degree of freedom) or electronic state (charge degree of freedom) of the system. Mixed valence magnanites exhibits colossal Magnetoresistance (CMR) phenomenon and magnetic phase transition [8].

Reduction in size enhances the contribution of surface states. There are uncompensated spins at the surface of the nano dimension which are comparable to the spins at the core for sufficiently small sizes. The magnetic interactions leads to different kind of ground state in the mixed valence $R_xA_{1-x}MnO_3$ (R = rare earth elements like La, A= Ca, Sr, Br etc.) oxides by changing the coupling between the spins of both Mn ions, carriers and lattice compared to the bulk counterpart [1, 3-4,9-10]. The grain size reduction in the mixed valance magnanite leads to the appearance of the Ferromagnetic metallic state by the suppression of antiferromagnetic insulating charged ordered ground state which exists in the bulk material [3-4, 9-11].

1.3 New Properties in manganite nano structure

Previous studies results some interesting observations in manganitesnano structures (nano particles, nano wires, nano tubes, thin films) which may have technological applications in magnetic, spintronic and microelectronic devices due to their unusual electron transport and magnetic properties [12]. Negative differential resistance has been observed in nanoscale filaments of manganites due to reversible metal to insulator transition [13]. Grain size reduction melts charge and orbital order state into ferromagnetic metallic phase [4]. Manganite oxide nanowires can be used in magnetic tunnel junction (MTJ) devices or lateral spin valves. For example using $La_{0.76}Sr_{0.33}MnO_3$ as ferromagnetic layer and $SrTiO_3$ as insulating layer MTJ devices was first developed by Lu et al [14] and Sun et al [15]. But the working temperature of all the manganite MTJ devices is below room temperature. This is a

major problem for commercial application of these devices. Manganite oxide thin films are very good oxygen ion conductors and they are used as interconnects in solid oxide fuel cells [16]. Later sections we discuss briefly the outcome of basic physics in manganite nano structures studied till date.

1.3 (a) Grain size reduction and Charge and orbital ordering

In recent years the tuning of the ground state properties of hole doped perovskite oxide manganites by grain size reduction have attracted much attention. The charge and orbital ordered state is favourable for 50 % hole doping with relatively narrow band width system such as $La_{0.5}Ca_{0.5}MnO_3$ [17], $Pr_{0.5}Ca_{0.5}MnO_3$ [18], $Pr_{0.5}Sr_{0.5}MnO_3$ [19], $Nd_{0.5}Sr_{0.5}MnO_3$ [20], $Nd_{0.5}Ca_{0.5}MnO_3$ [21], which is a quite stable phase in those compounds.

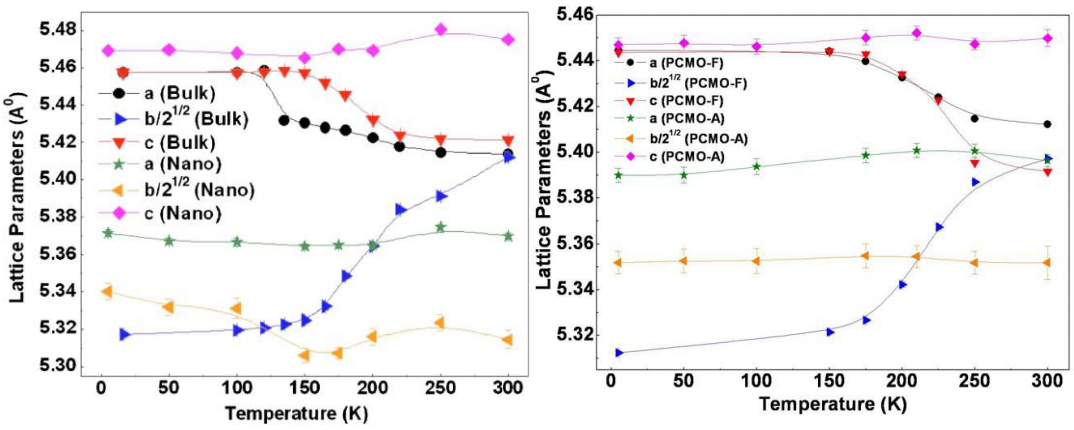

FIG. 1.2. Variation of lattice parameters of $La_{0.5}Ca_{0.5}MnO_3$ (LCMO) and $Pa_{0.5}Ca_{0.5}MnO_3$ (PCMO) nano particles (~15nm(±2) LCMO and ~15nm(±2) PCMO) and bulk samples(~3.6μm(±600nm) LCMO and ~ 3.3 μm(±500nm) PCMO) with respect to temperature (Reproduced from the reference [22] and [23] with permission).

It has been found that for half doped manganites (like $La_{0.5}Ca_{0.5}MnO_3$ [4], $Nd_{0.5}Ca_{0.5}MnO_3$ [24], $Nd_{0.5}Sr_{0.5}MnO_3$ [25], $Pr_{0.5}Ca_{0.5}MnO_3$ [26] etc.) the CO insulating state can be destabilized in to ferromagnetic metallic phase by only size reduction. For the nano system room temperature arrest of lattice parameter is observed which is shown in FIG.1.2. However the melting of CO state is higher for compounds of larger cation radius. There is no direct experimental evidence, which can explore the actual mechanism behind the observed nanometric effect. Sarkar et al. [4, 26] have explained the nanometric effect by structural changes which modify the magnetic and electronic structure by creating an equivalent hydrostatic pressure originating from surface tension. Although some reports exist in literature that describes the surface effect may be responsible for the experimental results [27, 28]. Recently theoretical investigation on $La_{0.5}Ca_{0.5}MnO_3$ [29] nano crystallites by DFT+DMFT calculations shows that effect of size reduction to be distinctively different from application of hydrostatic pressure. In case of $La_{0.5}Ca_{0.5}MnO_3$ nano crystallites the Ferromagnetic metallic(FM) state establishes at higher temperature 260K compared to $Pr_{0.5}Ca_{0.5}MnO_3$, which has FM state formation arises 100 K [27] with majority coexisting of COI state. Again only a small fraction of FM exists in $Pr_{0.5}Ca_{0.5}MnO_3$ nano crystallites compared to $La_{0.5}Ca_{0.5}MnO_3$ nano crystallites. Thus a general question arises for half doped manganites whether the formation of FM over COI state is predictable or not.

1.3.(b) Oxygen stoichiometry and its relevance in nano structures

The general formula for hole doped perovskite oxide manganite can be written as $A_{1-x}B_x(Mn^{3+})_{1-x+2\delta}(Mn^{4+})_{x-2\delta}O_{3-\delta}$where δ is the oxygen non-stoichiometry. Insertion of oxygen in the proper vacant sites of the samples reduces δ and increases effectively Mn^{4+} concentration in the samples which in turn enhances the hole doping in the samples. Oxygen concentration can tune the physical properties of manganites both in bulk and in nano systems. In this section we will discuss some recent published results tuning the ground state in manganite thin films. In this work of [30] a hidden ferromagnetic metal (FM-M) – antiferromagnetic insulator (AFM-I) transition is observed in $La_{0.5}Sr_{0.5}MnO_{3\pm\delta}$ films with thickness ~120nm in optimized oxygen content. This antiferromagnetic insulating phase is very much sensitive to the oxygen content. Oxygen content in the films was varied in a laser ablated CVD (chemical vapour deposition) system by varying atmospheric temperature (T_{atm}). In FIG.1.3 a phage diagram of LSMO with oxygen concentration was developed.

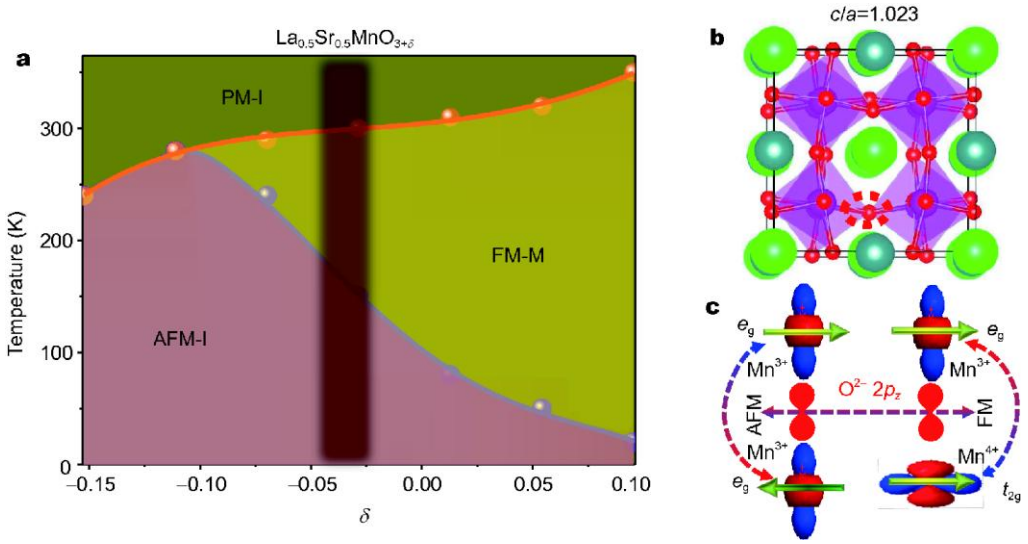

FIG. 1.3. Temperature-oxygen non stoichiometry (δ) phase diagram of $LSMO_{3+\delta}$ was reproduced in (a) PM-I is paramagnetic insulator. The Red rectangular area indicates the hidden metal-insulator transition. (b) LSMO perovskite structure with the red dotted circle denoting the position of an oxygen vacancy. (c) A schematic of the Mn–O–Mn orbital hybridization through double exchange and super exchange mechanism is shown (Reproduced from ref [30] with permission).

The Oxygen vacancy concentration (V_0) is successively reduced a hidden AFM-I to FM-I transition appears at low temperature. In FIG.1.3(b) it is shown that LSMO thin film suffers compressive strain ~1.7% Substrate (LAO) with lattice distortion of $c/a = 1.023$ which leads the compression of oxygen octahedra and results C-type AFM-I ground state. Different oxidation states of Mn are mediated by double exchange and supper exchange mechanism which is shown in FIG.1.3(c).

Oxygen vacancy tuning at a localized position can tune the resistance state in manganites. Recently the work of [31] where they have grown $La_{0.67}Ca_{0.33}MnO_3$ films on conducting $SrTiO_3$ (STO) substrate. In FIG. 1.4(a) resistive switching results on in-situ TEM measurement was given. They have applied a 100ms triangular voltage pulse between conducting STO substrate and metal tip, after the application of voltage pulse instantaneously STEM images were measured (FIG.1.4 (c)-FIG.1.4 (d)). For positive voltages as the

amplitude of the applied voltage pulse increases the sample goes to the high resistance state. This resistive switching process shows that it is directly related to the modification of lattice structure. In saturation state (2 in FIG.1.4 (a)), the original perovskite lattice shown in FIG.1.4 (c) completely transformed into an ordered superstructure (FIG.1.4(d)). This newly formed structure and corresponding high resistance state are stable unless a large enough negative voltage V_P is applied. This work shows how active control of oxygen vacancy can control the resistive state on well defined areas in manganite structure.

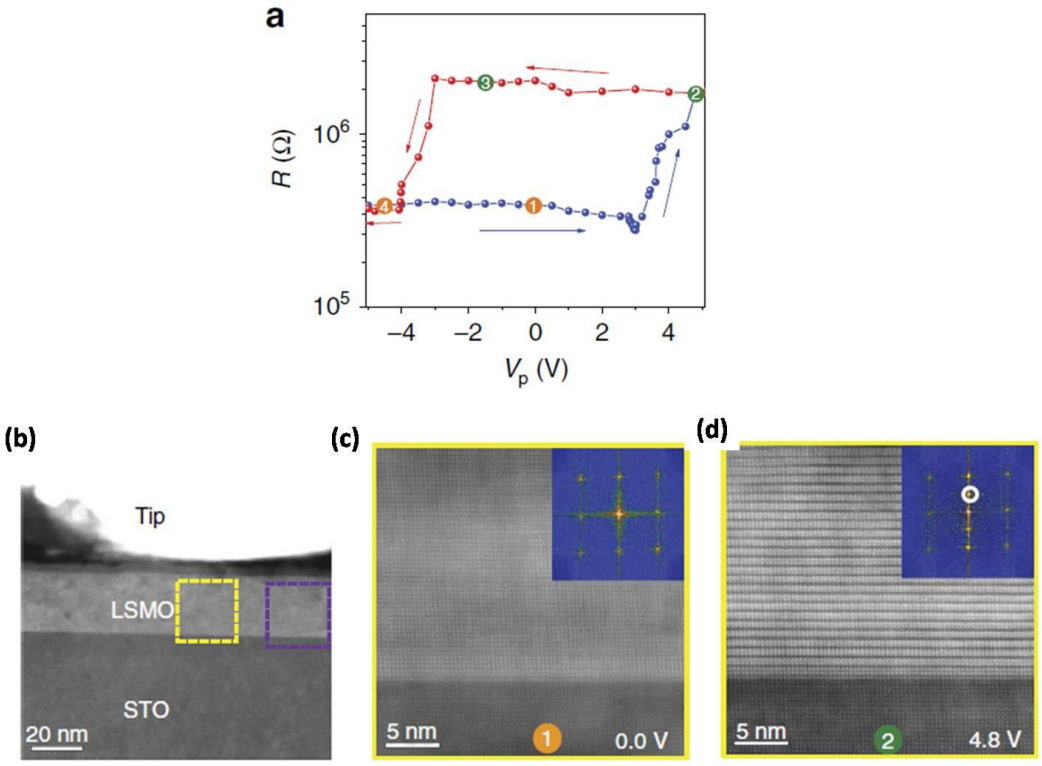

FIG. 1.4. Two-level resistive switching driven by structural phase transitions. (a) In situ TEM resistive switching curve for a LSMO film on top of a conducting $SrTiO_3$ substrate (b) STEM image between the metal tips and LSMO film (c) Ordered perovskite structure at low resistance state (d) In the high-resistance state a uniform structural transition to the brownmillerite phase is observed (reproduced from [31]).

1.4 Charge, orbital ordering and half-doped manganites

In the doped manganites, where Mn^{3+} and Mn^{4+} both present, the zener double exchange interaction prefers Mn^{3+} and Mn^{4+} ions to be next to each other, the local Jahn-Teller distortion of Mn^{3+} ions lift the degeneracy of e_g orbitals which impedes the hopping of e_g electrons to the undistorted nearest neighbour Mn^{4+}. Again the on sight coulomb repulsion between e_g electrons localizes the charge carriers at specific sites resulting an insulating state which opens a gap at the Fermi level, called **charge ordering**. The charge ordering in manganites is favored in 50:50 doping i.e, equal percentage of Mn^{3+} and Mn^{4+} ions where long range Mn^{3+} and Mn^{4+} chains observed. Again other compositions can also give charge ordered state depending on the interactions, temperature range and perturbations. The Jahn-Teller distortion of Mn^{3+} ions results an ordering of orbitals termed as **orbital ordering**. In the charge ordered manganites one particular spin ordering (**CE-type** as shown in Fig 1.5) is observed. The CE-type spin ordering is characterized by the ordering of Mn^{3+} and Mn^{4+} ions alternatively.

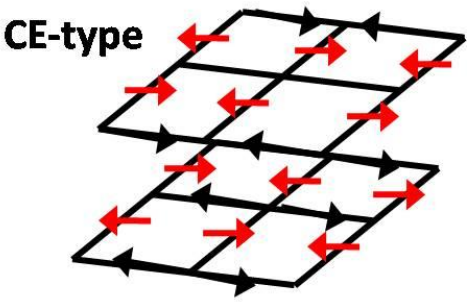

FIG.1.5. CE-type spin ordering.

In this ordering, in the ab-plane the Mn^{3+} and Mn^{4+} ions forms an alternative pattern along a zig-zag chain, the spins are ferromagnetically ordered within the Zig-Zag chain but the successive chains are antiferromagnetically coupled shown in FIG.1.5.

The stability of charge ordered phase directly related to the average radius of the A-site cation $< r_A >$. By reducing the $< r_A >$ the buckling of MnO_6 octahedra increases which reduces the one electron band width and increases the charge-order gap. Here given an example of variation of properties of manganates with A-site cation as Nd, Sm, Gd, Dy and Y [32].

TABLE 1.I. Value of charge ordering temperature is listed (reproduced from [32]).

Ln	$< r_A >$ **(A^0)**	**Lattice parameters (A^0)**			T_{CO} **(K)**		**Effect of H (6 T)**
		a	***b***	***c***	χ	**d log(ρ)/dT^{-1}**	
Nd	1.172	5.384	5.406	7.607	240	220	Yes
Sm	1.156	5.356	5.418	7.548	260	240	No
Gd	1.143	5.345	5.460	7.523	260	250	No
Dy	1.132	5.317	5.483	7.457	260	255	No
Y	1.127	5.305	5.495	7.445	260	250	No

The temperature variation of activation energy and magnetic susceptibility is shown below [32].

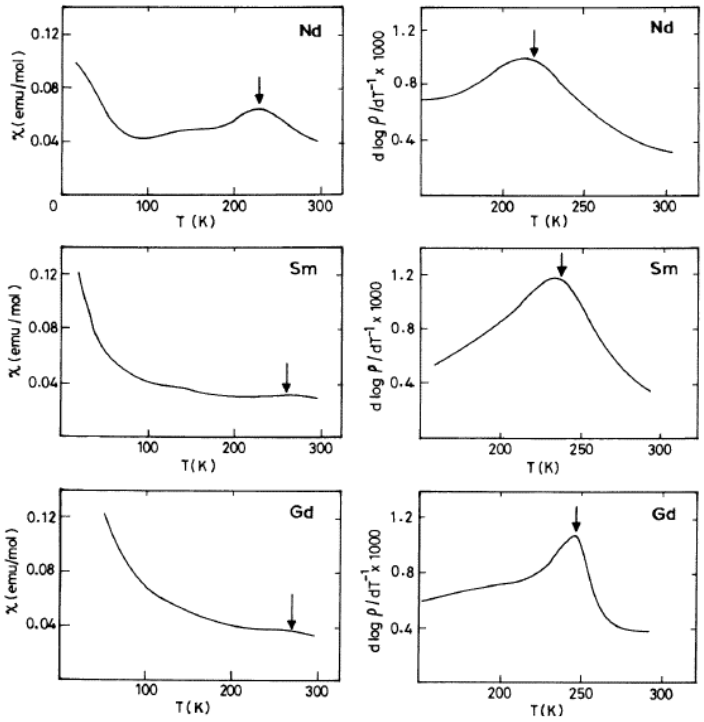

FIG. 1.6. The temperature variation of magnetic susceptibility and activation energy for conduction d(lnρ)/d(1/T) for $A_{0.5}Ca_{0.5}MnO_3$ (A = Nd, Sm, Gd) (reproduced from [32]).

From FIG.1.6 we can see that magnetic susceptibility shows a maximum around 240 K or 260 K due to charge ordering. The values of charge ordering transition temperature, T_{CO} obtained from susceptibility data arelisted in TABLE 1.I. Also the temperature variation of activation energy is shown in the FIG.1.6. These plots also show maximum due to charge-ordering. The maxima are in the range 220-255 K. The value obtained is somewhat smaller than the susceptibility data. We see that T_{CO} is higher for Sm, Gd, Dy and Y derivatives than for $Nd_{0.5}Ca_{0.5}MnO_3$. From this we can conclude that as the $< r_A >$ decreases charge order transition temperature increases. In FIG.1.7 a schematic diagram shows the dependence of charge order state on $< r_A >$ during cooling reproduced from [33].

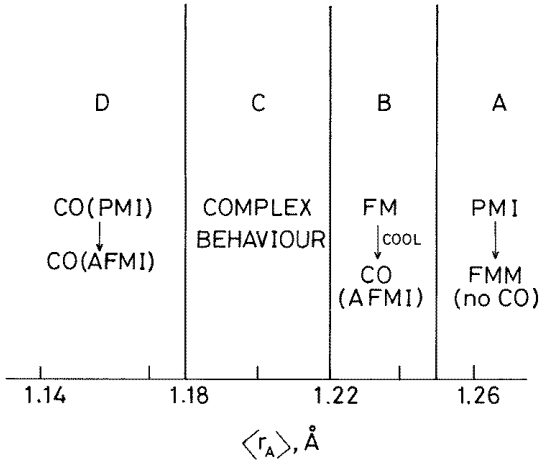

FIG. 1.7. Schematic phase diagram of rare-earth manganates showing different types of charge ordering effect with the variation in the average radius of the A-site cations. FMM, ferromagnetic metal; PMI, paramagnetic insulator; AFMI, antiferromagnetic insulator; CO, charge-ordered state (reproduced from ref [32]).

This diagram shows when $< r_A >$ is large in the region A the ferromagnetic metallic state is stable. For example $La_{0.5}Sr_{0.5}MnO_3$ with $< r_A >$ 1.244 A^0 does not show charge ordering. In the region B slightly smaller radius ferromagnetic state becomes unstable and transforms into antiferromagnetic charge ordered state on cooling as example $Nd_{0.5}Sr_{0.5}MnO_3$ with $< r_A >$ 1.236 A^0. When $< r_A >$ is very small the does not exhibit ferromagnetism and gives rise to insulating charge order ground state (e. g , $Pr_{0.7}Ca_{0.3}MnO_3$ with $< r_A >$ ~ 1.179 A^0) in region D. In region C, T_{CO} approaches to T_C, shows complex behavior, for example $Nd_{0.5}Ca_{0.5}MnO_3$ ($< r_A >$ ~ 1.2 A^0) exhibits coexistence of ferromagnetism and charge ordering in a narrow temperature range. In this region there is strong competition between ferromagnetism and charge ordering. For further reduction of $< r_A >$ (as in $Nd_{0.25}La_{0.25}Ca_{0.5}MnO_3$ with $< r_A >$ ~ 1.19 A^0) shows novel re-entrant ferromagnetic transition from an incipient CO state on cooling [34].The $Y_{0.5}Ca_{0.5}MnO_3$ have smallest $< r_A >$ with 1.127 A^0. Charge –ordering also depends on the doping concentration. When x = 0.5 charge ordering is more robust due to equal amount of Mn^{3+} and Mn^{4+} amount. For other concentrations charge ordering also observed. For example, charge ordering is observed in $Nd_{1-x}Sr_xMnO_3$ only for x close to 0.5 and charge ordering disappears for x < 0.48 and x > 0.52.Again for reduced band-width perovskites like $Pr_{1-x}Ca_xMnO_3$ charge ordering is observed in a much broader range of x.

1.5 Phase diagram of $La_{1-x}Sr_xMnO_3$ and $La_{1-x}Ca_xMnO_3$

The parent $LaMnO_3$has orthorhombic Pbnm structure at room temperature. Orbital ordering (OO) due to corporative John Teller effect is present in this system. A structural phase transition occurs at temperature 780 K and above this temperature OO phase vanishes. Below the Neel temperature 140 K the Antiferromagnetic insulating (AFI) phase is stable.

The doping of divalent compound Sr^{2+} in the system changes the oxidation state of some Mn ions from Mn^{3+} to Mn^{4+} and introduces holes in the e_g level. The carriers can hope through intermediate oxygen ions of Mn^{3+}-O-Mn^{4+} bridge. In FIG.1.8 the phase diagram of $La_{1-x}Sr_xMnO_3$ system was shown [35]. For 0.16 > x > 0.08 the system is ferromagnetic insulator. In the region 0.3> x > 0.16 ferromagnetic metallic phase appears. For x > 0.3 the system becomes ferromagnetic even at room temperature. Changing the oxygen concentration in the system results similarly as hole doping. For example in the work of shiozaki et. al. [36] they have extensively studied the electronic and structural phase transitions of LSMO single crystal samples after oxygen annealing. Before oxidation the resistivity of the samples shown in FIG.1.9(a) follows the phase diagram of LSMO.

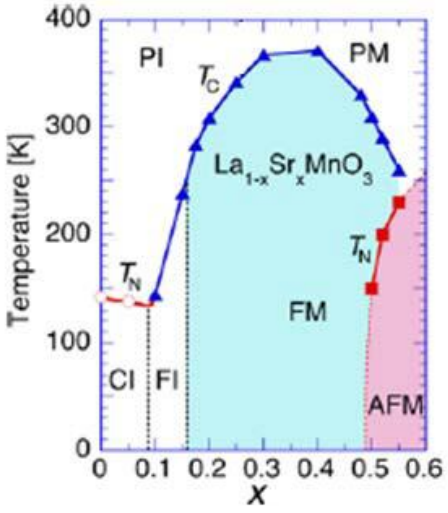

FIG.1.8. Phase diagram of LSMO-ordered state (reproduced from [35]).

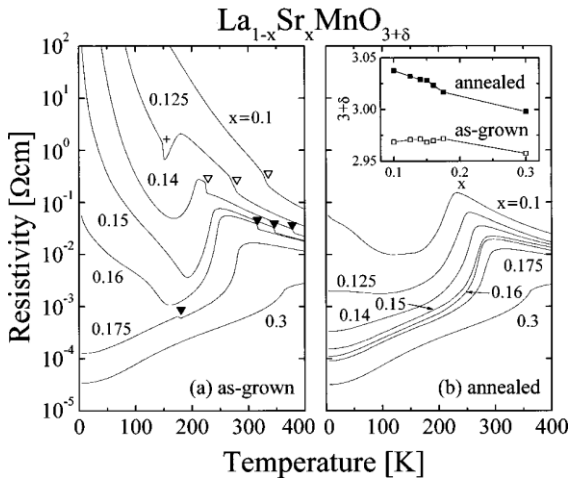

FIG.1.9. Resistivity versus temperature curve for (a) as grown and (b) oxidized single crystal samples of LSMO (reproduced from [36]).

The filled triangles of FIG. 1.9 (a) represents rhombohedral (R) to orthorhombic (O*) transition and open triangles denotes O*−O' phase transition with charge ordering. After oxidation all of these transitions vanish in FIG.1.9 (b).

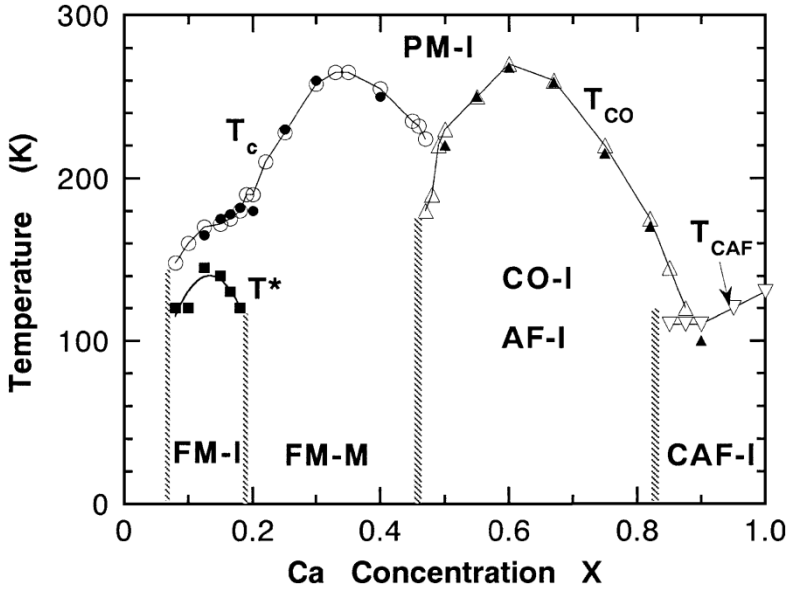

FIG. 1.10. Phase diagram of $La_{1-x}Ca_xMnO_3$compound (reproduced from [37]).

In FIG.1.10 the phase diagram of LCMO series is shown. For $0.1 > x > 0$ the system is antiferromagnetic insulator. Within the range of $0.2 > x > 0.1$ ferromagnetism sets in with insulating nature. For $0.5 > x > 0.2$ ferromagnetic metallic phase exists. Charge and orbital order phase arises from 50% doping accompanied with antiferromagnetic insulating state up to $x < 0.88$ and for $x > 0.88$ canted antiferromagnetic phase starts growing. For this compound $x = 0.33$ composition have highest ferromagnetic transition temperature ($T_C \sim 270$ K) as x increases or decreases from this optimal concentration T_C decreases.

1.6 Oxidation of manganites

The general formula for hole doped perovskite oxide manganite can be written as $A_{1-x}B_x(Mn^{3+})_{1-x+2\delta}(Mn^{4+})_{x-2\delta}O_{3-\delta}$ where δ is the oxygen non-stoichiometry. Insertion of

oxygen in the proper vacant sites of the samples reduces δ and increases effectively Mn^{4+} concentration in the samples which in turn enhances the hole doping in the samples. Depending concentration of hole doping in the phase diagram the resistance of the samples responses after oxidation. For example Previously $La_{1-x}Sr_xMnO_{3\pm\delta}$ samples are prepared after annealing single crystals of $La_{1-x}Sr_xMnO_{2.968}$ in 900 ^{0}C for 1000 h at oxygen partial pressure 1 atm [23, 36]. It can be seen from FIG.1.9 that the resistivity of ($x \leq 0.16$) is more drastic from other compositions of Sr and attains metallic feature in resistivity. The as grown sample of ($0.14 \leq x \leq 0.16$) exists in metal to insulator (IM) phase boundary. Oxygen content can greatly affect the system at the IM phase boundary.

Methods for oxidation

Generally two kinds of method are available to change the oxygen concentration in any oxide sample. One is thermal and another is electrochemical oxidation and reduction.

Below we discuss briefly the advantages and disadvantages of both the methods.

(i)Thermal

The effect of oxygen non-stoichiometry on the electric transport properties of these kind of oxides for temperatures reasonably high (above 500 ^{0}C) was studied [38−42]. In most of those cases the oxygenation was done by heat treatment along with varying the oxygen partial pressure in the chamber. The oxygen diffusion at those high temperatures occurs at a very fast time scale(~ few seconds to few minutes) which is completely uncontrolled and after the oxygenation process the samples (film, bulk) became homogeneously oxygenated [38−42].

Advantage:

The main advantage of this process is that, it is faster in time scale as the diffusivity of oxygen increases at high temperature.

Also large amount of samples can be homogeneously oxidized by this process.

Disadvantages:

This process leads to grain growth so study of oxygen concentration change in nano grained samples is not possible by using this method.

The precise control on the amount of oxidation/reduction is not possible.

(ii) Electrochemical

Using heat treatment method study of oxygen diffusion at room temperature is impossible (this process needs high temperature > 500 ^{0}C).Oxygen incorporation by electrochemical method can be done at room temperatures. Since the diffusion length at room temperature is small, we can make regions locally that have “oxygen crowding”. As the temperature is low (300 K), the oxygen ions will not diffuse very fast in the sample and it is possible to study the dynamics of oxygen motion in details.

While electrochemical oxidation has been used in the past on $La_{0.2}Sr_{0.8}CoO_{3-\delta}$ [43], $La_4Ni_3O_{10}$ [44], $La_2CuO_{4+\delta}$ [45] oxides to control oxygen but using it as a controlled source to do diffusion study has not been done. The $La_{0.85}Sr_{0.15}MnO_3$ sample exists in the insulator to

metal phase boundary. The oxygen sensitivity of these kinds of oxides is a very important issue. There is no any detailed study from my knowledge in the variation of oxygen stoichiometry in nano perovskite systems.

Advantage:

Main advantage of this method is that is possible to do the stoichiometry modification at room temperature and precisely.

By using this method, since it involves no heating, grain sizes of nano particles are retained.

Oxygen concentration change at definite spatial location can be possible by using this method. Precise control on the amount of stoichiometry change can be done as the electrochemical current and Faraday laws allow precise amount of oxygen amount incorporated in the system.

Disadvantages:

The main disadvantage of this process is that, it is slower in time scale as the diffusivity of oxygen decreases at low temperature (near room temperature).

1.7 Work done in this thesis

Innovative way to control oxygen stoichiometry in nanoscale has given us a handle to investigate how control of oxygen stoichiometry in such small scale materials leads to modifications of their physical properties. In particular, in this thesis we have investigated stability of certain long range order in manganties upon size reduction (reduction of crystalite size to sub-micron or nanometer length scale) – which is an important outcome of control of physical properties by size reduction.
The thesis focused on the following experiments and the important results achieved have been summarized:

(a) Development of the method for electrochemical oxidation/reduction that allows precise oxygen stoichiometry control at room temperature.

(b) Reversible electrochemical oxidation/reduction temperature in nanocrystal (~ 4 nm grain diameter) of optimally doped $La_{0.67}Ca_{0.33}MnO_{\delta}$ (with $\delta \approx 3$) and thereby control of magnetization and ferromagnetic transition. Proof of concept has been established that in such system electrochemical method can control δ from 2.74 to 3.20 at room temperature without any need for heating. Such electrochemical oxidation/reduction process at room temperature changes both the magnetization and also the transition temperature by as much as 16 K.

(c) Size reduction leads destabilization of charge ordering state in nanocrystals (~ 5 nm grain diameter) of half doped manganites $A_{0.5}Ca_{0.5}MnO_3$(where A = Y, Sm, Nd, Pr, La) leading to onset Ferromagnetism (FM). It has been shown that FM state and electrical resistivity can be controlled by electrochemical control of the stoichiometry in such nanometric systems. The resulting changes depend on the extent of A site cation disorder as measured by the size variance of the cationic radii.

(d) To establish that oxygen created by electrochemical oxidation in a part of the sample can be made to diffuse by application of a field and thus have spatial control on

oxygen diffusion. This was tested in a submicron strip of low hole doped $La_{0.85}Sr_{0.15}MnO_3$, where diffusion of oxygen by a field leads to reduction of resistance as the hole concentration increases. This establishes yet another way of nanoscopic control of stoichiometry where oxygen can be transported from one region of the sample to another and this have a nanoscopic control of the oxygen stoichiometry.

(e) The charge and orbital ordering (COO) of $Y_{0.5}Ca_{0.5}MnO_3$ (end member of $A_{0.5}Ca_{0.5}MnO_3$ series) is very robust (cannot be destabilized at high magnetic field up to 20 T). The important phenomena observed here is that in the nanocrystallite (~ 75 nm grain diameter) of $Y_{0.5}Ca_{0.5}MnO_3$ the COO phase is melted and ferromagnetism (FM) which coexist with antiferromagnetism (AFM) arises.

The thesis is organized in the following chapters:

Chapter2: Experimental techniques

Chapter3: Nanoscopic control of stoichiometry of oxide nanoparticles of $La_{0.67}Ca_{0.33}MnO_3$ using electro-chemical route and the resulting physical and structural properties

Chapter4: Dependence of physical properties of half-doped manganite nanoparticles (average diameter:~5nm) on electrochemically controlled Oxygen stoichiometry: Role of cation A-site disorder

Chapter5: Migration of Oxygen by electric field in submicron strips of $La_{0.85}Sr_{0.15}MnO_3$

Chapter6: Stability of charge and orbital order in nanocrystals of half-doped manganite $Y_{0.5}Ca_{0.5}MnO_3$

Chapter7: Conclusion

Annexure: Relaxation dynamics of oxygen in manganites after electrochemical oxidation

References:

1. Lei Li, Lizhi Liang, Heng Wu and Xinhua Zhu, *Nanoscale Research* Letters.**11**, 121 (2016).
2. Yufeng Tian, Saidur Rahman Bakaul and Tom Wu, *Nanoscale*, **4**, 1529 (2012).
3. Tapati Sarkar, A. K. Raychaudhuri, A. K. Bera and S. M. Yusuf, *New J. Phys*. **12**, 123026 (2010).
4. Tapati Sarkar, Barnali Ghosh and A. K. Raychaudhuri, *Phys. Rev. B*, **77**, 235112 (2008).
5. K. Shantha Shankar and A. K. Raychaudhuri, *J. Mater. Res*. **21**, 27 (2006).
6. C. N. R. Rao and B. Raveau, (eds) *Colossal magnetoresistance, charge ordering and related properties of manganese oxides*. *Singapore: World Scientific* (1998).
7. B. Raveau, *Phil. Trans. R. Soc. A*. **366**, 83 (2008).
8. S. Jin, T. H. Tiefel, M. McCormack, R. A. Fastnacht, R. Ramesh and L. H. Chen, *Science*. **264**, 413 (1994).
9. S. K. Giri, A. Poddar and T. K. Nath, *Aip Adv*, **1**, 032110 (2011).
10. S. S. Rao, S. Tripathi, D. Pandey and S. V. Bhatt, *Phys. Rev. B*, **74**, 144416 (2006).
11. Barnali Ghosh, V Siruguri, A K Raychaudhuri and Tapan Chatterji, *J. Phys.: Condens. Matter*. **26** 025603 (2014).
12. L. Z. Liang, H. Wu, X. H. Zhu, *Nanoscale Res. Lett*. **9**, 325 (2014).
13. T. Wu and J. F. Mitchell, *Phys. Rev. B*. **74**, 214423 (2006).
14. Yu Lu , X. W. Li, G. Gong, G. Xiao, A. Gupta, P. Lecoeur, J. Z. Sun, Y. Y. Wang and V. P. Dravid, *Phys. Rev. B*. **54**, R8357 (1996).
15. Y. Lu , X. W. Li, G. Gong, G. Xiao, *Appl. Phys. Lett*. **69**, 3266 (1996).
16. San Ping Jiang, *J Mater Sci*. **43**, 6799 (2008).
17. P. G. Radaelli, D. E. Cox, M. Marezio and S.W.Cheong, *Phys. Rev. B*. **55**, 3015 (1997).
18. S. Mori, T. Katsufuji, N. Yamamoto, C. H. Chen and S. W. Cheong, *Phys. Rev. B*. **59**, 13573 (1999).
19. R. Kajimoto, H. Yoshizawa, Y. Tomioka and Y. Tokura, *Phys. Rev. B*. **66**, 180402(R) (2002).
20. H. Kawano, R. Kajimoto, H. Yoshizawa, Y. Tomioka, H. Kuwahara and Y. Tokura, *Phys. Rev. Lett*. **78**, 4253 (1997).
21. T. Vogt, A. K. Cheetham, R. Mahendiran, A. K. Raychaudhuri, R. Mahesh and C. N. R. Rao, *Phys. Rev. B*. **54**, 15303 (1996).
22. Tapati Sarkar, *Tuning of ground state and phase transitionin complex oxide nanomaterials*, Thesis submitted at S. N. Bose National Centre for Basic Sciences, Kolkata (2009).
23. Tapati Sarkar, A. K. Raychaudhuri and Tapan Chatterji, *Applied Physics Letter*. **92**, 123104 (2008).
24. L. Liu, S. L. Yuan, Z. M. Tian, X. Liu, J. H. He, P. Li, C. H. Wang, X. F. Zheng and S. Y. Yin, *J. Phys. D: Appl. Phys*. **42**, 045003 (2009).
25. S. Kundu, A. Das, T. K. Nath, A. K. Nigam, *J.Magnetism and Magnetic materials*. **324**, 823 (2012).
26. Tapati Sarkar, P. K. Mukhopadhyay, A. K. Raychaudhuri and Sangam Banarjee, *J. Appl. phys*. **101**, 124307 (2007).
27. Z. Jirak, E. Hadova, O. Kaman, K. Knizek, M. Marysko and E. Pollert, *Phys Rev. B*. **81**, 024403 (2010).
28. S. Dong, F. Gao, Z. Q. Wang and J. M. Liu, *Appl. Phys. Lett*. **90**, 082508 (2007).
29. Hena Das, G. Sangiovanni, A. Valli, K. Held and T. Saha-Dasgupta, *Phs. Rev. Lett*. **107**, 197202 (2011).
30. Chuangye Song, Iftikhar Ahmed Malik, Menglei Li, Qinghua Zhang, Lichen Wang, Jing Wang, Rongyan Chen, Renkui Zheng, Shuai Dong, Lin Gu, Wenhui Duan, Ce-Wen Nan and Jinxing Zhang, *Science China Materials*. **62**, 577 (2018).
31. Lide Yao, Sampo Inkinen and Sebastiaan van Dijken, *Nature Communications*. **8**, Article number: 14544 (2017).

32. Anthony Arulraj, P. N. Santhoshy, R. Srinivasa Gopalan, Ayan Guha, A. K. Raychaudhuri, N. Kumar and C. N. R. Rao, *J. Phys.: Condens. Matter*. **10**, 8497 (1998).
33. Anthony Arulraj, R. Gundakaram, Amlan Biswas, N. Gayathri, A. K. Raychaudhuri and C. N. R. Rao, *J. Phys.: Condens.* Matter. **10**, 4447 (1998).
34. Anthony Arulraj, Amlan Biswas, A. K. Raychaudhuri and C. N. R. Rao, *J. Phys.: Condens.* Matter. **12**, L101 (2000).
35. Y. Tokura, *Rep. Prog. Phys.* **69**, 797 (2006).
36. R. Shiozaki, K. Takenaka,Y. Sawaki and S. Sugai, *Phys. Rev. B.* **63**, 184419 (2001).
37. Hiroyuki Fujishiro, Tetsuo Fukase and Manabu Ikebe, *Journal of the Physical Society of Japan*. **70**, 628 (2001).
38. H. Zhang, X. Yao, X. H. Zeng, *Phys. Stat. Sal*. *(a)201*. **10**, 2305 (2004).
39. L. Malavasi, G. Flor, *J. Phys. Chem B.* **107(50)**, 13880 (2003).
40. S. Kittelberger, O. M. Stoll and R. P. Huebener, *Supercond. Sci. Technol*. **11**,744 (1998).
41. K. Yamamoto, B. M. Lairson, J. C. Bravman and T. H. Geballe, *J. Appl. Phys.* **69**, 7189 (1991).
42. K. N. Tu, N. C. Yeh, S. I. Park and C. C. Tsuei, *Phys. Rev. B.* **39**, 304 (1989).
43. V. Pralong, V. Caignaert, S. Hebert, C. Marinescu, B. Raveau and A. Maignan, *Solid State Ionics*. 177, 815 (2006).
44. M. D. Carvalho, A. Wattiaux, J. M. Bassat J. C. Grenier, M. Pouchard, M. I. da Silva Pereira and F. M. A. Costa, *J Solid State Electrochem*. **7**, 700 (2003).
45. H. H. Feng, Z. G. Li, P. H. Hor, S. Bhavaraju, J. F. Di-Carlo and A. J. Jacobson, *Phys. Rev. B, (Rapid communications).* **51**, 22 (1995).

Chapter 2

Sample preparation and experimental techniques

During the course of this thesis work certain sample preparation, characterisation and physical property measurement techniques are used. In this chapter we give a brief overview of these experimental techniques. The samples were prepared by techniques like chemical solution deposition. Pulsed laser deposition (PLD) was used for deposition of films. One of the important technique was developed during the work is electrochemical oxidation/reduction. For lithography work we used Optical lithography, Electron Beam Lithography (EBL) and Focussed Ion Beam (FIB) milling. For characterisation tools like scanning electron microscopy (SEM), X-ray diffraction (XRD), energy dispersive X-ray analysis (EDX), iodometric titration were used. Electrical resistance measurement was done using a 4-probe technique. Magnetic property measurements were done using vibrating sample magnetometer (VSM) and superconducting quantum interface device (SQUID).

2.1.Sample preparation

All the samples used in this thesis were prepared by us.

The list of the samples which were used in this thesis work are given below,

(i) $Y_{0.5}Ca_{0.5}MnO_3$ bulk (grain size > 1 μm) and nanograined (grain size ~ 75 nm)

(ii) $A_{0.5}Ca_{0.5}MnO_\delta$ (grain size ~ 5 nm), where A= Y, Sm, Nd, Pr, La and x = 2.95−3.20

(iii) $La_{0.67}Ca_{0.33}MnO_\delta$ (grain size ~ 4 nm), where x = 2.74−3.20

(iv) $La_{0.85}Sr_{0.15}MnO_3$ sub-micronstrip of width 340 nm and 740 nm

(v) Film of $Y_{0.5}Ca_{0.5}MnO_3$ (thickness ~ 300 nm) and $La_{0.85}Sr_{0.15}MnO_3$ (thickness ~ 750 nm)

2.1.1. Chemical solution deposition (CSD)

We adopted Chemical solution deposition technique to prepare the nanoparticles used in this thesis work [1]. This is basically a modified polymeric precursor synthesis route. The essential steps involved in this process are shown schematically in FIG. 2.1. Here pure phase manganite nanoparticle samples have been prepared at temperatures as low as 600 ^{0}C and the minimum particle size of the samples used in this thesis work was ~ 4 nm. The particle size of the samples was controlled by the furnace temperature and the annealing time. The water/ethylene glycol ratio was also an important factor.

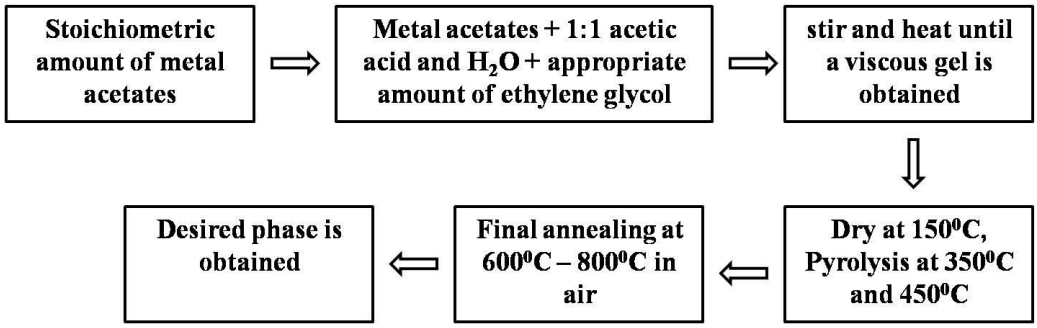

FIG. 2.1. Schematic diagram of pervoskite nanoparticle sample preparation.

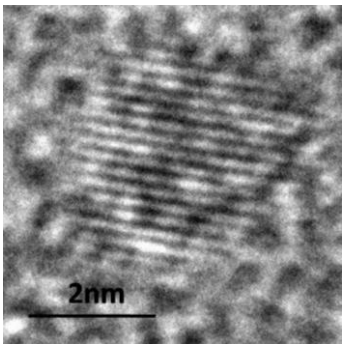

FIG. 2.2. TEM image of the $Y_{0.5}Ca_{0.5}MnO_3$ nanoparticle of grain size ~ 5 nm.

2.1.2. Pulsed Laser deposition (PLD)

PLD is widely used to prepare oxide thin films. All the films used in this thesis work are prepared in pulsed laser deposition chamber at S N Bose National Centre for Basic

Sciences. A schematic diagram of PLD unit is given in FIG.2.3. High power pulsed laser beam is focussed on the rotating target material in a chamber. This PLD unit delivers maximum 700 mJ power at wave lengths of 193 nm (ArF) and 248nm (KrF) with the maximum repetition rate of 10 Hz. Forward directed plasma plume of the target reaches the heated substrate and gets deposited on it to form the desired film sample. Oxygen gas is used in the chamber during deposition.

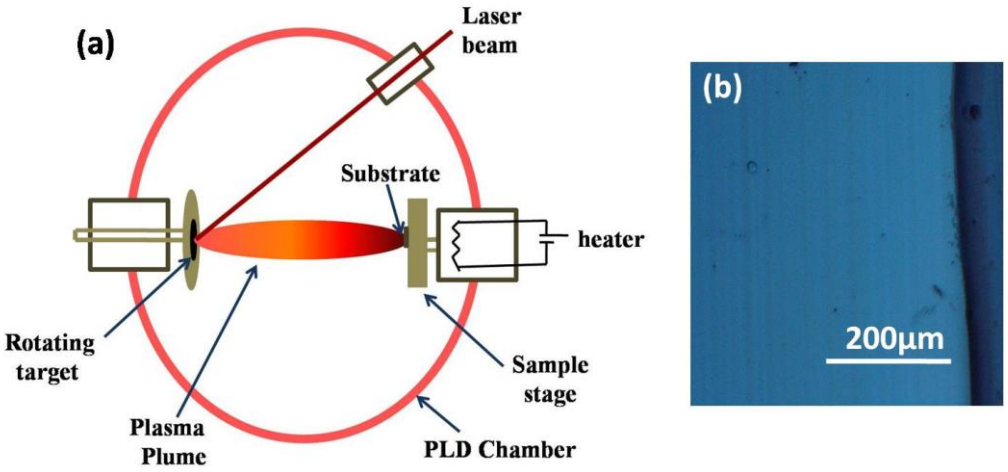

FIG. 2.3. (a) Schematic diagram of PLD unit (b) Optical microscope image image of $La_{0.85}Sr_{0.15}MnO_3$ film grown on $LaAlO_3$ substrate.

As an example the films of $La_{0.85}Sr_{0.15}MnO_3$ prepared in this thesis were grown on (100) oriented LAO substrates from stoichiometric targets. The chamber oxygen pressure was maintained during the deposition and cooling process at 10^{-1} mbar. The fluence of 1.8 J/cm^2 was used. The optimized shot frequency was 3 Hz and the target rotation frequency was 20 rpm. The optimized substrate temperature was 700 ^{0}C and the substrate was pre-annealed for 1 hrs before deposition. After deposition it was post annealed for 5 hrs. We have cooled the sample very slowly (0.5 ^{0}C/min) to avoid any abrupt crack developing in the sample.

2.1.3. Thermal evaporation

It is a very popular technique to make metal films and electrical contact pads. Here we use a chamber with air pressure $<10^{-6}$mbar. A molybdenum or tungsten boat inside the chamber was used as the source. The ingot of the film/sample material is placed on the boat. The substrate is placed above the boat at a distance, maintain a distance from boat. A substrate heater is attached to the substrate.

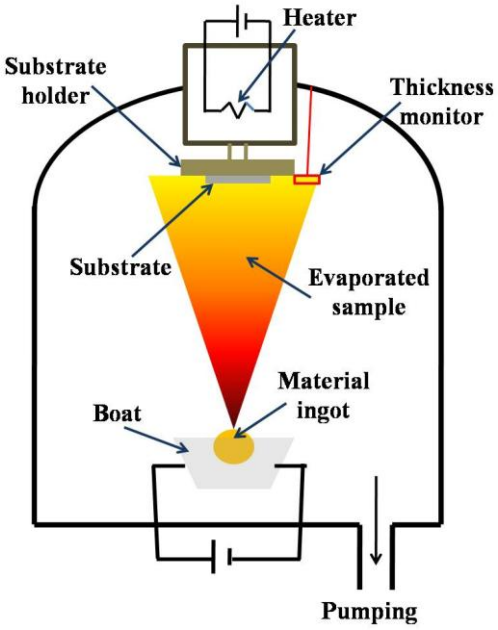

FIG. 2.4. Schematic diagram of thermal evaporation technique.

We used thermal evaporation process to make electrical contact pads of Au/Ag. We also prepared Al films on $LaAlO_3$(100) substrate at ~ 10^{-7}mbar chamber pressure for the preparation of high temperature lithography mask to prepare LSMO microstrips. The detail of this sample preparation will be discussed in section 2.1.4.

2.1.4. Integrated lithography

An integrated lithographic root was developed to make the sub-micron wire. Thermal evaporation set-up, photolithography, chemical etching and FIB milling was used sequentially. Since electron beam resist PMMA is burned above 200 ^{0}C, it is impossible to make $La_{0.85}Sr_{0.15}MnO_3$ microstrip on $LaAlO_3$ (100) substrate. We developed a high temperature lithographic technique (schematically explained in FIG. 2.5).

At first by thermal evaporation Al of thickness ~ 40 nm was deposited on LAO substrates and aluminum oxide (Al_2O_3) was prepared by annealing it in furnace at 600 ^{0}C for 3 hrs. By the combination of photo lithography and chemical lithography (with NaOH as etchant) a trench of 50 µm × 4 mm was prepared on the oxide film (see FIG. 2.6(a)). Then by PLD technique $La_{0.85}Sr_{0.15}MnO_3$ film was grown inside the trench at high temperature (~ 700 ^{0}C). Except that rectangular strip of film other portion of the sample was cleaned by NaOH solution (FIG. 2.6(b)). After that by Focused Ion Beam (FIB) milling process (explained later) a sub-micron (width ~ 740 nm) wire was prepared on that strip (FIG. 2.6(c)).

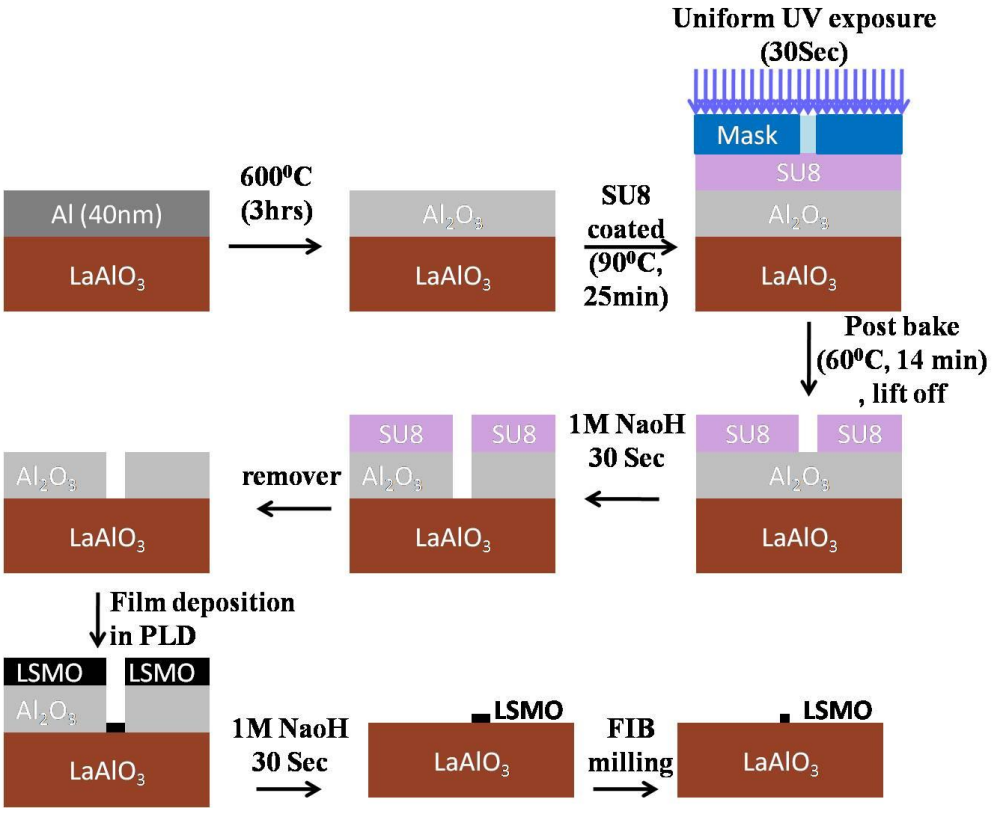

FIG. 2.5. Schematic diagram of the integrated lithography process.

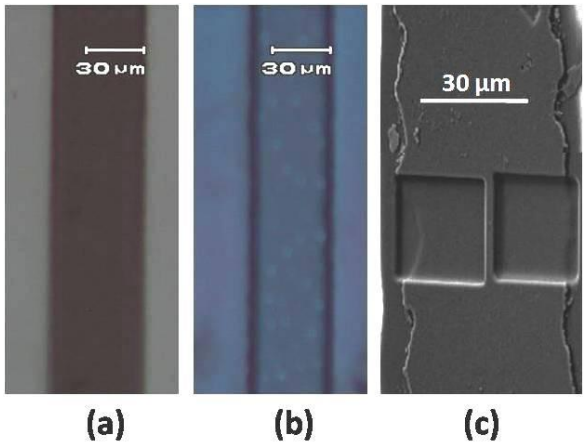

FIG. 2.6. Optical image of (a) Trench on Al-oxide film and (b) Rectangular strip of $La_{0.85}Sr_{0.15}MnO_3$ film. (c) SEM image of sub-micron wire on the strip of the film.

2.1.5. Focused Ion Beam (FIB)

In FIB apparatus liquid metal Gallium is used as a source to produce ion (Ga^+). The most important use of this ion beam is milling or "cutting" a sample according to desired requirements. Ions with kinetic energy ≤ 30 keV are used to sputter away the materials from desired sites by focussing the ion beam on it (see FIG. 2.7(a)). The machine allows preparation of samples with dimensions of few tens of nanometers.

Besides this ion milling FIB has an another important application. Here metal deposition of metals like Pt, Au, W are possible. This technique is used for nanolithography where electrical contact pads are prepared. For depostion of Pt (as done in the work) high energy Ga^+ ion beam breaks the precursour gas of methyl cyclopentadienyl platinum trimethyl $(CH_3)_3(CH_3C_5H_4)$ Pt which is targeted at a desired position and metal (Pt and Ga) is isotropically deposited with amorphous carbon (C) (see FIG. 2.7(b)). Metal content increases with the increase of ion energy. The electrical resistivity of this deposited metal content is very high ($10 - 10^3$ μΩ.m) [2]. This metal deposition is very useful to make voltage lead preparation and lithography where abrupt height difference is present in sample surface.

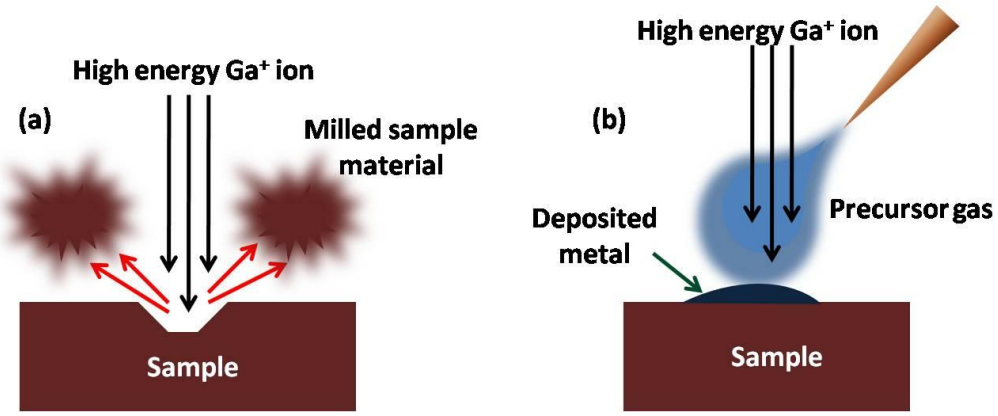

FIG. 2.7. Schematic diagram of (a) sample milling and (b) metal deposition by FIB.

2.1.6. Electrochemical oxidation/reduction

To avoid the difficulties associated with thermal oxidation as describe before in this thesis we used electrochemical oxidation/reduction technique [3-4] to change the oxygen stoichiometry of the samples. This process has been done at room temperature (~ 300 K) so that the grain size of the samples becomes invariant. Also a precise control of oxidation is possible.

A schematic diagram of electrochemical oxidation process is given in FIG. 2.8(a). Here we used conventional three electrode process [5] where the sample was used as working electrode in form of a thin disk shape pellet of nanoparticle or thin film. Rectangular thin Platinum sheet and 1(M) KOH solution was used as counter electrode and electrolyte. We used Hg/HgO as reference electrode. Electrical lead (copper wire) was connected with the sample by silver paste. The electrical lead and the contact area were covered by PMMA resist to avoid any charge deposition at the time of electrochemical process. From the cyclic voltammeter curve (current vs. voltage) (inset of FIG. 2.8(b)) the working potential for best oxidation was found at 0.27 V. The total deposited charge Q was determined from the area under the current (I) vs. time (t) curve (FIG. 2.8(b)). Here we used Faraday Law which will be discussed in section 2.1.6(a).

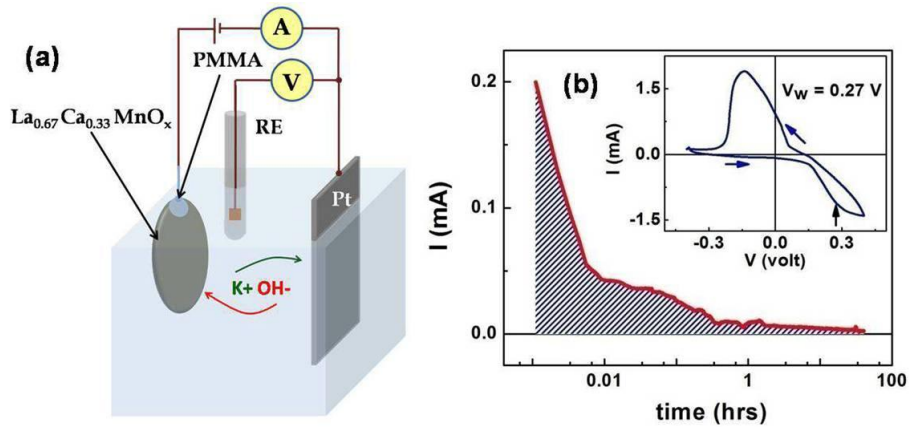

FIG. 2.8. (a) Schematic diagram of three electrode electro deposition process. (b) Oxidation current vs. Time. Inset shows the cyclic voltammetry curve. Arrow shows the best working potential.

Calculation of oxygen stoicchiometry in electrochemically oxidized / reduced samples using Faraday Law:

The oxygen stoichiometry also found out by the Faraday law of calculation. By the electrochemical oxidation process δ has been changed in a sample. The total deposited charge was calculated from the area under the oxidation current (I) vs. time (t) curve (FIG. 2.8(b)) i.e. $Q = \int_0^T Idt$. From Faraday law the change of oxygen stoichiometry can be expressed as,

$$\delta_f - \delta_i = \frac{QM}{2emN_A} \tag{2.1}$$

, where δ_i and δ_f are the initial and final stoichiometry respectively. M is the molecular weight, m is the mass of the sample, N_A is the Avogadro's number and e = 1.6 x 10^{-19} C is the electronic charge. Here 2 come for Oxygen valency.

The change of oxygen stoichiometry $\Delta\delta$ was determined by the above methods. We compared the values obtained from various methods and the analysis shows that the results match very well, an example is shown in TABLE 2.I ($Y_{0.5}Ca_{0.5}MnO_3$ nanoparticles).

TABLE 2.I. $\Delta\delta$ of $Y_{0.5}Ca_{0.5}MnO_3$ nanoparticles of grain size ~ 5 nm.

Process	$\Delta\delta$
Rietveld refinement	0.22 (±0.03)
Iodometric titration	0.24(±0.02)
Faraday Law	0.216(±0.002)

2.2. Characterization

2.2.1. Structural characterization

(a) Lattice parameter determination

(i) X-ray diffraction

It is the most popular technique to determine the crystal structure of samples. When a beam of X-ray incident on crystalline sample, it is scattered in some specific directions depending on the alignment of atomic planes within the crystal.

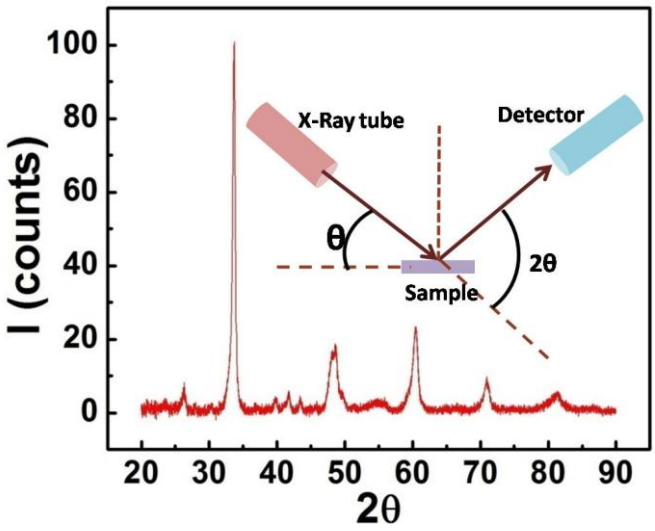

FIG. 2.9. XRD pattern of $Y_{0.5}Ca_{0.5}MnO_3$nano particles of average grain size 5 nm. Inset shows the Schematic of X-ray diffraction process.

According to Braggs' law, $2dsin\theta = n\lambda$, where d is the spacing between parallel atomic planes, θ is the angle between incident X-ray and scattered beam, λ is the wavelength of the incident X-ray. We have used Cu-Kα radiation with wave length λ = 1.5418 A^0. Both the X-ray source and detector was moving at an angle θ by keeping the sample stage fixed and diffraction pattern was recorded. For High temperature XRD Pt-sheet was used as sample holder and the whole setup was inserted into a cage. XRD has been done up to 1073 K temperature [6].

(ii) Neutron diffraction

The basic principle of elastic neutron scattering is same as X-ray diffraction. Similarly Braggs' law is useful here. Neutrons are scattered by the nuclei of the atoms. Neutrons themselves posses spin. Prominent diffraction peaks for light atoms with lesser atomic number can be obtained in neutron diffraction if they have sufficient neutron scattering cross-section.

For a magnetic material the magnetic structure can be clearly understood from neutron diffraction. For temperature above the magnetic transition the diffraction peaks gives the information of only crystal structure. In case of ferromagnetic sample the amplitude of the diffraction peaks increases. For antiferromagnetic structure additional peaks can be seen at lower diffraction angel (FIG. 2.10). We have used UGC-DAE BARC

beam line (at Dhruva reactor). A wave length of 1.48 A^0 was used. The $Y_{0.5}Ca_{0.5}MnO_3$ nanoparticles have average crystallite size down to 75 nm.

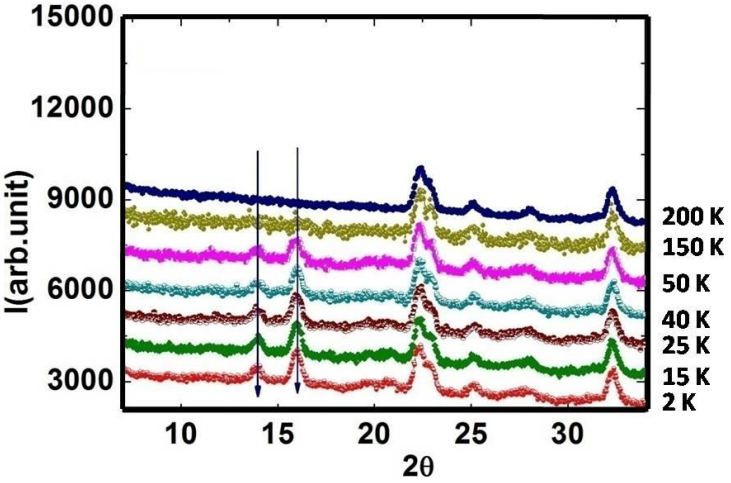

FIG. 2.10. Neutron diffraction curve of $Y_{0.5}Ca_{0.5}MnO_3$ nanoparticles of grain size 75 nm. Antiferromagnetic peaks which are developed from 50 K are indicated by arrows.

Both Neutron and XRD data were analyzed uisng Rietveld method uisng FULLPROF software. This discussed in sub-section 2.2.2.

(b) Scannig electron microscope (SEM)

Here we use this microscope mainly for particle size determination and compositional analysis. The basic part of a SEM consists of an electron gun, condenser lens, objective lens and detectors (see FIG. 2.11(a)). The sample is placed in a chamber with < 10^{-7}mbar pressure. The energy of the electron beams generally range from 5 KeV to 30KeV. The highly energetic electron beam ~ 30 KeV is focused on the sample through condenser lenses within a spot size ranging from 0.4 nm to 5nm in diameter. The incident electron beam can reach up to ~5 µm depth from the sample surface. In the sample, the primary electrons (PE) lose their energy due to random scattering and trapped within a volume. Secondary electrons (SE) are generated due to random inelastic scattering of PEs with the K shell's of the surface atoms. The energy of these emitted SE's is < 50 eV. These SE's are collected by a detector for producing image. To avoid charging non conducting sample is coated with Au or Pt.

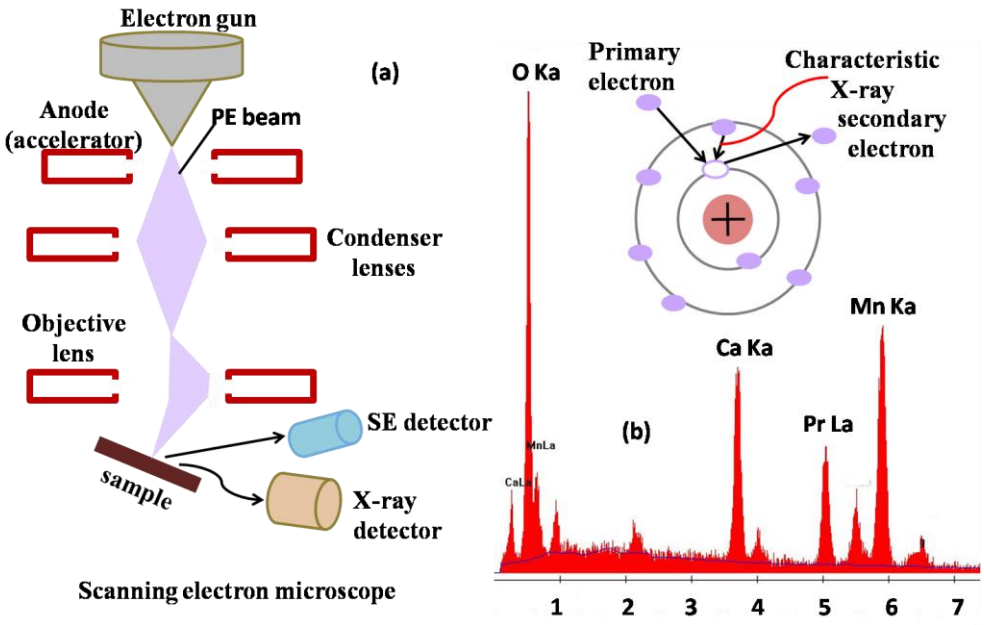

FIG. 2.11. (a) Schematic diagram of SEM. (b) EDX spectrum of $Pr_{0.5}Ca_{0.5}MnO_3$ nanoparticles.

For compositional study energy dispersive X-ray analysis has been done. High energy PE removes electrons from the K-shell of atoms. Then higher shell (L, M, N etc.) electrons jump to vacant K-Shell of and release energy by electromagnetic radiation. This is characteristic X-ray. These X-rays are collected by detector and give the compositional analysis of the samples (FIG. 2.11(b)). This process is called energy dispersive X-ray spectroscopy (EDX).

In this thesis work EDX analysis of all samples has been done using SEM. Also particle sizes ~75nm and ~ 1 µm of $Y_{0.5}Ca_{0.5}MnO_3$sample were determined from SEM images.

(c) Transmission electron microscopy (TEM)

The basic part of a transmission electron microscope consists of an electron source, electron beam, electromagnetic lenses, viewing screen and detectors. High energetic ~200 KeV primary electron beam is transmitted through the sample placed on a thin carbon film coated Cu-grid. The transmitted electrons are detected by a detector (FIG. 2.12).

After interaction of the collimated electrons with the sample specimen, two types of electron beams are existed. One is scattered (diffracted beam) and another one is unscattered (it correspond to the bright central beam of the diffraction pattern). In imaging mode, at the back focal plane of objective lens the objective aperture is inserted. By this aperture if only central beam (un-scattered) is selected, bright field (BF) image is obtained. Dark field (DF) image is received by allowing the signal from the diffracted beam. The final selected signal is magnified and projected on a screen by projector lenses.

The Fourier transform of the periodic potential for the electrons in two dimensions is basically the diffraction pattern. All the diffracted beams and the primary beam are brought together again at the objective lens. The interference of these beams provides a back transformation and form an enlarged picture of the

periodic potential. This operation is called high resolution TEM or simply HRTEM.

In TEM the crystal structure of the samples behaves as a three dimensional grating for highly energetic electrons. A diffraction pattern is generated by the electrons which suffer elastic scattering using electromagnetic lenses. The diffraction pattern can be formed on a selected part of the sample and is called a SAED pattern. For polycrystalline samples the diffraction pattern is in the form of rings and for single crystal samples it is in the form of spots. This can give an idea of the crystal structure of samples. In this thesis work we use TEM to determine the particle size of the samples $A_{0.5}Ca_{0.5}MnO_{\delta}$ (A= Y, Sm, Nd, Pr, La), $La_{0.67}Ca_{0.33}MnO_{\delta}$, $Y_{0.5}Ca_{0.5}MnO_3$ (~75nm grain size) and EDX for these samples also done in TEM as well as in SEM. The results are compatible with each other.

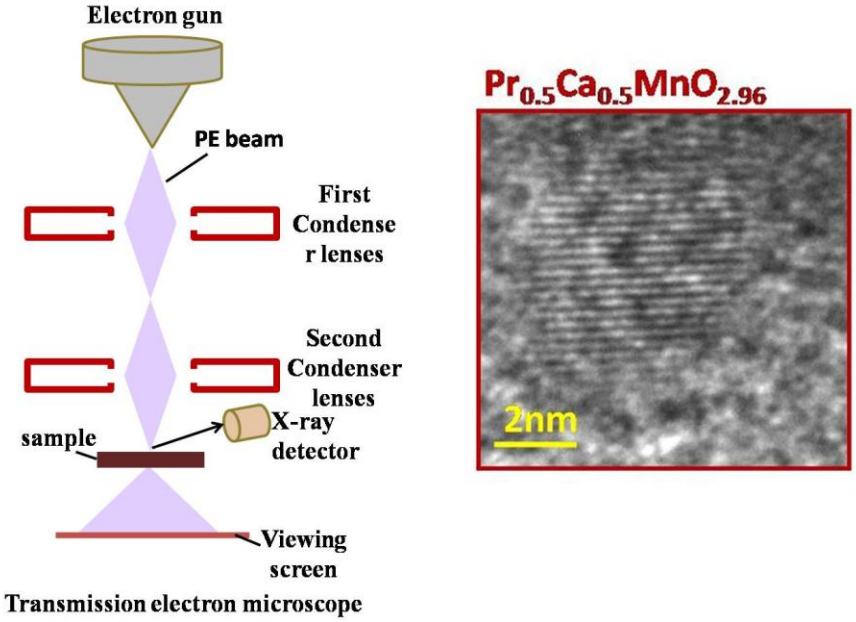

FIG. 2.12. Diagram of TEM schematic and an example of $Pr_{0.5}Ca_{0.5}MnO_3$ nanoparticles of grain size ~ 5 nm.

2.2.2. Stoichiometry checking

The oxygen stoichiometry δ of the samples were checked by various techniques.

(a) Rietvield refinement

In this process the powder X-ray diffraction (XRD) profile (Intensity vs. 2θ curve) was fitted with appropriate crystal structure by using Fullprof software [7]. Space group, lattice parameters and oxygen concentration/vacancy were taken as variable parameters. We took the best fitted values. The oxygen stoichiometry δ was calculated for all the powdered samples used in this thesis. Also the crystal structure parameters (bond distance, bond angle, lattice parameter) of the samples were also determined by this technique.

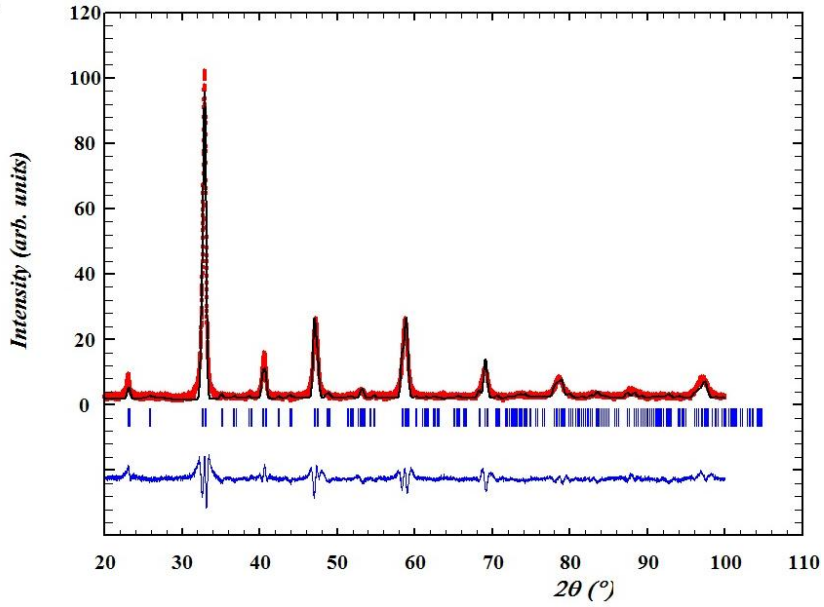

FIG. 2.13. Rietvield refinement of the XRD data of $La_{0.67}Ca_{0.33}MnO_{2.74}$ nanoparticles of grain size ~ 4 nm at room temperature.

(b) Iodometric titration

The molecular formula of an oxide with 50 % divalent cation (B) doping with oxygen deficiency (or oxygen excess) can be written as $A^{3+}_{0.5}B^{2+}_{0.5}Mn^{3+}_{1-y}Mn^{4+}_{y}O^{2-}_{3+\delta}$, where A is the trivalent cation. The valencies are shown in superscripts. For an oxygen deficient (or excess) sample δ and y becomes $\delta \neq 0$ and $y \neq 0.5$ (departure from the ideal value). The value of y and δ can be determined by Iodometric titration method.

Here a known amount of sample with mass m was dissolved in concentrated HCl. Then added it to Potassium Iodide (KI) solution (with known normality N) and titrate with sodium thiosulphate ($Na_2S_2O_3$) solution. The process was repeated with a blank solution (i.e. without the oxide sample). The difference of the volume (V) of $Na_2S_2O_3$ solution in these two processes determine the amount of $Na_2S_2O_3$ which was used by the sample. Oxidation state of Mn before titration was $3(1-y)+4y=3+y$. After the titration process Mn^{2+} was obtained. Thus the change in oxidation state of Mn during titration became $1+y$. The molecular weight of the sample was also known (say, M). Then y was calculated from the equillibrium condition: $m = M(D)N/\{1000(1+y)\}$, where D was the amount of $Na_2S_2O_3$ that was used for this case. Now from the Charge balance condition of $Y^{3+}_{0.5}Ca^{2+}_{0.5}Mn^{3+}_{1-y}Mn^{4+}_{y}O^{2-}_{3+\delta}$, we found $\delta = (y - 0.5)/2$. Thus knowing y we calculated the value of δ. A positive value of δ indicated an excess of oxygen while a negative value of δ implied the oxygen deficiency.

(c) Inductively coupled plasma atomic emission spectroscopy (ICPAES)

It consist two parts Inductively coupled plasma (ICP) and spectrometer. Argon gas is inductively ionized by highly intense radio frequency (RF) electromagnetic field and plasma is generated. Sample is delivered into that plasma and is broken down into ions. Atoms looses electrons and again recombine. Electromagnetic waves of characteristic wave length is generated and is analysed by a spectrometer. Intensity of each spectral line is compared with known intensities and from that the concentration of the elements is computed.

The ratio of the amount of $Y_{0.5}Ca_{0.5}MnO_3$ sample of grain size ~ 75 nm and ~ 1 µm-were calculated by atomic emission spectroscopy. Our result showed that for 75 nm diameter sample and ~ 1 µm grain size sample the Y:Ca:Mn average ratio obtained from ICP-AES is 0.502:0.498:1 which is very close to the expected ratio 0.5:0.5:1.

2.3. Physical measurements

2.3.1. Electrical resistance measurement

Conventional four probe method was used to measure the electrical resistance. A rectangular disc shape pellet was prepared from powdered nano grained samples. The contact pads have been prepared on the samples by using wire lithography with separation between leads ~ 120 µm and thermal evaporation. DC current (I) was generated by a current source and passed through the sample between current leads. Voltage (V) between the voltage leads was measured by a Digital multimeter (DMM). Resistance (R) of the sample was measured by the ratio of voltage and current, $R = V/I$. Resistivity (ρ) was calculated from R. A pulsed tube Helium cryostat was used for electrical measurement in the temperature range 4 K to 330 K [8]. Data taking has been automated by a computer Labview programming through GPIB cable.

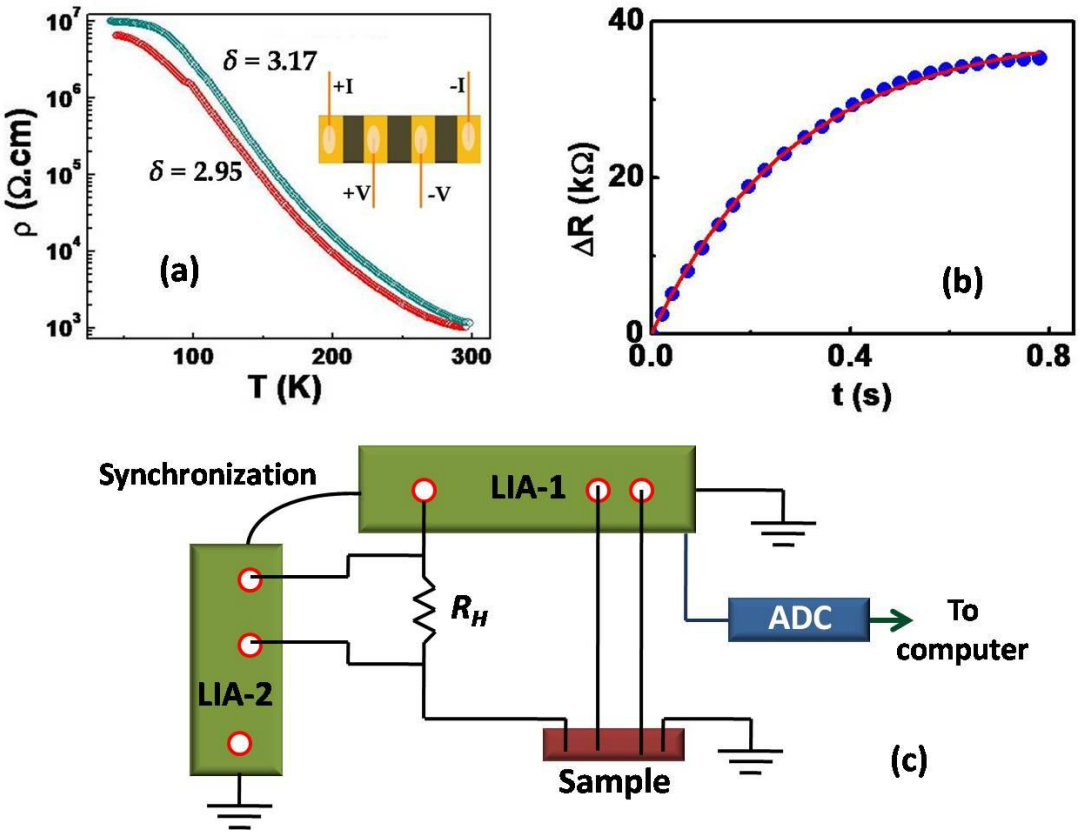

FIG. 2.14. (a) Resistivity (ρ) vs. temperature (T) of two $Pr_{0.5}Ca_{0.5}MnO_{\delta}$ nanoparticle samples of δ = 2.95 and 3.17. The average grain size of the sample is ~ 5 nm. DC resistance measurement has been done here. Inset shows the four probe arrangement on the sample. (b) The resistance relaxation data of $La_{0.85}Sr_{0.15}MnO_3$ microchannel due to oxygen diffusion. This resistance change (ΔR) vs. time (t) data has been taken by AC method. (c) Schematic diagram of AC resistance measurement technique.

Since the resistance relaxation for oxygen diffusion-can be affected by DC current flow, to study the resistance relaxation AC technique was used. Here a low frequency (~ 173 Hz) AC current (I_{ac}) was generated by a Lock-in-amplifier (LIA1) and it was passed through the sample. The voltage across the sample was measured by the same LIA1. To make a constant current flow a high resistance (R_H) was attached in series. The value of I_{ac} was calculated from the measured voltage across R_H. This voltage was measured by another Lock-in-amplifier (LIA2) which was synchronized with LIA1. The high speed data taking has been done by a computer through a 32-bit analogue to digital converter (ADC) card (PCIDAS6036, 200 ksamples/sec). The user friendly C++ programming was used for data collection.

2.3.2. Magnetic property measurement

(a) Vibrating sample magnetometer (VSM)

The magnetic property of the samples can be measured very well by using vibrating Sample Magnetometer (VSM). The working principle of this instrument is based on Faraday Law of electromagnetic induction. Firstly the sample is magnetized in a uniform magnetic field. Helmholtz coil was used to produce uniform magnetic field. Then it is sinusoidally vibrated by a piezoelectric material which induces an ac voltage across the pickup coils. The induced voltage is, $V_{ind} = -\partial\varphi/\partial t$, where φ is the magnetic flux across the pickup coils. This induced voltage is recorded by a Lock in amplifier. From this voltage the magnetisation (M) of the sample is calculated [9]. The VSM has a minimum resolution 10^{-6}emu. For our experiments we have used a commercial VSM which has magnetic field range up to 1.6 Tesla and temperature range from 80 K to 1250 K. We have measured Applied Field (*H*) dependent magnetisation (*M*) curve of our samples. We have also used VSM to measure Zero field cooled (ZFC) and Field cooled (FC) temperature dependent magnetisation of the samples.

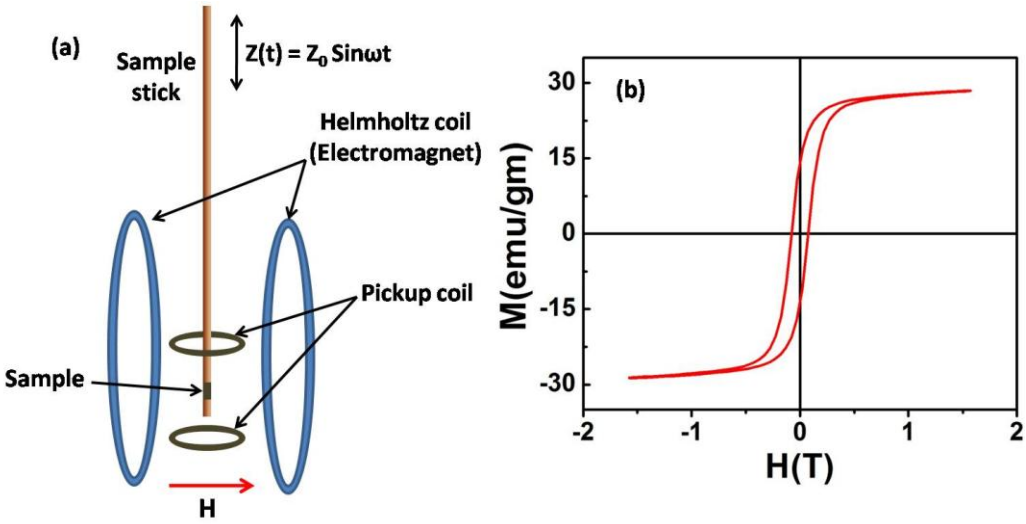

FIG. 2.15. (a) Schematic diagram of the working principle of VSM. (b) Magnetisation (*M*) versus applied magnetic field (*H*) data of $La_{0.67}Ca_{0.33}MnO_{2.74}$ sample of grain size ~ 4 nm at 80 K.

(b) Superconducting quantum interfearence device (SQUID)

SQUID is a magnetometer with a minimum resolution of 10^{-8} emu. It works on the basic principles of superconducting loops containing Josephson junction. We have used SQUID to measure the Magnetisation (*M*) versus applied field (*H*) and in temperature range 5 K to 400 K. Example of data is shown in Figure 2.16 for $Y_{0.5}Ca_{0.5}MnO_3$samples with average grain size ~5nm.

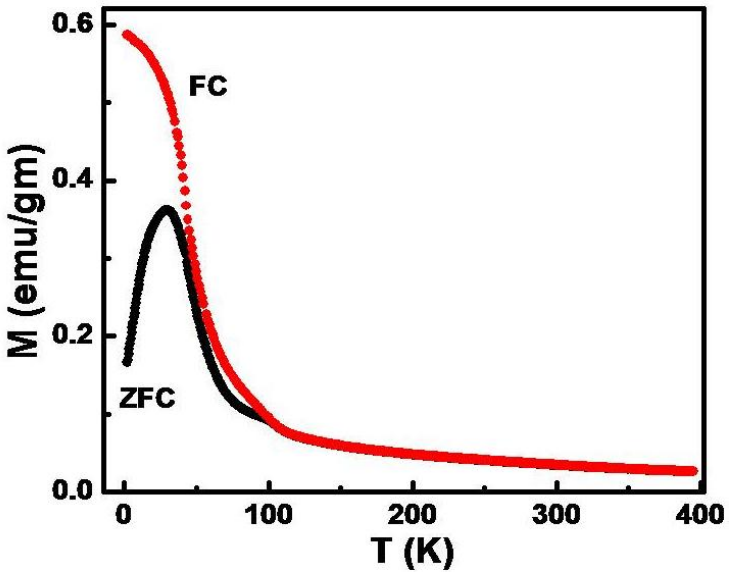

FIG. 2.16. Field cooled (FC) at 0.7 T and zero field cooled (ZFC) magnetization (*M*) vs. temperature (*T*) curve of $Y_{0.5}Ca_{0.5}MnO_3$ sample of grain size ~ 5 nm.

References:

1. K. Shanta Shankar and A. K. Raychaudhuri, *J. Mater. Res*. **21**, 27 (2006).
2. Manotosh Chakravorty, K. Das, A. K. Raychaudhuri, J. P. Naik and P.D. Prewett, *Microelectronic Engineering*, **88**, 3360 (2011).
3. I. L. Zhogin, A. P. Nemudry, P. V. Glyanenko, Yu. M. Kamenetsky, H. J. M. Bouwmeester and Z. R. Ismagilov. *Catalysis in Membrane Reactors*. **118**, 151 (2006).
4. L. E. Hueso, F. Rivadulla, R. D. Sanchez, D. Caeiro, C. Jardon, C. Vazquez-Vazquez, J. Rivas and M. A. Lopez-Quintela, *Journal of Magnetism and Magnetic Materials*.**189**, 321 (1998).
5. R. Kumar Pandey, S. N. Sahu and Suresh Chandra, *Handbook of Semiconductor Electrodeposition* (CRC Press, 1996).
6. PANanalytical B. V., Lelyweg 1, 7602 EA Almelo, Netherlands.
7. *www.Fullprof.edu*.
8. W. E. Gifford and R. C. Longsworth, *Adv. Cryo. Eng.* **3b**, 69 (1963).
9. K. H. J. Buschow and Frank R. Boer, *Physics of Magnetism and Magnetic Materials*, Springer (2003).

Chapter 3

Nanoscopic control of stoichiometry of oxide nanoparticles of $La_{0.67}Ca_{0.33}MnO_3$ using electro-chemical route and the resulting physical and structural properties

In this chapter it is established that precision control of oxygen stoichiometry can be done by electrochemical oxidation in manganite nanoparticles at room temperature. $La_{0.67}Ca_{0.33}MnO_{\delta}$ nanoparticles of size ~ 4 nm have been prepared by chemical solution deposition (CSD) method. To keep the particle size constant electrochemical oxidation method has been used to change the oxygen stoichiometry δ (from 2.74 to 3.20) at room temperature reversibly. The unit cell volume and orthorhombic strains are sharply affected by incorporation of oxygen into the as prepared sample (δ = 2.74). The *Mn−O−Mn* bond angles also changes for δ > 3 and < 3. The electrochemical control of δ from 2.74 to 3.20 encompasses the optimum doping of $\delta \approx 3$.The tuning of δ by an amount of 0.46 can enable a change in ferromagnetic T_C nearly by 16 K accompanied by a large change in H_C. The reversibility of the process was confirmed by using electrochemical reduction on a previously oxidised sample. The observed behaviour has been explained through changes in magnetic moments as well as the change in the structure that changes the orthorhombic distortion.

3.1Introduction

In perovskite oxides, the physical property changes by changing oxygen stoichiometry. In bulk and film of different perovskite samples the effects of oxygen nonstoichiometry have been studied rigorously [1-4]. Most of these works have been done by heat treatment (> 500^0C) with changing the oxygen partial pressure [1-5]. But in nano perovskites heat treatment must be avoided to keep particle size unchanged. Therefore, though the effect of oxygen non-stoichiometry on hole doped nanomanganites is an interesting topic, it remains an unsolved problem due to the previously mentioned constraint where change of stoichiometry by heat treatment also changes the particle size. Electrochemical oxidation is a tool to oxidize the nano perovskites at room temperature (~300 K) [6,7]. Previously electrochemical method has been used to change oxygen concentration on Lu_2CuO_4 [8,9], $La_{0.2}Sr_{0.8}CoO_3$ [10], $La_4Ni_3O_{10}$ [11], La_2CuO_4 [12] samples but no work has been done on nanomanganites. The paramagnetic insulating (PI) to ferromagnetic metal (FM) transition temperature (T_C) varies in a non-trivial way in $La_{0.67}Ca_{0.33}MnO_3$nanomanganites due to the decrease of particle size from bulk to ~15 nm [13]. But there is no work where the effect of oxygen non-stoichiometry in crystal structure and ferromagnetism has been studied in nano crystallites. There is a report of Hueso et. al. [7] who did not find any change in T_C in this system with grain size 50 nm (meso region) for limited variation of oxygen stoichiometry from 2.97 to 3.01. But there is no report of crystal structure analysis and existence of ferromagnetism in $La_{0.67}Ca_{0.33}MnO_3$ of particle size below 10 nm. From our best knowledge in this thesis we have first time studied the detailed variation of T_C, H_C (Coercive field), and structural parameter of $La_{0.67}Ca_{0.33}MnO_\delta$ of particle size ~4 nm with the variation of Oxygen stoichiometry δ ranging from 2.74 to 3.2 ($\Delta\delta$ ~ 0.46).

3.2 Experimental Methods

We have prepared $La_{0.67}Ca_{0.33}MnO_\delta$ nano particles by chemical solution deposition method (CSD) as described in chapter 2. From this as prepared sample (S_1) we have prepared another set of four samples (S_2, S_3, S_4 and S_5) which have different oxygen stoichiometry (δ). Another sample S* has been prepared by reduction of S_5. Samples S_2 to S_5 and sample S* was prepared from sample S_1 by electrochemical methods

3.2.1 Sample Preparation

In CSD method (discussed detail in Chapter 2) high purity Lanthanum acetate hydrate, Calcium acetate hydrate and Manganese acetate tetra hydrate were mixed with de ionized (DI) water and Acetic acid in stoichiometric ratio. Appropriate amount of ethylene glycol were added. The polymer (ethylene glycol) was used for forming a network of cations which assisted the reaction in phase formation. The solution was heated and stirred at ~70^0C for making it in gel formation. The gel was dried for 15 hours at temperature ~ 150^0C. After that pyrolysis process was done at 350^0C and 450^0C. Then finally it was sintered at 650^0C for 3 hours to obtain the proper phase and particle size.

3.2.2 Oxygen stoichiometry change

The oxygen stoichiometry of S_1 was changed by electrochemical oxidation method at room temperature (~300 K). The electrochemical method has been discussed in

details in Chapter 2 (sections 2.1.6, FIG. 2.7., Page 23). Here we give the relevant numbers and oxidation/reduction parameters.

The oxygen stoichiometry (δ) was also found by Faraday's law. In this process the difference between two stoichiometry can be written as,

$$\Delta\delta = \delta_f - \delta_i = \frac{QM}{2emN_A} \quad (3.1)$$

, where δ_f and δ_i are the final and initial stoichiometry. The total deposited charge (Q) in electrochemical deposition can be calculated as, $Q = \int_0^{T_f} Idt$(area under the *I-t* curve and T_f is the total depositing time). Molecular weight and mass of the sample are *M* and *m* respectively. Avogadro's number is N_A, charge of an electron is e = 1.6 x 10^{-19}C and the factor 2 comes for Oxygen valency. To find the value of the stoichiometry $\delta(=\delta_f = \Delta\delta + \delta_i)$ the above equation 3.1 has been used to calculate $\Delta\delta$ for S_2, S_3, $S_4$and S_5. δ_i is the starting value of δ of S_1 (has been taken from Rietveld refinement). Data are given in TABLE 3.1. We have checked the value of δ for S_1 and S_5 by Iodometric titration method as a check. TABLE 3.I shows the different δ values of different samples obtained with different methods. In this work all the results are plotted with respect to δ which is obtained from Rietveld refinement and it gives an absolute δ.

TABLE 3.I. Oxygen stoichiometry (δ) and charge deposited per unit mass of different samples are summarized.

Sample-ID	**δ (Rietveld refinement)**	**δ (Faraday Law) (±0.002)**	**δ (Iodometric titration)**	**Charge deposited (C/gm)**
S_1	2.74(±0.038)	2.740	2.74(±0.021)	--
S_2	2.76(±0.035)	2.763	--	21.209
S_3	2.78 (±0.035)	2.785	--	20.288
S_4	2.90 (±0.035)	2.912	--	117.115
S_5	3.20 (±0.030)	3.230	3.22(±0.024)	293.249
S^*	3.14 (±0.035)	3.143	3.14((±0.021)	-80.229

3.3Results

3.3.1 Crystal structure

The TEM images and distribution of particle size for all the samples are plotted in FIG.3.1. (a) and FIG.3.1. (b), which confirms, that the samples has mean particle size 4(±1) nm.FIG.3.2 shows the XRD patterns (red lines) with fitting (black lines) and residues (blue lines) for S_1 to S^* samples respectively. Crystal structure analysis has been done from x-ray diffraction pattern by Rietveld refinement method. All the samples shows orthorhombic Pnma space group. In TABLE 3.II the lattice parameters (*a, b* and *c*), unit cell volume and *Mn-O-Mn* bond angels for all the samples are tabulated. In TABLE 3.III the lattice parameters (*a, b* and *c*) are compared with the value of bulk samples [13].

In manganite nanoparticles with sizes ~ 4 nm, there are small but subtle changes that occur in the structure. For instance, while the lattice constants *a* and *c* become smaller, lattice constant *b* is larger. This occurs due to distortion of the MnO_6 octahedra and their packing. A notable change occurs in the *Mn-O_2-Mn* bond angle that reduces substantially from ~171^0 to ~150^0. This will lead to reduction in double

exchange and reduction in the magnetization and saturation moment (M_S). This modification in the MnO_6 octahedra on size reduction changes the orthorhombic distortions $OS_{\parallel}$ and $OS_{\perp}$. The orthorhombic distortion (strain) in ac-plane is defined by $OS_{\parallel} = \frac{2(c-a)}{c+a}$ and that along the b axis with respect to ac-plane is defined by $OS_{\perp} = \frac{2(a+c-b/\sqrt{2})}{(a+c+b/\sqrt{2})}$. The effect of changing δ that happens in this case without a change in size leads to changes in the lattice constants as well as unit cell size and in the orthorhombic distortion.

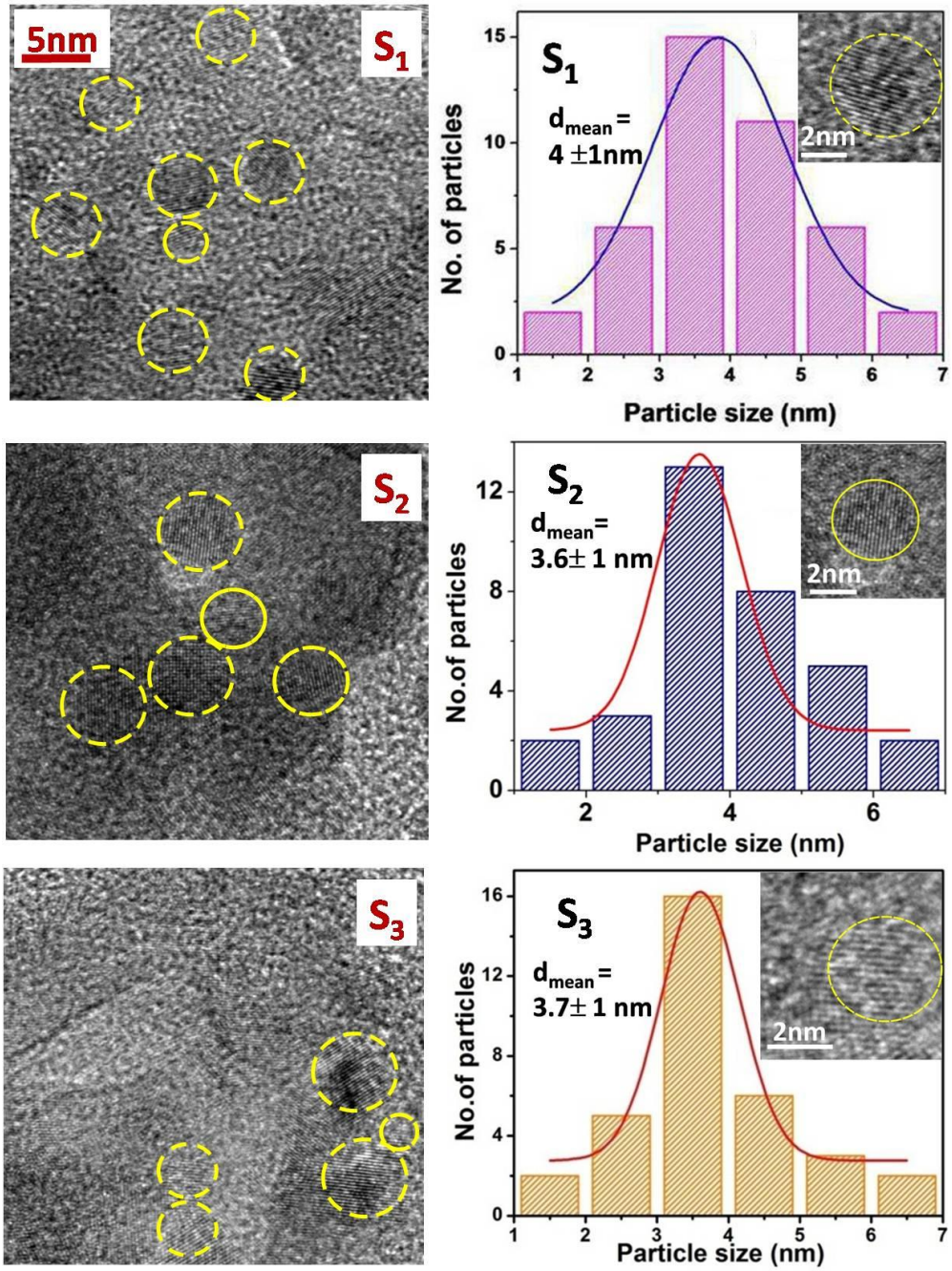

FIG. 3.1. (a).The TEM images of S_1, S_2, S_3 samples and their particle size distribution plots are given. The inset of distribution plots shows single particle TEM images of corresponding samples.

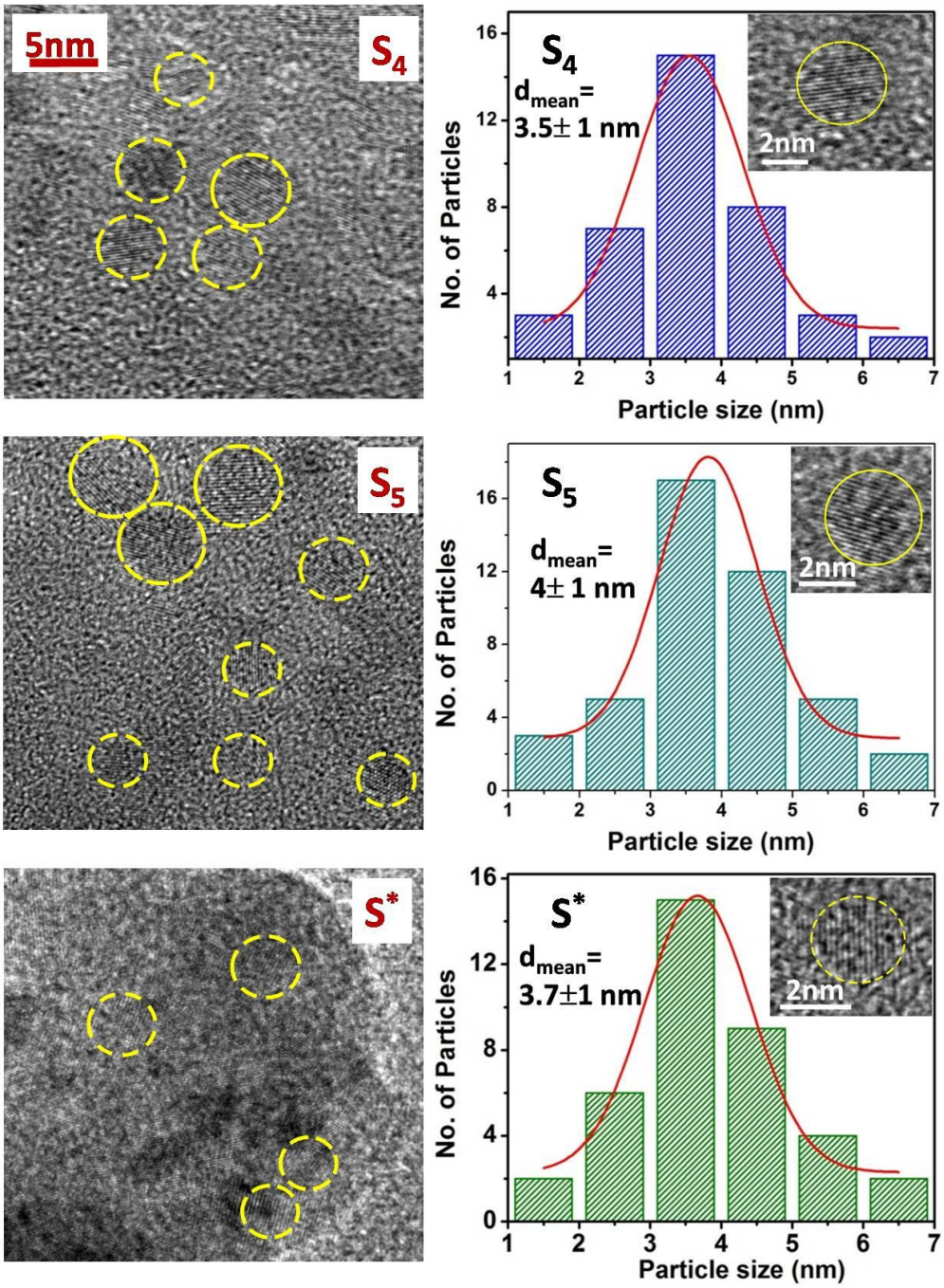

FIG. 3.1. (b).The TEM images of S_4, S_5, S^* samples and their particle size distribution plots are given. The inset of distribution plots shows single particle TEM images of corresponding samples.

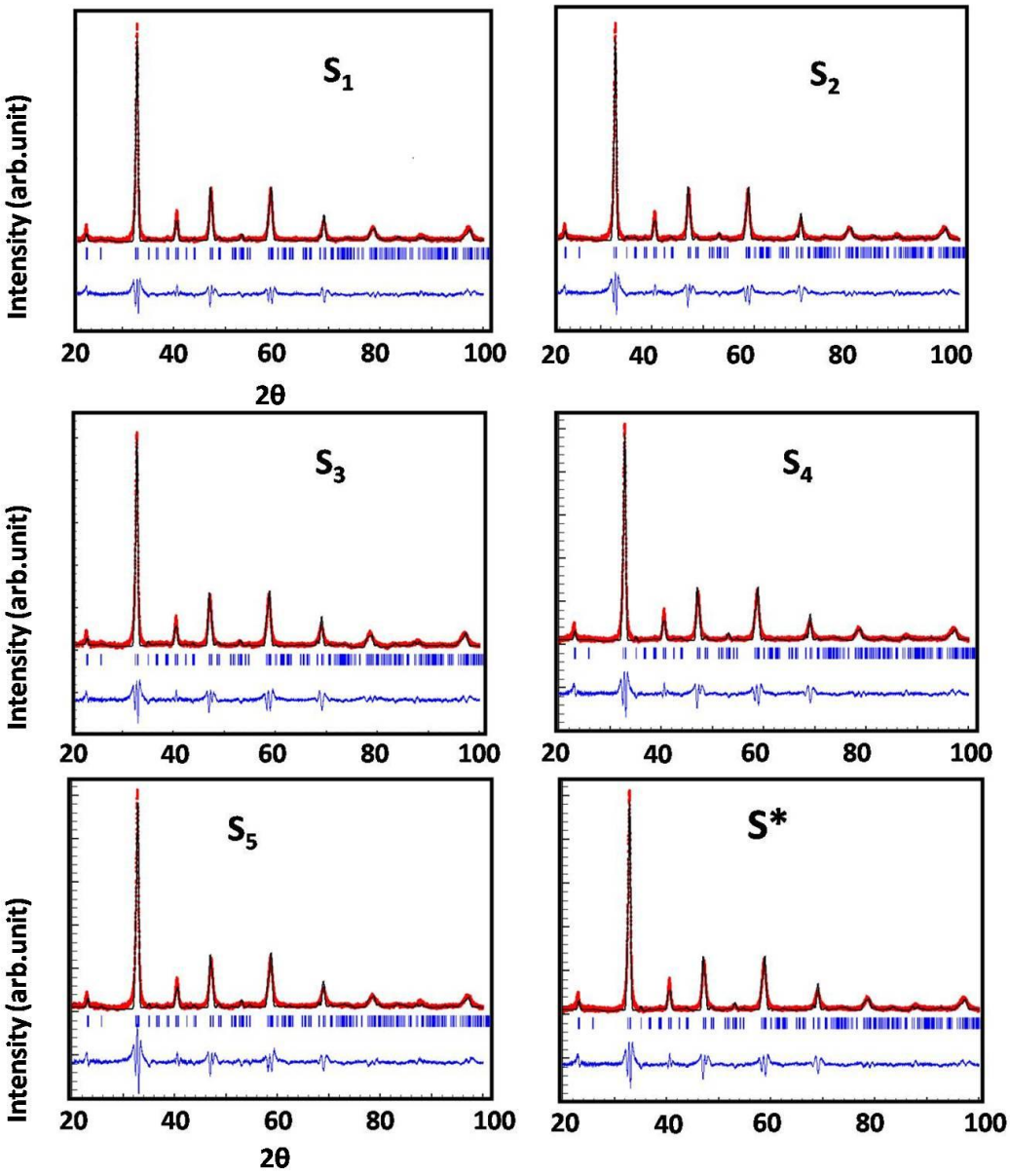

FIG. 3.2 . The XRD data and the Rietveld profile fit with residual at 300 K of samples S_1, S_2, S_3,S_4, $S_5$and S^*.

TABLE 3.IIa. Structural parameters of the samples obtained from Rietvield refinement.

Sample-Id	δ	a (A^0)	b (A^0)	c (A^0)
S_1	2.74	5.42464(±0.00046)	7.65828(±0.00063)	5.49124(±0.00041)
S_2	2.76	5.42698(±0.00044)	7.66011(±0.00061)	5.49831(±0.00040)
S_3	2.78	5.42765(±0.00042)	7.65922(±0.00056)	5.50046(±0.00038)
S_4	2.90	5.42710(±0.00043)	7.65990(±0.00059)	5.50247(±0.00040)
S_5	3.20	5.43424(±0.00042)	7.67168(±0.00058)	5.51238(±0.00038)
S^*	3.14	5.4407(±0.00043)	7.66855(±0.00057)	5.51023(±0.00039)

TABLE 3.IIb. Structural parameters (unit cell volume *V* and bond angles) obtained from Rietvield refinement.

Sample-Id	δ	V $(A^0)^3$	*Mn-O_1-Mn*	*Mn-O_2-Mn*
S_1	2.74	228.12(±0.032)	172.999(±0.01)	151.945(±0.017)
S_2	2.76	228.57(±0.031)	173.12(±0.008)	151.7(±0.017)
S_3	2.78	228.66(±0.029)	171.25(±0.01)	154.5(±0.017)
S_4	2.90	228.74(±0.030)	170.76(±0.01)	151.8(±0.019)
S_5	3.20	229.81(±0.029)	172.41(±0.008)	145.9(±0.017)
S^*	3.14	229.69(±0.03)	172.33(±0.01)	147.32(0.017)

The change in lattice parameters for different values of δ is shown in FIG.3.3 (a). The δ dependence of the cell volume (V) has been shown in FIG.3.3 (b). (Data are also tabulated in TABLE 3.IIb).

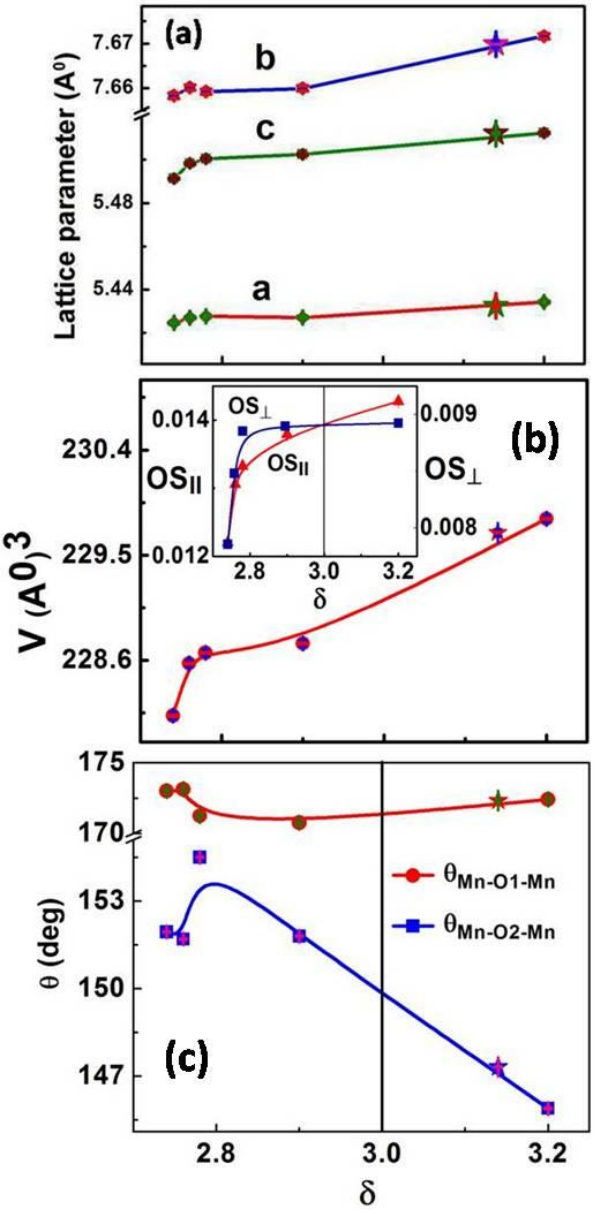

FIG. 3.3. Oxygen stoichiometry (δ) dependence of (a) lattice parameters and (b) crystal volume (c) bond angles are shown. Star (*) symbols are the results of reduced sample S^*. Error bars are smaller than the symbols.

The initial oxidation makes the δ value from 2.74 to 2.76. There are changes in *a, b, c* and *V* that occur for a small change in δ. After that the values gradually increase with δ. For $\delta \geq 2.9$ the lattice constant *b* shows enhancement when δ is increased and this shows as an enhancement in unit cell volume *V.* For a change of oxidation from 2.74 to 3.20 (~0.46) the value of *V* changes from 228.2 $(A^0)^3$ to 229.8 $(A^0)^3$ (~ 0.7 %). While it is expected that when a large ion like Oxygen is introduced in the lattice, it will expand leading to enhancement of unit cell volume, what is non-trivial is that it distorts the lattice and changes the *Mn-O-Mn* bond angle. The variation of orthorhombic strains with δ is also shown in the inset of FIG. 3.3(b). For the initial change of δ, $OS_{\parallel}$and $OS_{\perp}$increase sharply and after that though $OS_{\parallel}$ has a gradual increment, $OS_{\perp}$freezes.

The oxygenation of the 4 nm sample does not lead to reduction in orthorhombic distortions instead it increases it. This differs from a bulk sample of optimal oxygen stoichiometry ($\delta \approx 3$) that has low orthorhombic distortion and less distorted MnO_6 octahedra with both $Mn - O_1 - Mn$ and $Mn - O_2 - Mn$ bond angles nearly equal ($\approx 180^0$) and the structure with low orthorhombic distortion is close to being cubic [14].

TABLE 3.III. Comparison of structural parameters of bulk and nanoparticle sample.

Structural parameters	**Bulk ***	**Nanoparticle Diameter ~ 4 nm for δ=3.2**
a	5.433 A^0	5.434A^0
b	7.687 A^0	7.672A^0
c	5.473 A^0	5.512A^0
V	228.33 $(A^0)^3$	229.81$(A^0)^3$
$Os_{\parallel}$	5.5X10^{-3}	14.3X10^{-3}
$Os_{\perp}$	2.0X10^{-3}	8.9X10^{-3}
$Mn-O_1-Mn$	172.5^0	172.41^0
$Mn-O_2-Mn$	171.75^0	145.9^0

* Values are taken from the work of Sarkar et. al. [13]

For bulk sample of $La_{0.67}Ca_{0.33}MnO_{\delta}$ it has been found [15] that as δ value increases from 2.80 to 3, the unit cell volume decreases from 236.19$(A^0)^3$ to 232.03$(A^0)^3$. The decrease of the volume on oxidation is due to the conversion of Mn^{3+} ions into Mn^{4+} as the effective ionic radii of Mn^{3+} and Mn^{4+} in octahedral oxygen coordination are 0.645 and 0.530 A^0, respectively [16]. But for our case (i.e, the nanopartcicles) as δ increases from 2.74 to 3.2 the crystal structure volume monotonically increases. Though the origin of this behaviour cannot be established firmly, however, the difference can arise from two sources: (a) Orthorhombic distortions that distort the octahedra as well as their packing as can be seen from the unequal bond angles and (b) existence of a highly oxygen deficient (and magnetically "dead layer") as can be seen from the magnetic data below. This layer houses higher concentration of Mn^{3+} ions leading to larger volume.

3.3.2 Magnetic Properties tuned by changing δ

The structural studies show that change in oxygen stoichiometry δ leads to small but subtle changes in the structure. We show how a change in δ done by electrochemical

means at room temperature without change in size or chemical composition can bring about substantial changes in the magnetic properties like spin-moments (obtained from high temperature Curie-Weiss law $\chi = (C/(T - T_C))$, ferromagnetic transition T_C, saturation magnetic moment (M_S at $T/T_C < 1/3$) and the Coercivity H_C.

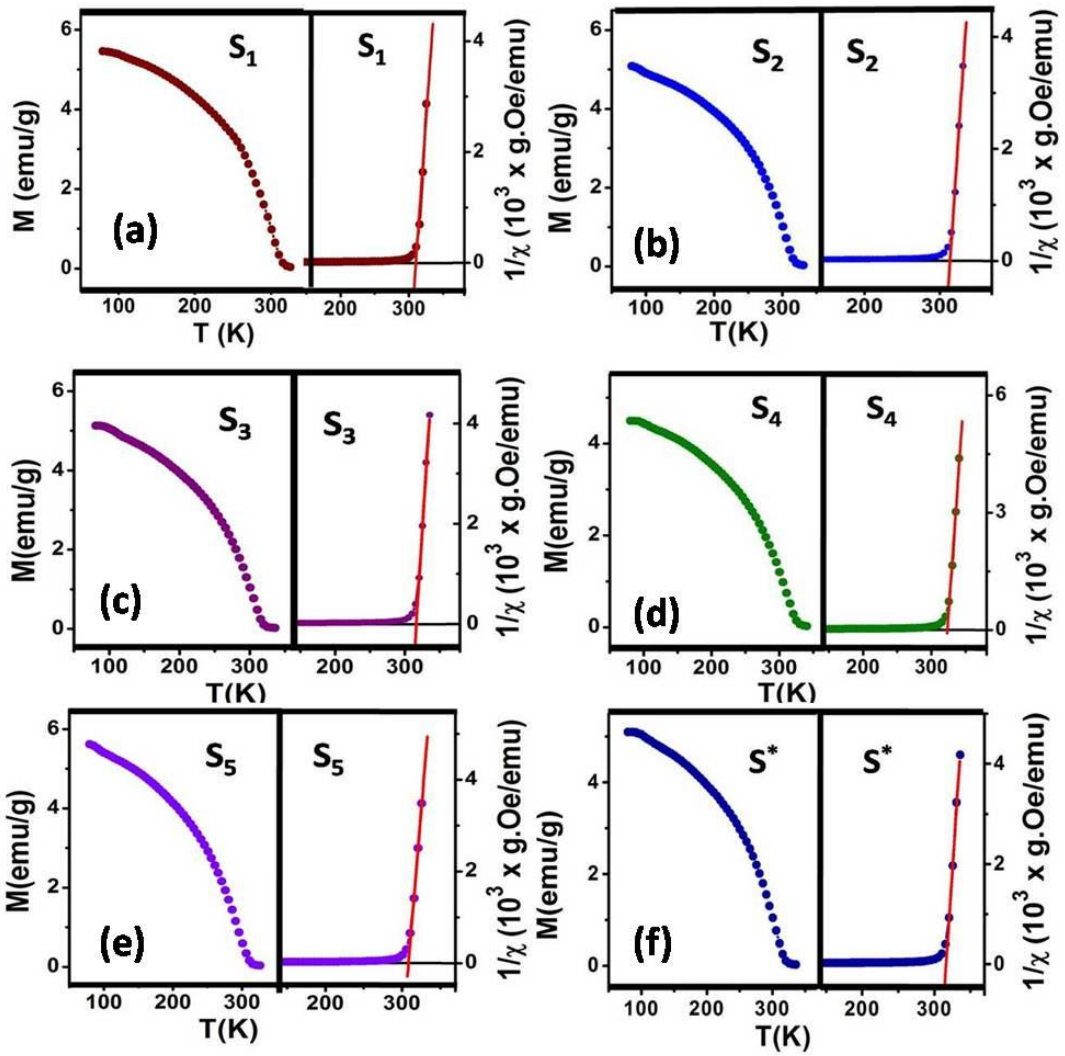

FIG.3.4. Field dependence magnetization at a field of 0.01T and $1/\chi$ vs. temperature fitting of (a) S_1, (b) S_2, (c) S_3, (d) S_4, (e) S_5 and (f) S^* samples is plotted.

In FIG.3.4 we show the magnetization M taken at a field of 0.01T for all the samples.

The onset of ferromagnetic transitions can be seen. We have also plotted the Curie-Weiss plot of $1/\chi$ vs. T for respective samples in FIG.3.4. Susceptibility $\chi \equiv M/H$ is obtained from the low field data. From the plot we identify the Curie temperature T_C and the spin values (μ_{eff}) from the Curie constant (C) using the relation, $C = {\mu_{eff}}^2/3k_B$. In TABLE 3.IV we show C, μ_{eff} (in units of Bohr magnetron) and the Curie temperature T_C. The same are plotted as a function of δ in FIG.3.5. The M_S and H_C are obtained from M-H curve taken at 80 K and shown in FIG.3.6. In the TABLE 3.V and FIG.3.7 we also show the coercive field H_C and the saturation magnetization M_S and as a function of δ.

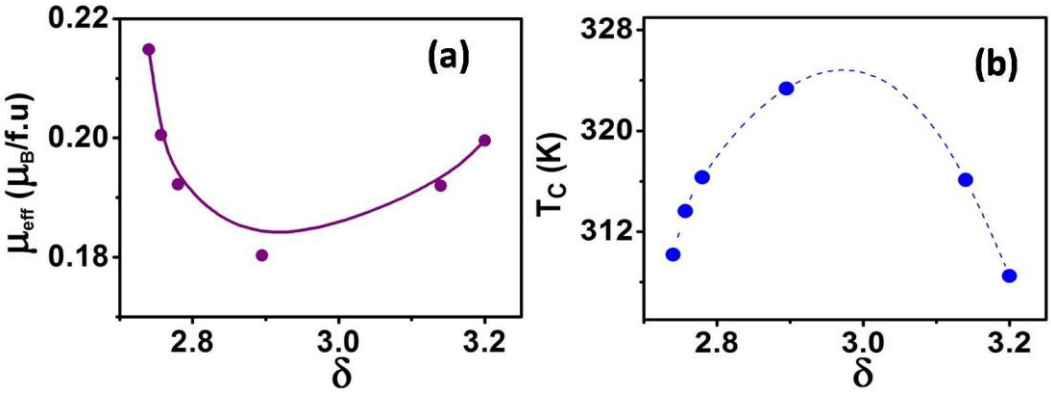

FIG. 3.5. (a) Effective magnetic moment μ_{eff} per formula unit and (b) Curie temperature (T_C) are plotted with respect to δ.

TABLE 3.IV. Results obtained from $1/\chi$ vs. T plot.

Sample-Id	δ	C(g.Oe/emu)$^{-1}$K	$\mu_{eff}(\mu_B)$	T_C(K)
S_1	2.74	0.00576	0.21482	310.16
S_2	2.76	0.00502	0.20047	313.62
S_3	2.78	0.00461	0.19223	316.30
S_4	2.90	0.00406	0.18027	323.35
S_5	3.20	0.00497	0.19959	308.47
S*	3.14	0.00460	0.19198	316.10

TABLE 3.V. Saturation magnetization and coercive field for different samples.

Sample-Id	δ	M_S (μ_B/f.u)	M_S/μ_{eff}	$\mu_0 H_C$ (T)
S_1	2.74	1.132	5.27	0.076
S_2	2.76	0.983	4.91	0.039
S_3	2.78	0.993	5.17	0.040
S_4	2.90	0.833	4.62	0.043
S_5	3.20	1.064	5.33	0.040
S*	3.14	0.893	4.65	0.042

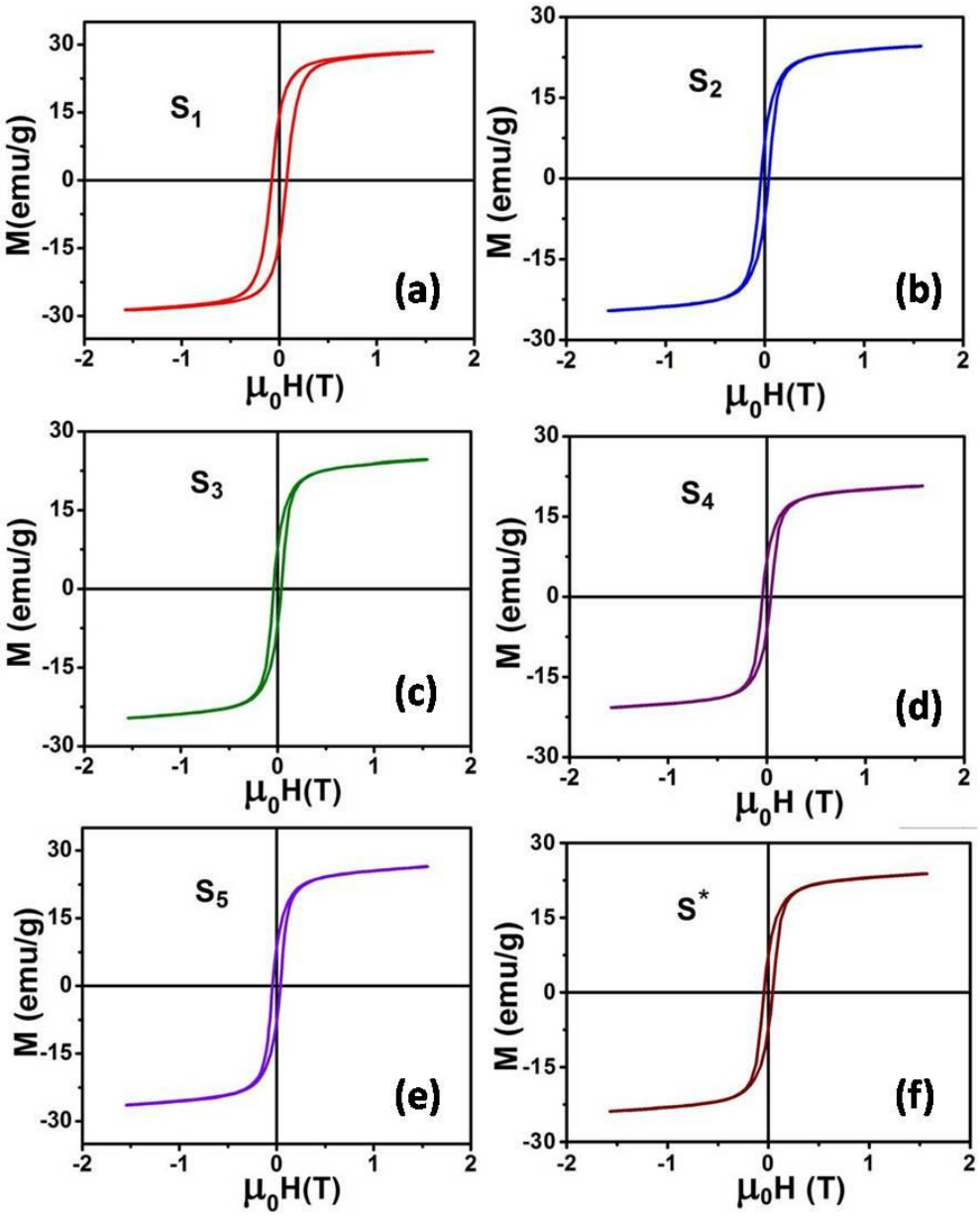

FIG. 3.6. Magnetisation vs. field curves of (a) S_1, (b) S_2, (c) S_3, (d) S_4, (e) S_5 and (f) S^* at temperature 80 K.

The Curie temperature shows a non-monotonous dependence on δ and expectedly the highest T_C (~ 324 K) is seen for $\delta \approx 3$.T_C reported for bulk sample [17] is 274 K and for single crystal it is 250 K [18].This is substantially larger than that seen in bulk samples and even that in single crystals. It has been seen before that size reduction leads to enhancement of T_C in nano-manganites like $La_{0.67}Ca_{0.33}MnO_3$ [13]. However, the enhancement in the T_C observed by us after electrochemical oxidation is significantly higher that seen in previous studies. In fact the observed T_C of 324 K in nanoparticles of LCMO is the highest reported. We also observe that by a change of δ from 2.74 to 3.2 the T_C can be tuned by nearly 16 K. We also observe that by reducing a sample with higher value of δ it is possible to reverse the oxidation for S^* sample.

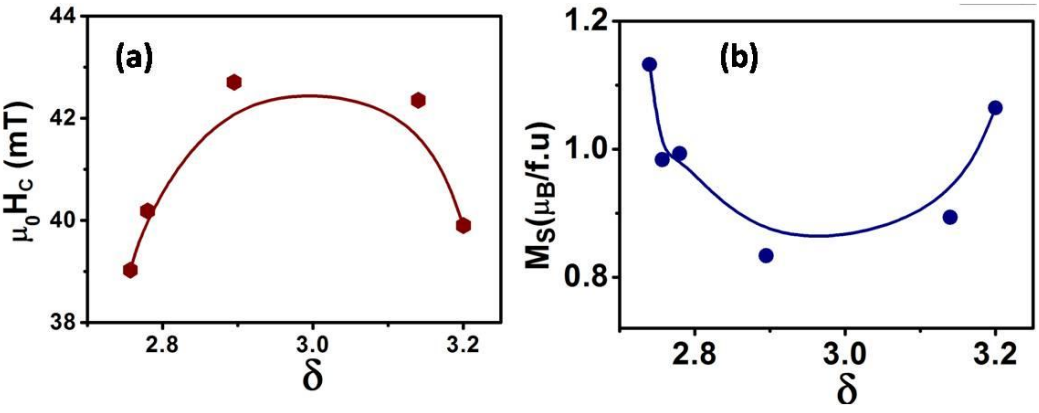

FIG. 3.7. (a) Coercive field and (b) saturation magnetisation versus δ is plotted.

The saturation magnetization M_S as shown in FIG.3.7 (b) also has a non-monotonous dependence on δ and it is opposite to that seen in the dependence of T_C on δ. The effective magnetic moment (μ_{eff}) similarly follows the same trend with δ as M_S follows (which is obvious). The similar trends in the μ_{eff} and M_S can be best seen from the ratio M_S/μ_{eff} shown in TABLE 3.V. It can be seen that the ratio is mostly constant ~ 4.99 ± 0.11.

The coercive field (H_C) shows a maximum value around $\delta \approx 3$. In optimally doped LCMO the value of M_S at 80 K is around 3-3.2 μ_B/Mn. In contrast, in the nanoparticles (from 15 to 30 nm diameter) the value of M_S at 80 K ranges from 0.5-3.25 μ_B/Mn [19]. For δ either < or > 3 the value of M_S increases because the effective valency and of *Mn* and hence the effective magnetic moment μ_{Mn} on *Mn* changes as value of δ changes (Note: for $La_{0.67}Ca_{0.33}MnO_\delta$ effective valency of *Mn* is given as: $x = 2\delta - [3 \times 0.67 + 2 \times 0.33] = 2\delta - 2.67$. For optimal doping, $\delta = 3, x = 3.33$. If f is the concentration of Mn^{4+}, this can be expressed as a function of δ as $x = 2\delta - 2.67 = 3 + f$, so that $f = 2\delta - 5.67$).

The spin only atomic moment of Mn^{3+} (with $3d^4$configuration , crystal field level t_{2g}^3 , e_g^1) is 4 μ_B and that of Mn^{4+} (with d^3 configuration t_{2g}^3 , e_g^0) is $3\mu_B$. The change in the magnetic moment as a function of δ will thus be given as $\Delta\mu_{Mn} \approx -f\mu_B = -(2\delta - 5.67)\mu_B$. Increasing δ can enhance the hole concentration (Mn^{4+} concentration) and thus reduce the saturation moment of the bulk manganite. If the value of the bulk saturation moment M_{OS} is taken as $3.42\mu_B$ one can evaluate its value as a function of δ and it should decrease as δ increases. However, the observed data (this work) deviates from this simple estimate.

For nanoparticles, depression of M_S from the bulk value can arise from surface oxides that from a dead layer on the surface of the nanoparticles. This contributes to mass or volume but not to M_S and as a result the effective magnetization /unit volume or unit mass is smaller than the bulk value [13]. The following equation was used to find the dead layer thickness λ in a particle of diameter *d*:

$$M_S = M_{OS}\left(\frac{\frac{d}{2} - \lambda}{\frac{d}{2}}\right)^3$$

$$or,\ \lambda = \left\{1 - \left(\frac{M_S}{M_{OS}}\right)^{1/3}\right\}\frac{d}{2} \qquad (3.2)$$

, where M_{OS} is the spontaneous magetization for the bulk sample and for optimally doped sample of LCMO with $\delta \approx 3$, this is 3.42μ_B at 80 K [19]. From Eqn. 3.2 and the observed M_S and from the estimated M_{OS} one can evaluate the dead layer thickness (λ) as a function of δ. This is shown in FIG.3.8. As δ increases λ increases and becomes maximum at $\delta \approx 3$.For further increase of δ the value of λ reduces.

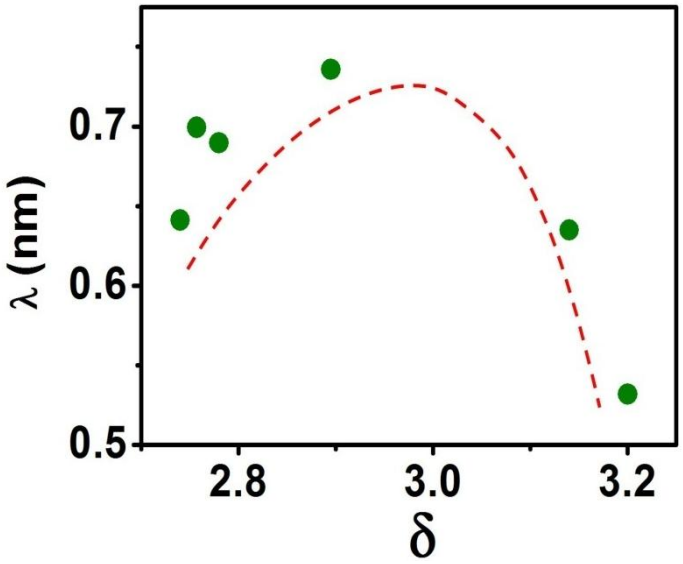

FIG. 3.8. Variation of shell thickness (λ) versus δ plot.

FIG.3.7 (b) shows that the value of M_S is minimum (~ 22.2 emu/g or 0.83 M_S/μ_B) around δ = 3. Considering the core-shell structure where shell is the magnetic dead layer (showed in previous work [13]) if the shell thickness becomes 2.47 nm, the ferromagnetism disappears for the particle size below 5 nm. Our work shows that the ferromagnetism persists even with the particle size ~ 4 nm. This result indicates that the shell thickness λ is much thinner ~0.6 $\pm$ 0.1 nm for smaller particles as opposed to ~ 2.5nm for particles with diameter 15nm.

It has been shown that [15] the spontaneous magnetization (M_S) for bulk $La_{0.67}Ca_{0.33}MnO_{\delta}$drops from ~ 3.5 μ_B/f.u (for δ =3) down to M_S ~1.75 μ_B/f.u (for δ = 2.94). The surprise is that the strongly reduced sample with δ = 2.80 has a larger high-field magnetic susceptibility than other reduced samples. It is difficult to determine M_S for the δ < 2.94 samples because the magnetization is not saturated in the available fields up to 70 kOe at 6K. Magnetization for the δ = 2.80 sample is around 4 μ_B/f.u. at field of 60 kOe (Taken from ref [15]).

For our case as δ differs from optimum value 3 (> or <) M_S increases. For nanomanganites this work shows that the saturation magnetisation can be measured over a wide range of δ change from 2.74 to 3.2 with much less magnetic field (~1.6 T) compared to the bulk system (~7 T) even at 80 K tempeature.

3.4 Discussion

The dependence of the ferromagnetic transition temperature (T_C) on δ is shown in FIG. 3.5(b). On initial oxidation T_C increases and shows a broad maximum around δ = 3. For δ > 3 it decreases again. T_C value of the reduced sample S^* (obtained after reduction of sample S_5) is situated on the same graph process showing reversibility of the electrochemical oxidation/reduction process.

The process of oxidation changes the *Mn-O-Mn* bond angle as can seen from FIG 3.3. (c). While the bond angle *Mn-O_1-Mn* remains mainly unaltered, the angle *Mn-O_2-Mn* increases sharply on initial oxidation and then decreases. Since the increase of the *Mn-O-Mn* bond angle will increase the orbital overlap, this will enhance the band width leading to enhancement of T_C which in a double exchange mechanism is directly related to the band-width. However, for δ > 2.9, the *Mn-O_2-Mn*angle decreases again but the enhancement of T_C continues till higher δ (~3) and then it decreases again. Thus the enhancement of T_C for $\delta \leq 3$ will not only depend on the change in the bond angle but also on other factors like the exchange constant and also likely on the dead layer thickness (λ). For δ > 3 the decrease of T_C is most likely is governed by the large decrease in the bond-angle *Mn-O_2-Mn*.

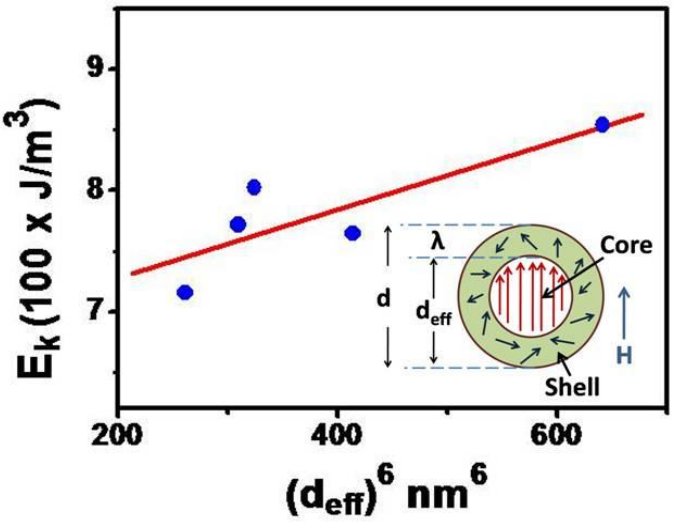

FIG. 3.9. Variation of anisotropy energy (E_K) vs. effective particle diameter d_{eff}. Inset shows the schematic diagram of core-shell structure of a particle.

The average magnetic anisotropy energy (E_K) of the samples has two parts. One is coming from the core part (K_1) and another one is coming from the shell part (K_2) of the particles. Therefore average anisotropy energy can be expressed by $E_K = K_1+K_2$. Since the shell part has random spins, saturation magnetization coming from that part is very small than core part. Anisotropy energy is proportional to the saturation magnetization and for that reason $K_1 >> K_2$ and $E_K \sim K_1$. If the particle diameter d is less than magnetic exchange length, it can be shown from the work of Herzer et. al. [20] that $E_K \propto d^6$. Here the main contribution of E_K is coming from K_1. The effective particle size is d_{eff} = (d-2λ). In this work the average particle diameter is d ~ 4 nm. We have calculated anisotropy energy $E_K = \frac{1}{2}\mu_0 H_C M_S$ [21] using the values of H_C and M_S as obtained from experiment. Plot of E_K and d_{eff} is shown in FIG. 3.9. Result showed that $E_K$varies as $(d_{eff})^6$.This concludes that whatever is the individual dependence, the product of H_C and M_S follows the nano-magnetic properties.

3.5 Conclusions

We made pure phase $La_{0.67}Ca_{0.33}MnO_{\delta}$ nanoparticle of average grain size around 4 nm and analyzed the crystal structure. Orthorhombic strain becomes very large due to very small particle size. Though the particle size is very small, the ferromagnetism persists even in this small size. This result contradicts the earlier report where it has been proposed (based on results of 15nm particle) that ferromagnetism will disappear particle size less than 5 nm due to the fact that dead layer thickness that may become comparable to particle size. We find that in smaller nanoparticles the dead layer has smaller thickness (~1nm or less) as a result the ferromagnetism can be sustained.

This investigation is first report where the effects of oxidation on nanoparticle (~ 4 nm particle size) on magnetic properties have been studied. The samples were oxidized electrochemically at room temperatures which ensured that the particle size remains the same before and after the oxidation. Very small particle size makes it possible to carry out large change in oxidation from δ = 2.74 to δ = 3.20 due to faster diffusion. The ferromagnetic T_C, it becomes maximum around δ = 3 where the particles are saturated by oxygen ions and all vacancies are filled up. Further incorporation of oxygen ions distorts the $Mn{-}O_2{-}Mn$ bond angle which effectively decreases the value of T_C. Since the reduction results δ race the same oxidation path it shows that the process is reversible.

The shell thickness (λ) increases as δ reaches near the value 3 and further increment of δ value again decreases the shell thickness. The average anisotropy energy E_K of the sample is proportional to the sixth power of the effective diameter, $d_{eff} = d - 2\lambda$.This behavior confirms that d_{eff} is smaller than the magnetic exchange length of $La_{0.67}Ca_{0.33}MnO_{\delta}$ sample.

References:

1. S. V. Trukhanov, L. S. Lobanovski, M.V. Bushinsky, V. A. Khomchenko, N.V. Pushkarev, I.O. Troyanchuk, A. Maignan, D. Flahaut, H. Szymczak, and R. Szymczak, *Eur. Phys. J. B.* **42**, 51 (2004).
2. Y. G. Zhao, W. Cai, J. Zhao, X. P. Zhang, B. S. Cao, M. H. Zhu, L.W. Zhang, S. B. Ogale, TomWu, T. Venkatesan, Li Lu, T. K. Mandal, and J. Gopalakrishnan, *Phys. Rev. B.* **65**, 144406 (2002).
3. L. Malavasi, G. Flor, *J.Phys.Chem B.* **107(50)**, 13880 (2003).
4. Zhang, X. Yao, X. H. Zeng, *Phys.Stat.Sal.(a)201*. **10**, 2305 (2004).
5. Alina Manzoor, S. K. Hasanain, A. Mumtaz, M. F. Bertino, L. Franzel, *J Nanopart Res*. **14**, 1310 (2012).
6. I. L. Zhogin, A. P. Nemudry, P. V. Glyanenko, Yu. M. Kamenetsky, H. J. M. Bouwmeester, Z. R. Ismagilov, *Catalysis in Membrane Reactors*. **118**, 151 (2006).
7. L. E. Hueso, F. Rivadulla, R. D. Sanchez, D. Caeiro, C. Jardon, C. Vazquez-Vazquez, J. Rivas and M. A. Lopez- Quintela, *Journal of Magnetism and Magnetic Materials*. **189**, 321 (1998).
8. Jean Pierre Locquet, Frederic Arrouy, Erich Macheer, Michel Despont, Peter Bauer, Erica J Williams. *Appl. Phys. Let*. **68**, 14 (1996).
9. Jean Pierre Locquet. *Physica C*. **263**,160-163 (1996).
10. V. Pralong, V. Caignaert, S. Hebert, C. Marinescu, B. Raveau, A. Maignan, *Solid State Ionics*. **177**,815-820 (2006).
11. M. D. Carvalho, A. Wattiaux, J. M. Bassat J. C. Grenier, M. Pouchard, M. I. da Silva Pereira, F. M. A. Costa. *J Solid State Electrochem*. **7**,700-705 (2003).
12. H. H. Feng, Z. G. Li, P. H. Hor, S. Bhavaraju, J. F. Di Carlo, A. J. Jacobson. *Phys. Rev. B*, (*Rapid communications*). **51**, 22 (1995).
13. Tapati Sarkar, A. K. Raychaudhuri, A. K. Bera and S. M. Yusuf. *New J. Phys*. **12**, 123026 (2010).
14. R. Mahendiran, S. K. Tiwary, A. K. Raychaudhuri, T. V. Ramakrishnan, R. Mahesh, N. Rangavittal, and C. N. R. Rao. *Phys. Rev. B*, **53**, 3348 (1996).
15. S. V. Trukhanov, N. V. Kasper, O. Troyanchuk , M. Tovar, H. Szymczak, K. Barner, *Journal of Solid State Chemistry*. **169**, 85–95(2002).
16. R. D. Shannon. *Acta Crystallogr. A*. **32**, 751(1976).
17. S.-W. Cheong and H. Y. Hwang, *Ferromagnetism vs Charge/Orbital Ordering in Mixed-Valent Manganites, in Colossal Magnetoresistance Oxides*, edited by Y. Tokura (*Gordon & Breach, Monographs in Condensed Matter Science, London*, 1999).
18. K. Shantha Shankar, Sohini Kar, G. N. Subbanna, A. K. Raychaudhuri. *Solid State Communications*. **129**, 479–483(2004).
19. Tapati Sarkar, *Tuning of ground state and phase transition in complex oxide nanomaterials, Chapter 3, S.N.Bose National Centre for Basic sciences* (2009).
20. G. Herzer. *IEEE Transactions On Magnetics*. **26**, 5(1990).
21. *Physics of Ferromagnetism*, 2nd ed., edited by S. Chikazumi (*Oxford University Press*, 1999).

Chapter 4

Dependence of physical properties of half-doped manganite nanoparticles (average diameter:~5nm) on electrochemically controlled Oxygen stoichiometry: Role of cation A-site disorder

In this work we have investigated the physical properties of half doped manganite $A_{0.5}Ca_{0.5}MnO_{\delta}$ nanoparticles to oxygen stoichiometry δ by keeping the same particle size after oxygen incorporation in the system. The oxygen incorporation (oxidation) was done by electrochemical oxidation at room temperature that allows the oxygen stoichiometry δ to be changed precisely without change of particle size. We find that the physical properties (structural, magnetic and electrical) of the half-doped manganite nanoparticles as well as their sensitivities to oxidation depend crucially on cation disorder (quantified by variance $\sigma^2$of ionic radii of ions in A site). When half-doped manganite nanoparticles are hole doped and δ is made > 3, there exists a critical cationic disorder (σ_C) so that for $\sigma > \sigma_C$ the oxidation process enhances the ferromagnetic transition temperature T_C and the density of state at Fermi level. The content and scope of this investigation is new.

4.1Introduction

Physical properties of perovskite oxides can be controlled by tuning of oxygen stoichiometry [1]. Tuning of oxygen concentration in these systems (bulk and film) is an emerging field of work due to its technological application in solid-oxide fuel cell [2]. These studies were done by heat treatment (> 500^0C) with different oxygen partial pressure where oxygen ions are diffused inside the oxide system [1,3-4]. Thermal oxidation is the easiest process to control oxygen stoichiometry. However, this process has the inherent problem that it also changes size of the nanoparticles and in some cases even the crystal symmetry. If these are of no concern, as may happen in some cases, then thermal oxidation is a viable process.

However, in case of manganite nanoparticles (referred to as nanomanganites) where the physical properties not only depend on the stoichiometry (δ) but also on the particle size (diameter *d*), the process of thermal oxidation has limited scope to carry a clean investigation as both δ as well as *d* would change on heat treatment. This is most severe in half-doped nanomangaites ($A_{0.5}Ca_{0.5}MnO_{\delta}$, A being rare-earth) which will be investigated in this chapter. We have used electrochemical oxidation, as described in earlier chapters, to circumvent this problem and carried out a precise change in δ in half-doped nanomanganites with average d ~ 5nm in samples with varying cationic radii. We have carried out structural, magnetic and electrical measurements in them. We made an important new observation that the sensitivity of the physical properties to oxidation depends on the cation disorder as quantified by the variance σ^2. It is observed that there exists a critical value of $\sigma^2(=\sigma_C^2)$ so that for, $\sigma^2 > \sigma_C^2$ the oxidation (i.e hole doping) leads to enhancement of the ferromagnetic T_C , bandwidth (ω) and density of states at the Fermi level N(E_F). Interestingly for $\sigma^2 < \sigma_C^2$ the opposite changes happen or they are suppressed. The oxidation (while retaining the crystal symmetry of the nanoparticles) changes the lattice parameters as well.

In ABO_3 perovskites like the manganites, distortion of crystal structure depends on the cation radius ($< r_A >$) [5,6]. The A-site cation mismatch is quantified by the variance $\sigma^2 = \sum_i y_i r_i^2 - < r_A >^2$ and r_i is the individual cation radius of A-site cation, $y_i$is the occupancy (fractional) of species i with $\sum_i y_i = 1$, $< r_A >$ is the weighted average of cationic radii. In $A_{0.5}Ca_{0.5}MnO_{\delta,}$ $< r_A > \equiv 0.5r_A(A) + 0.5r_A(Ca),$ being the ionic radii of ion A and Ca respectively as obtained from [7]. There are reports [8,9] which showed that electronic and magnetic properties of manganite sample has a dependence on σ^2. In TABLE 4.I we have tabulated the values of $< r_A >$ and σ^2 with sample IDs.

TABLE 4.I. $< r_A >$ and $\sigma^2$of different samples are summarized.

Sample $A_{0.5}Ca_{0.5}MnO_{\delta}$	**$< r_A >$ (A^0)**	**σ^2 $(A^0)^2$**
S_1 (A=Y)	1.128	2.76X 10^{-3}
S_2 (A=Sm)	1.156	5.76X 10^{-4}
S_3 (A=Nd)	1.172	7.23 X 10^{-5}
S_4 (A=Pr)	1.180	2.50 X10^{-7}
S_5 (A=La)	1.198	3.24X 10^{-4}

In FIG. 4.1 we plot σ^2 as a function of $< r_A >$. The dependence is not monotonous. It can be seen that for the smallest cation Y, σ^2 is the largest and it becomes smallest for Nd and Pr that have similar sizes as Ca and then it increases again as size of La becomes larger than that of Ca.

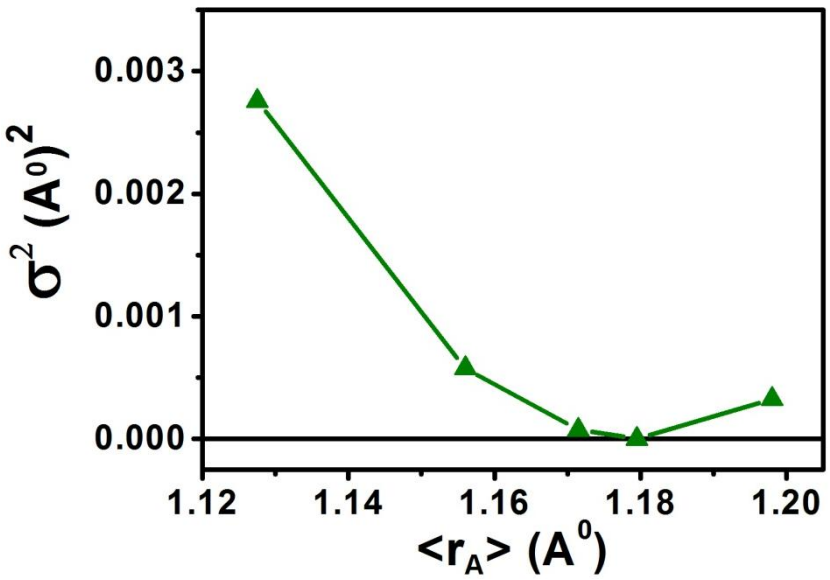

FIG. 4.1. The σ^2 dependence with $< r_A >$.

The phase diagram of nanomanganites and the magnetic order sensitively depends on size of the nanoparticles. As showed in Chapter 3(as well by past studies in our group [6,10-12] that in optimally doped manganites like $La_{0.67}Ca_{0.33}MnO_3$ the T_C is substantially enhanced when the partcicle size is reduced. This is particularly severe in half-doped ($A_{0.5}Ca_{0.5}MnO_\delta$) nanomanganites, where it has been shown [6,11,13] that the charge and orbitally ordered insulating state (with Antiferrromagnetic order) gets destabilized giving rise to ferromagnetic low resistance state with particle sizes below 15 nm. The destabilization of charge and orbitally ordered state depends on the rare-earth cationic size [6].

In this work we have focused to study the change of physical properties (structural, magnetic and electrical) by tuning of oxygen concentration in half- doped manganite nano particle systems of different cation sizes ($< r_A >$).The oxygen concentration was changed by electrochemical oxidation method at 300 K. The oxygen concentration δ was changed from ~3 to 3.2 for a system of particle size ~ 5(±1) nm. We investigated whether the sensitivities of the physical properties to oxidation by a given amount have any dependence of the cationic size or on the disorder that arises from cation size mismatch as quantified by the variance σ^2 defined above.

4.2Experimental

The experiments were done on half doped $A_{0.5}Ca_{0.5}MnO_\delta$ with A = Y, Sm, Nd, Pr, La trivalent rare earth elements. We have prepared pure phase nanomanganites ($S_1, S_2, S_3, S_4$and S_5) with different average ionic radius $< r_A >$ of the A-site ions by Chemical solution deposition(CSD) method described before in Chapter 2 [14]. Electrochemical oxidation method, described in details in Chapter 2, has been used to oxidize the samples. After oxidation the samples are identified as S_1^*, S_2^*, S_3^*, $S_4^*$and S_5^*, respectively where the oxygen stoichiometry (δ) changes from their as prepared starting δ values. The summery of oxygen stoichiometry of different samples (before and after oxidation) are tabulated in TABLE 4.IIa. The change in oxygen stoichiometry ($\Delta\delta$) for different methods with variance (σ^2) are tabulated in TABLE 4.IIb.

TABLE 4.IIa. Details of the samples used in this work and the electrochemical control of oxygen stoichiometry. Sample IDs are *S* (as prepared) and S^* (oxidized).

Sample $A_{0.5}Ca_{0.5}MnO_\delta$	**$\langle r_A \rangle$ (A^0)**	***S***	**δ (S) (Rietveld refinement)**	**δ (S) (Iodometric titration)**	**S^***	**δ (S^*) (Rietveld refinement)**	**δ (S^*) (Iodometric titration)**
$Y_{0.5}Ca_{0.5}MnO_\delta$	1.127	S_1	2.96(±0.010)	2.95(±0.02)	S_1^*	3.18(±0.021)	3.19(±0.02)
$Sm_{0.5}Ca_{0.5}MnO_\delta$	1.156	S_2	2.97(±0.020)	2.96(±0.02)	S_2^*	3.22(±0.020)	3.21(±0.02)
$Nd_{0.5}Ca_{0.5}MnO_\delta$	1.172	S_3	2.99(±0.021)	2.98(±0.02)	S_3^*	3.24(±0.021)	3.23(±0.02)
$Pr_{0.5}Ca_{0.5}MnO_\delta$	1.180	S_4	2.95(±0.031)	2.96(±0.02)	S_4^*	3.17(±0.065)	3.22(±0.02)
$La_{0.5}Ca_{0.5}MnO_\delta$	1.198	S_5	2.98(±0.026)	2.97(±0.02)	S_5^*	3.23(±0.026)	3.23(±0.02)

TABLE 4.IIb. Variance (cationic radius difference) and change in stoichiometry brought about by electrochemical oxidation $\Delta\delta = \delta(S^*) - \delta(S)$.

Sample $A_{0.5}Ca_{0.5}MnO_\delta$	**Variance $\sigma^2(A^0)^2$**	**$\Delta\delta(S)$ (Rietveld refinement)**	**$\Delta\delta(S)$ (Iodometric titration)**	**$\Delta\delta$ (Faraday Law)**
$Y_{0.5}Ca_{0.5}MnO_\delta$	$2.76X\ 10^{-3}$	0.22	0.24	0.216
$Sm_{0.5}Ca_{0.5}MnO_\delta$	$5.76X\ 10^{-4}$	0.25	0.25	0.258
$Nd_{0.5}Ca_{0.5}MnO_\delta$	$7.23\ X\ 10^{-5}$	0.25	0.25	0.254
$Pr_{0.5}Ca_{0.5}MnO_\delta$	$2.50\ X\ 10^{-7}$	0.22	0.26	0.252
$La_{0.5}Ca_{0.5}MnO_\delta$	$3.24X\ 10^{-4}$	0.25	0.26	0.250

The phase was confirmed from X-ray diffraction (XRD) results. We used Energy dispersive X-ray (EDX) spectroscopy results to check the composition. The particle size was confirmed from Transmission Electron Microscope (TEM) images as well as from Williamson-Hall plot [15] from XRD. The particle size (d) and micro strain (ε) of the system is related with the Full width half maximum (β) as,

$$\frac{\beta cos\theta}{\lambda} = \frac{1}{d} + \varepsilon \frac{2sin\theta}{\lambda} \tag{4.1}$$

, where λ = 0.1518 nm is the wave length of Cu Kα and θ is the XRD peak angle. In FIG. 4.2. (a) and 4.2. (b) XRD results and Williamson-Hall plot is shown. In FIG. 4.3. (a),(b) particle size distribution plot from TEM is shown. In TABLE 4.III comparison of particle size obtained from XRD and TEM tabulated. From Williamson-Hall plot we get average particle size which is always greater than the actual particle size (Obtained from TEM). Because the particles are so small they attached with each other and make bigger particles as shown in the FIG. 4.2. (c). XRD see these particles as single particle of bigger size. Williamson-Hall plot method gives the average particle diameter, as a result the discrepancy of particle sizes obtained from TEM and XRD arise. During sonication to make samples for TEM, the conglomerate breaks giving rise to smaller particles that are seen by TEM.

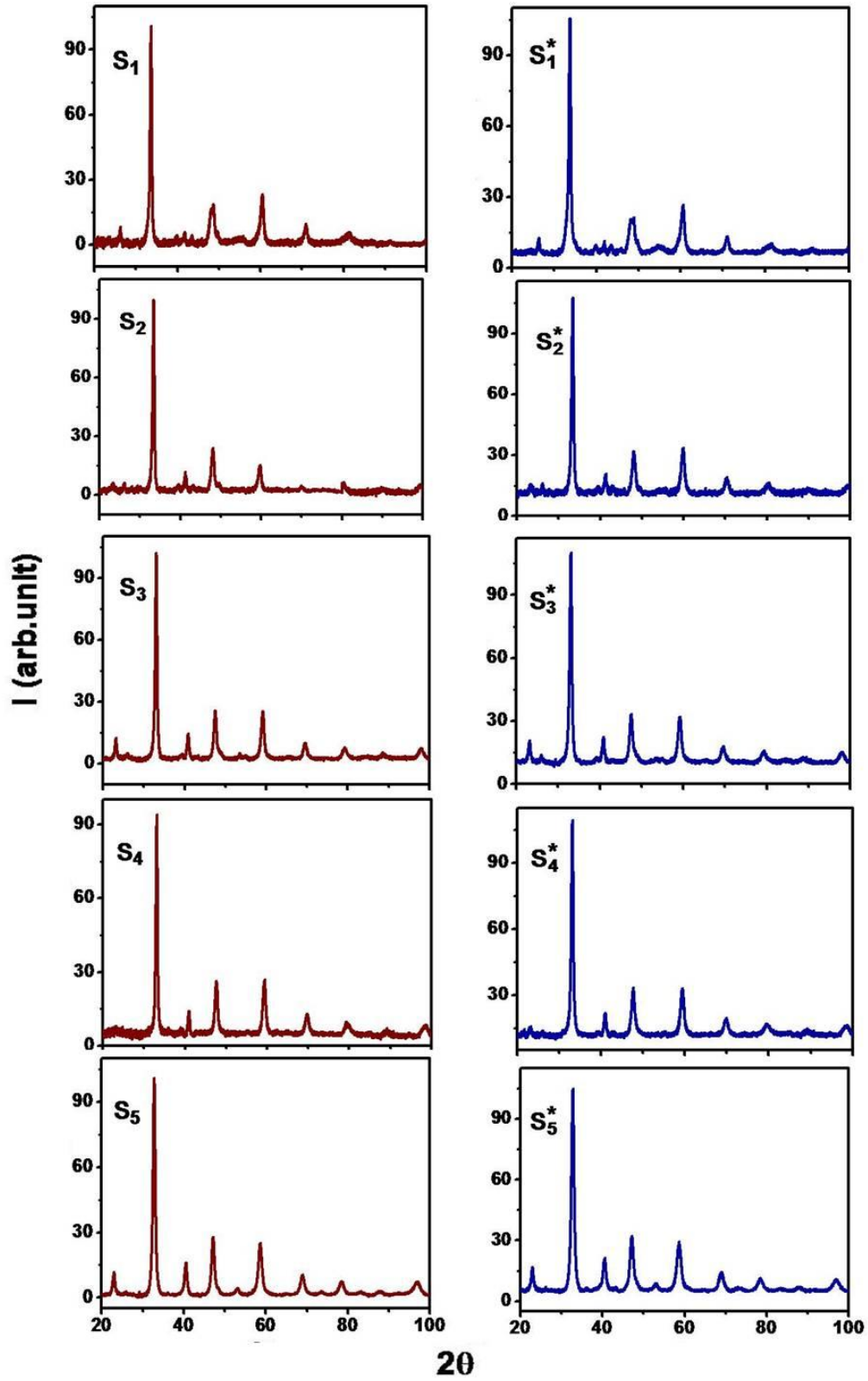

FIG. 4.2. (a). The XRD of *S* and *S** samples.

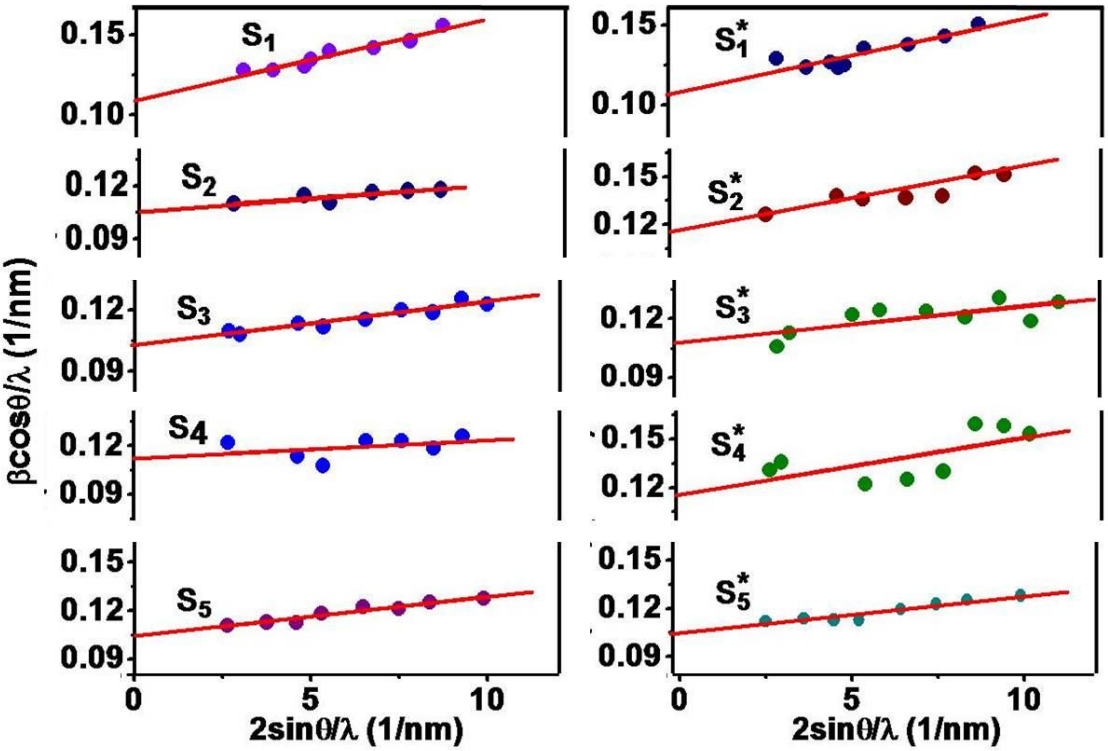

FIG. 4.2. (b). Williamson hall plot of *S* and *S** samples.

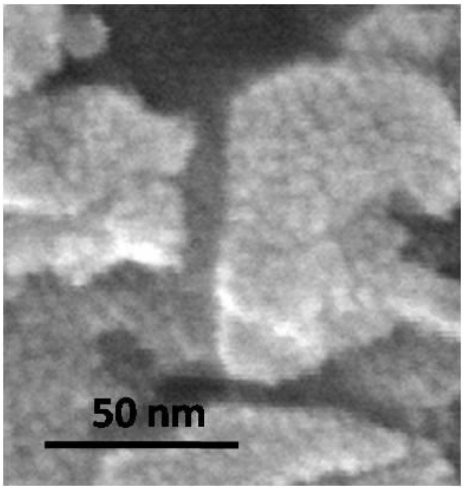

FIG. 4.2. (c). Scanning electron microscope image of S_1 sample. A large lump of particle is created by the small particles.

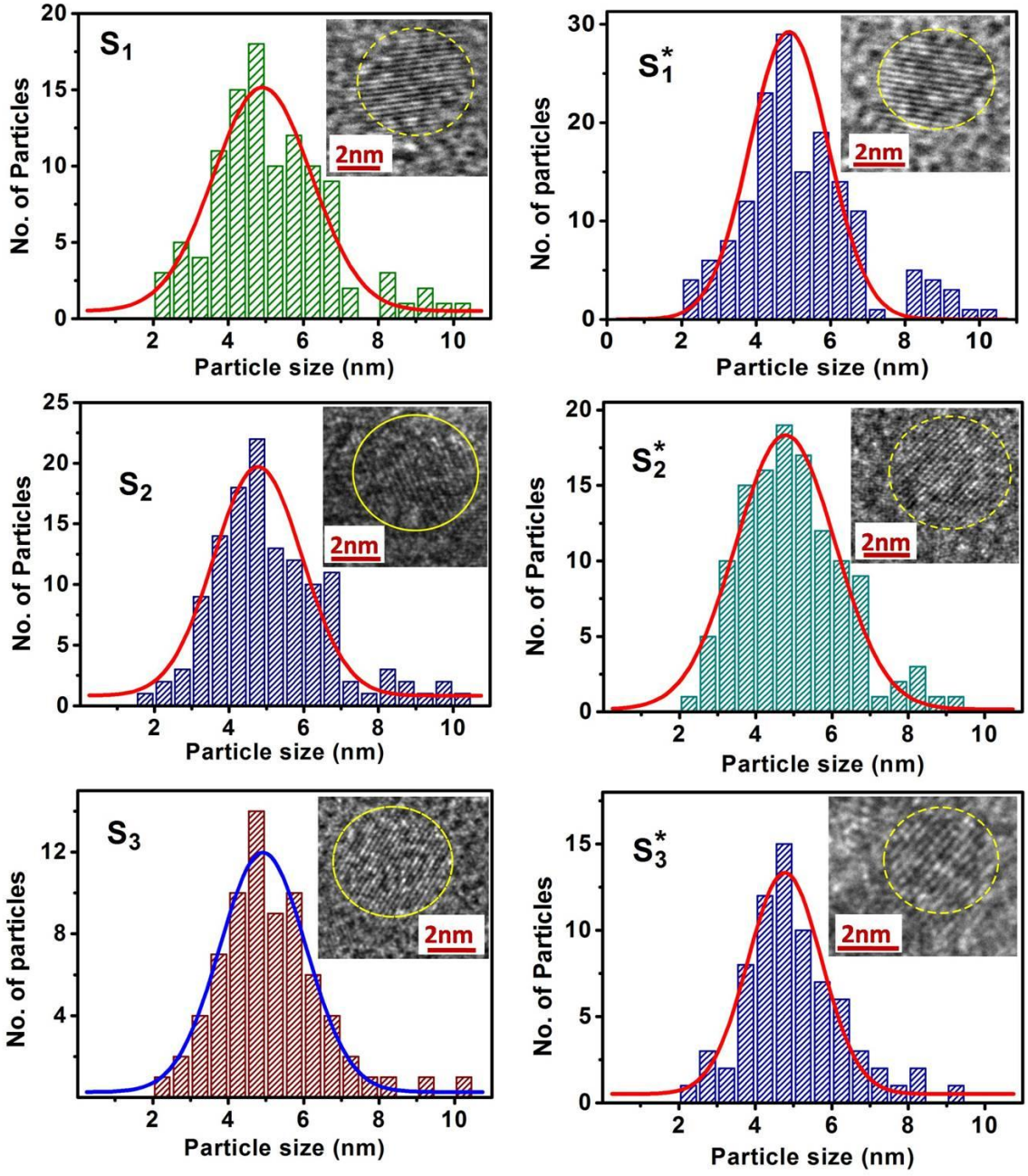

FIG. 4.3. (a).The Particle size distribution plot of S_1,S_1^*, S_2, S_2^*, S_3, S_3^*samples. Inset shows single particle TEM images of respective samples.

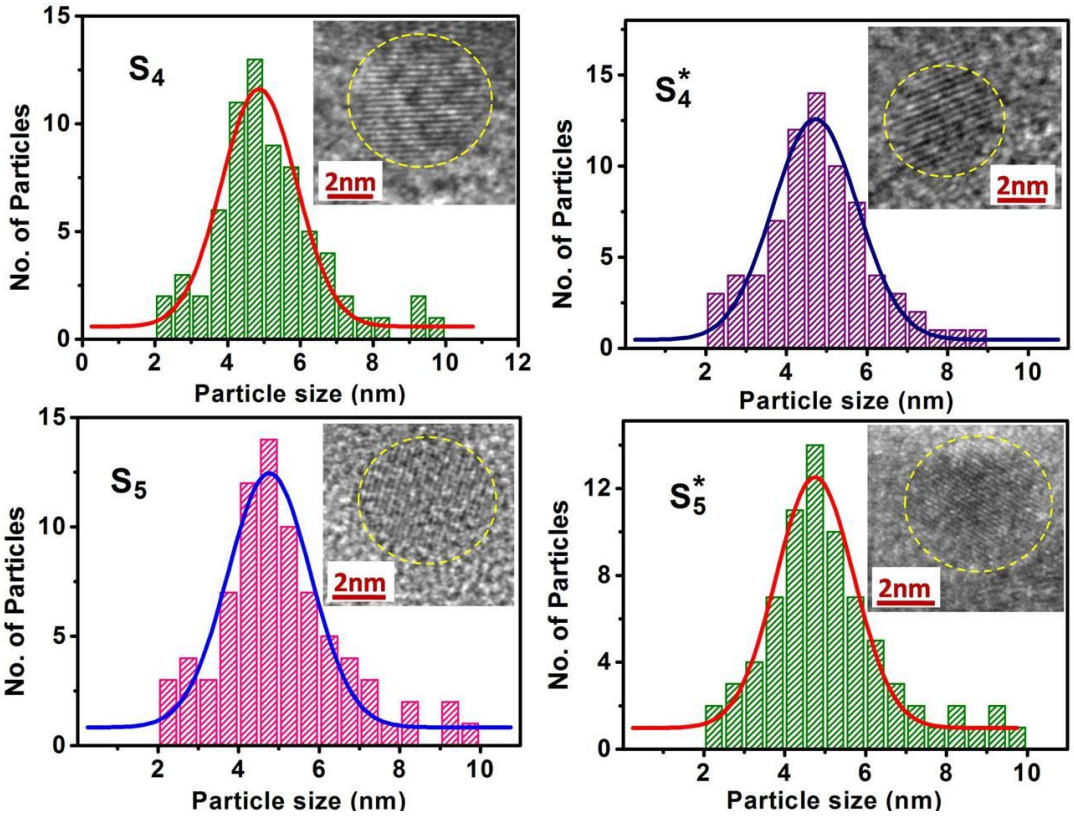

FIG. 4.3. (b).The Particle size distribution plot of S_4, S_4^*, S_5, S_5^* samples. Inset shows single particle TEM images of respective samples.

TABLE 4.III. Particle size from XRD and TEM as well as micro strain obtained from XRD.

ID	*d*(nm) from XRD	*d*(nm) from TEM	Micro strain (ε)	ID	*d*(nm) from XRD	*d*(nm) from TEM	Micro strain (ε)
S_1	9.1(±0.2)	4.8(±0.10)	$5.0X10^{-3}$ ($\pm5X10^{-4}$)	S_1^*	9.4(±0.4)	4.9(±0.10)	$4.0X10^{-3}$ ($\pm8X10^{-4}$)
S_2	9.4(±0.2)	4.8(±0.10)	$1.4X10^{-3}$ ($\pm3X10^{-4}$)	S_2^*	8.7(±0.9)	4.8(±0.06)	$4.2X10^{-3}$ ($\pm2X10^{-4}$)
S_3	9.7(±0.1)	4.9(±0.06)	$2.1X10^{-3}$ ($\pm2X10^{-4}$)	S_3^*	9.3(±0.4)	4.8(±0.06)	$2.2X10^{-3}$ ($\pm7X10^{-4}$)
S_4	8.9(±0.5)	4.9(±0.07)	$1.1X10^{-3}$ ($\pm1X10^{-4}$)	S_4^*	8.7(±0.8)	4.7(±0.06)	$3.6X10^{-3}$ ($\pm1X10^{-4}$)
S_5	9.6(±0.1)	4.8(±0.08)	$2.5X10^{-3}$ ($\pm2X10^{-4}$)	S_5^*	9.7(±0.2)	4.8(±0.07)	$2.5X10^{-3}$ ($\pm3X10^{-4}$)

It is noted that the microstrains in the as grown nanoparticles as well as those in oxygenated particles are of the same order. However, for two samples they are somewhat larger.

We fitted the XRD results for every sample by Rietveld Refinement technique with orthorhombic Pnma space group and got the crystal structure parameters and oxygen stoichiometry (δ). The δ values are cross checked from Iodometric titration results and the difference in δ value for each pair of samples (S and S^*) was checked from Faraday law. These values are tabulated in TABLE 4.IIb.The magnetization measurements were done in a vibrating sample magnetometer (VSM) with field range up to 1.6 T and temperature range

from 80 K to 350 K. Conventional collinear four probe method was used to measure the resistivity of the samples. For temperature dependent resistivity measurement (3 K to 300 K) a closed cycle pulsed tube Helium cryostat was used.

4.3Results and Discussions

4.3.1 Orthorhombic distortions and Crystal structure

In FIG 4.2 (a) XRD data of every sample is plotted, which confirm the proper phase formation for each sample. The spatial variation of stoichiometry for all samples was checked from energy dispersive X-ray analysis (done in TEM) which shows A:Ca ratio 1.01(± 0.03). For every sample studied in this work the mean particle size is ~ 4.7(±0.2) nm, obtained from particle size distribution graph of TEM images. Also particle size obtained from Williamson-hall fitting of equation (4.1) is ~ 9.5(±0.2) nm. In TABLE 4.III shows the comparison of particle size obtained from XRD and TEM.

From TEM images it is confirmed that the particle sizes after oxidation are same as before room temperature oxidation. Single particle TEM image of each sample is shown in the inset of distribution plots of FIG. 4.3. (a),(b). All samples show orthorhombic Pnma structure. The lattice parameters *a*, *b*, *c*, bond angles (*Mn-O_1-Mn* and *Mn-O_2-Mn*) and bond distances (*Mn-O_1* and *Mn-O_2*) are calculated from Rietveld refinement of the XRD results. The average orthorhombic distortion parameter *D*is defined as,

$$D = \frac{100}{3}\sum_{i=1,2,3}\frac{|a_i - a_{avg}|}{a_{avg}} \qquad (4.2)$$

, where, $a_{avg} = (abc)^{1/3}/\sqrt{2}$.

The value of D of the bulk sample gradually increaseswith the decrease of $< r_A >$ for the half doped manganitesystems. In the half doped family the system with smallest cation (Y^{3+}) has the largest distortion (1.35 %). In FIG. 4.4.(a) we plot *D*as a function of $< r_A >$ for both the bulk as well as nanosamples . In FIG. 4.4. (b) we also show *D* as a function of variance σ^2.

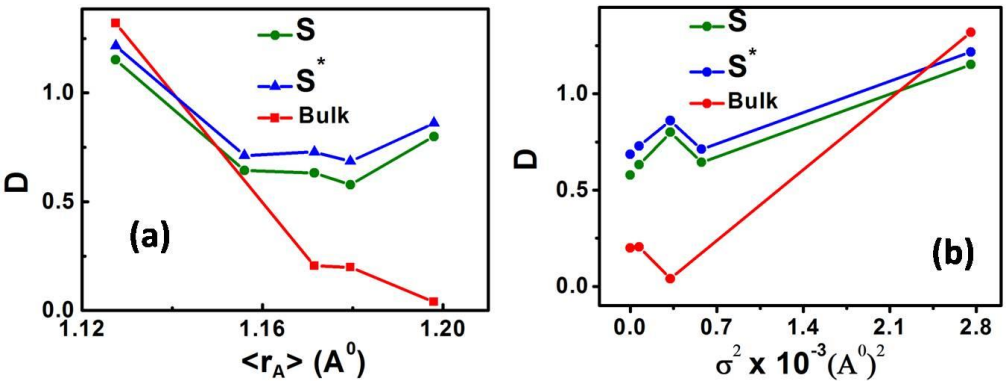

FIG. 4.4. (a) Distortion parameter *D* plotted as a function of the average ionic radius $< r_A >$for half-doped manganites, for Bulk, nano and oxidized nano samples. The ions in order of decreasing ionic radii are La, Pr, Nd, Sm and Y. *D* for the bulk samples have been taken from the work of Chowdhury et. al. [6]. **(b)**Variation of *D* with σ^2.

Some results have been taken from the references mentioned in the caption of the FIG.4.4. (a). Results show that the *D* for larger cationic radius (La) sample is nearly 8 times larger in nano sample than that in its bulk counterpart. For smallest cationic radius (Y) *D*is comparable for both the nano and bulk samples. The value of *D* that

arises due to large cationic size mismatch in the samples with large σ^2 and small $< r_A >$ is more than that arises from size reduction. In contrast for samples with larger $< r_A >$ and small σ^2 the distortion due to size reduction dominates [6]. In these samples the value of D is larger than the bulk counterpart and they stay high at ~ 0.75 %. Importantly, the value of D is always larger in the oxidized nano samples than the as prepared samples although the difference is smaller. The oxidation introduces the Oxygen atoms in the system leading to somewhat enhanced distortion.

Small but distinct enhancement in D on oxygenation implies that the oxygen incorporation into the samples make subtle changes in the crystal structure. FIG. 4.5. (a) and 4.5. (c) shows the $Mn-O-Mn$ bond angle (θ) and $Mn-O$ bond distances (u) for samples of different $< r_A >$. FIG. 4.5. (b) and 4.5. (d) shows the $Mn-O-Mn$ bond angle (θ) and $Mn-O$ bond distances (u) for samples of different σ^2.In the $Y_{0.5}Ca_{0.5}MnO_3$ system θ for $Mn-O_1-Mn$ drastically buckle to ~ 121^0. Oxygen incorporation recovers the angle to ~ 172^0. We will observe later on that this has an effect on transport as well as magnetic properties. The process of oxidation makes small enhancement for $Mn\text{-}O_1\text{-}Mn$ and small decrements for $Mn\text{-}O_2\text{-}Mn$.The bond angles are insensitive of oxidation for the largest cationic system like $La_{0.5}Ca_{0.5}MnO_3$. The bond distances are maximum for the middle element $Nd_{0.5}Ca_{0.5}MnO_3$. FIG. 4.6 shows that the increase of $< r_A >$ increases the unit cell volume (V). Oxidation makes the bond length $Mn\text{-}O_1$ somewhat larger (although opposite happens for the sample $Y_{0.5}Ca_{0.5}MnO_3$) and the bond-length $Mn\text{-}O_2$ becomes somewhat smaller on oxidation.

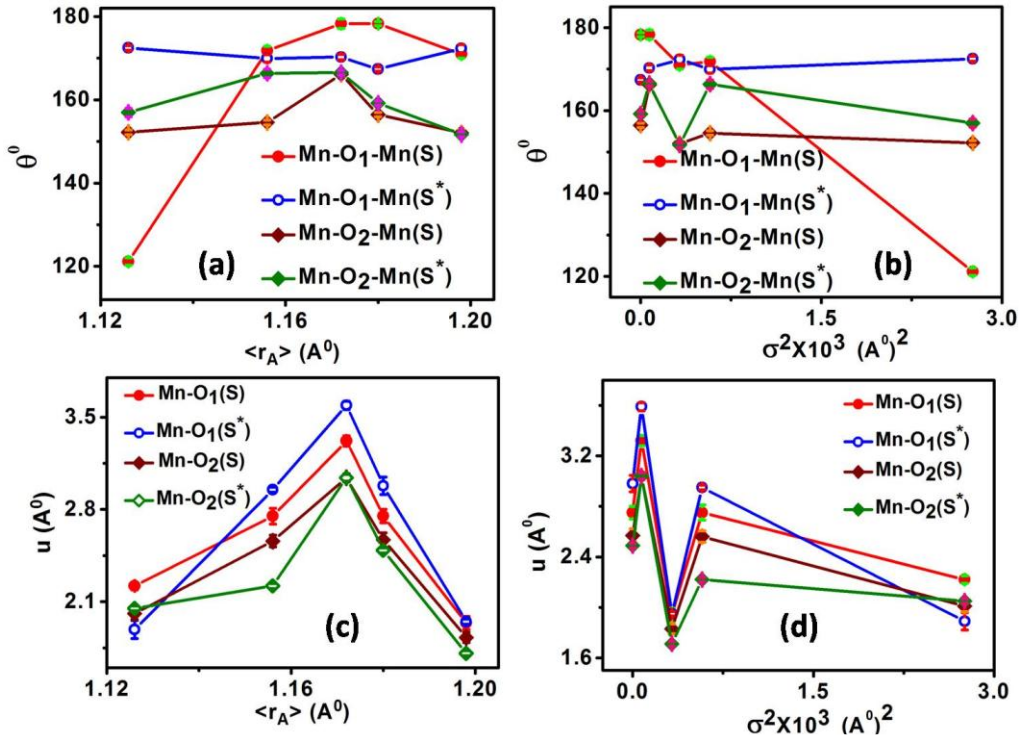

FIG. 4.5. (a).Variation of bond angles with $< r_A >$. (b).Variation bond angles with σ^2. (c).Variation of bond distances with$< r_A >$. (d).Variation of bond distances with σ^2 (The error bars are plotted with symbols).

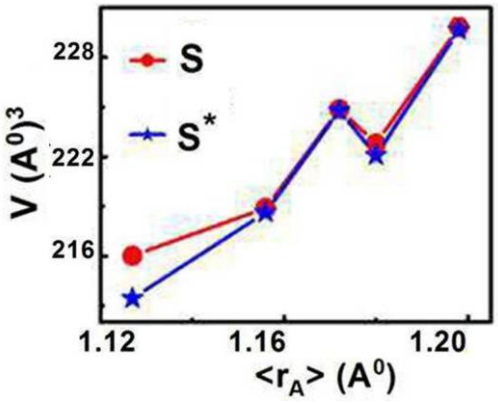

FIG. 4.6. Variation of unit cell volume (V) with $< r_A >$.

We define the average bond length $u_{avg} = [u(Mn - O_1) + u(Mn - O_2)]/2$. After oxidation, the opposing changes in *Mn-O₁-Mn* and *Mn-O₂-Mn* lead to small changes in u_{avg}. The changes in the bond angles ($\Delta\theta^0$) are quantified as Δ *Mn-O₁-Mn* = *Mn-O₁-Mn* (S^*) − *Mn-O₁-Mn*(S) and Δ *Mn-O₂-Mn* = *Mn-O₂-Mn* (S^*) − *Mn-O₂-Mn*(S). The changes in the bond distances (Δu) are estimated as$\Delta u(Mn - O_1) = u(Mn - O_1)(S^*) - u(Mn - O_1)(S)$,$\Delta u(Mn - O_2) = u(Mn - O_2)(S^*) - u(Mn - O_2)(S)$, $\Delta u_{avg} = u_{avg}(S^*) - u_{avg}(S)$. In FIG. 4.7 we plotted the changes in the bond angles and bond distances with both $< r_A >$ and σ^2.

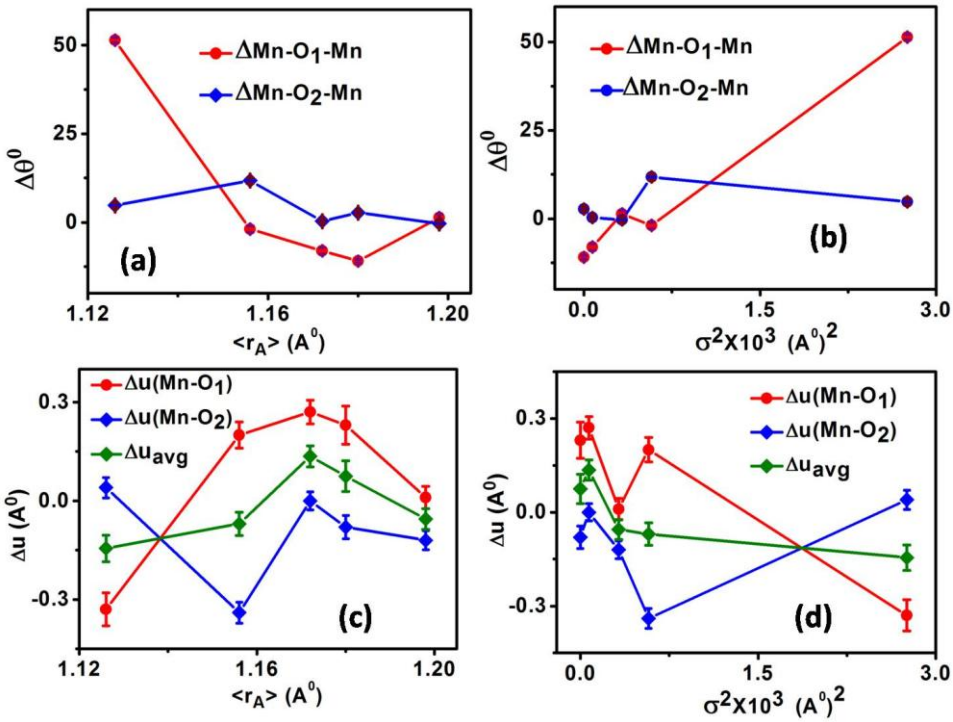

FIG. 4.7. (a) Variation of $\Delta\theta^0$ with $< r_A >$. (b) Variation of $\Delta\theta^0$ with σ^2. (c) Variation of Δu with $< r_A >$. (d) Variation of Δu with σ^2 (The error bars are plotted with symbols).

4.3.2 Dependence of Resistivity on oxidation:

Resistivity (ρ) as a function of temperature were measured in the samples before and after oxidation. All the samples are insulating in nature throughout the measuring

temperature range up to 300 K. In FIG. 4.8. (a) − (j) the $\rho - T$ data for all samples are shown before and after oxidation. The resistivity (ρ) of the *S** sample (oxidized) is larger than the *S* sample (as grown).The $\rho - T$ curves were fitted with the Mott variable range hopping (VRH) model [16-17]. According to the VRH model $\rho(T)$ can be expressed as:

$$\rho = \rho_0 \, e^{\left(\frac{T_0}{T}\right)^{1/4}} \tag{4.3}$$

, where $\rho_0$and T_0 are constants. The data fitted to VRH equation are shown FIG. 4.8. (a) − (j). From the fitting we measured the value of T_0 which can be defined as [16],

$$K_B T_0 = \frac{18}{N(E)\xi^3} \tag{4.4}$$

,where N(E) is the density of states at the Fermi level and ξ is the localization length which can be considered as the average bond distance u_{avg} for strongly localized systems like the half-doped manganites. In TABLE 4.IV the values of the parameters ρ_0, T_0 ,N(E) and $\xi(= u_{avg})$ as obtained from equation (4.3) and (4.4) for as grown and oxidized samples are given.

TABLE 4.IV. Values of ρ_0, T_0, N(E) and $\xi(= u_{avg})$ for different samples.

Sample-ID	$\boldsymbol{\rho_0}$ **(Ωm)**	$\boldsymbol{T_0}$ **(K)**	**N(E) X 10^{25} ($eV^{-1}m^{-3}$)**	$\boldsymbol{\xi(= u_{avg})}$ **(A^0)**
S_1	2.62 x 10^{-10}	1.55 x 10^8	14.24	2.115
S_2	1.02 x 10^{-8}	9.67 x 10^7	11.53	2.655
S_3	8.38 x 10^{-10}	1.89 x 10^8	3.42	3.180
S_4	3.01 x 10^{-9}	1.38 x 10^8	8.03	2.660
S_5	3.51 x 10^{-11}	2.12 x 10^8	14.68	1.885
S_1^*	1.76 x 10^{-9}	1.71 x 10^8	15.94	1.970
S_2^*	2.41 x 10^{-8}	1.03 x 10^8	11.73	2.585
S_3^*	1.02 x 10^{-9}	1.95 x 10^8	2.93	3.315
S_4^*	3.87 x 10^{-9}	1.43 x 10^8	7.12	2.735
S_5^*	1.92 x 10^{-10}	2.14 x 10^8	14.77	1.875

It can be seen from TABLE 4.IV. that after oxidation the value of T_0 increases for all the samples. In FIG.4.9.(a) we show the plot of change in T_0, $\Delta T_0 = T_0(S^*) - T_0(S)$ as obtained after oxidation. This shows that the change in T_0 is maximum for the lowest cation size sample $Y_{0.5}Ca_{0.5}MnO_3$. The ΔT_0 value gradually decreases with the increment of the A-site cation size and it is minimum for $La_{0.5}Ca_{0.5}MnO_3$.

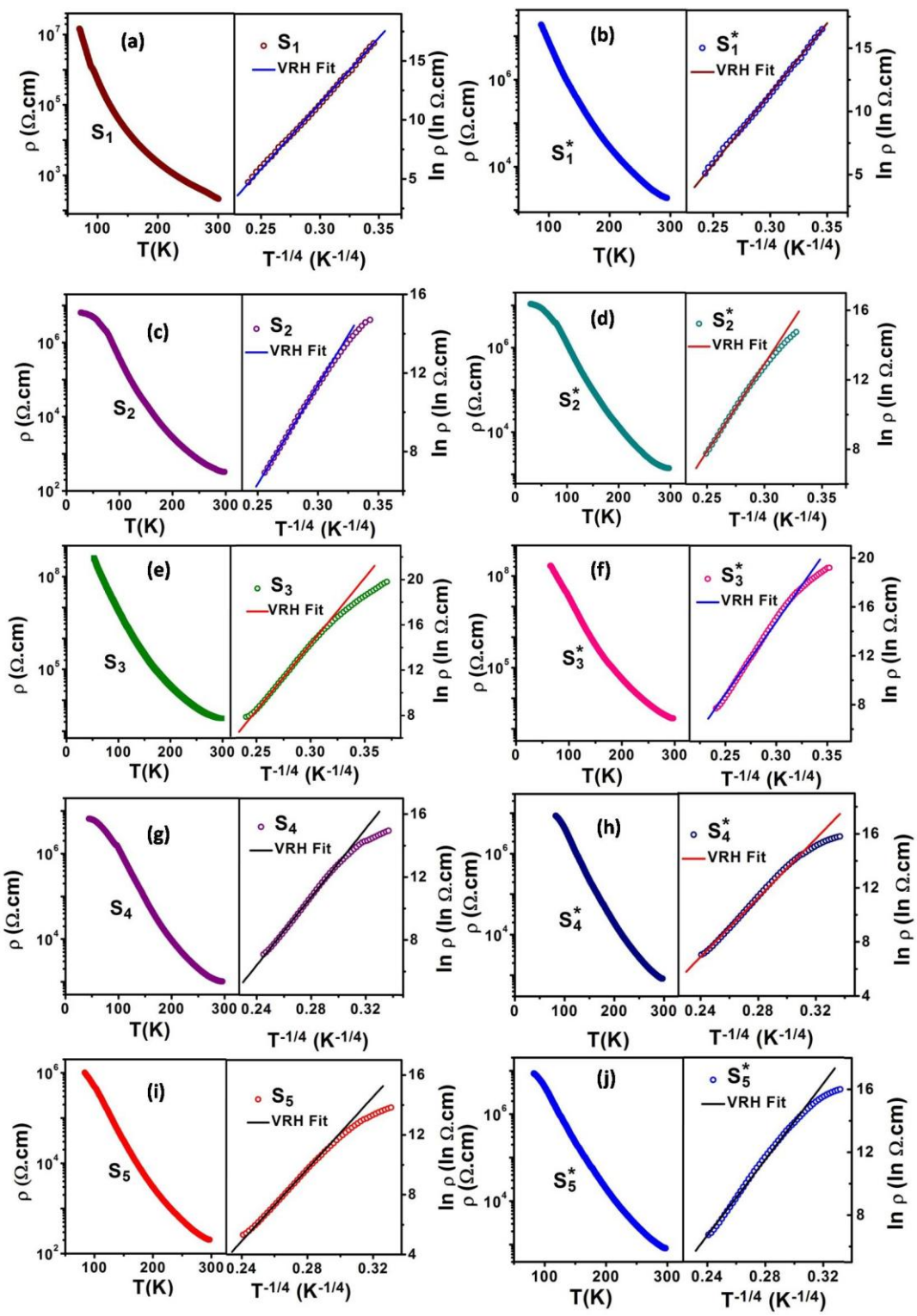

FIG. 4.8. Resistivity versus temperature plot with variable range hopping fitting for samples (a) S_1 (b) S_1^* (c) S_2 (d) S_2^* (e) S_3 (f) S_3^* (g) S_4 (h) S_4^* (i) S_5 (j) S_5^*.

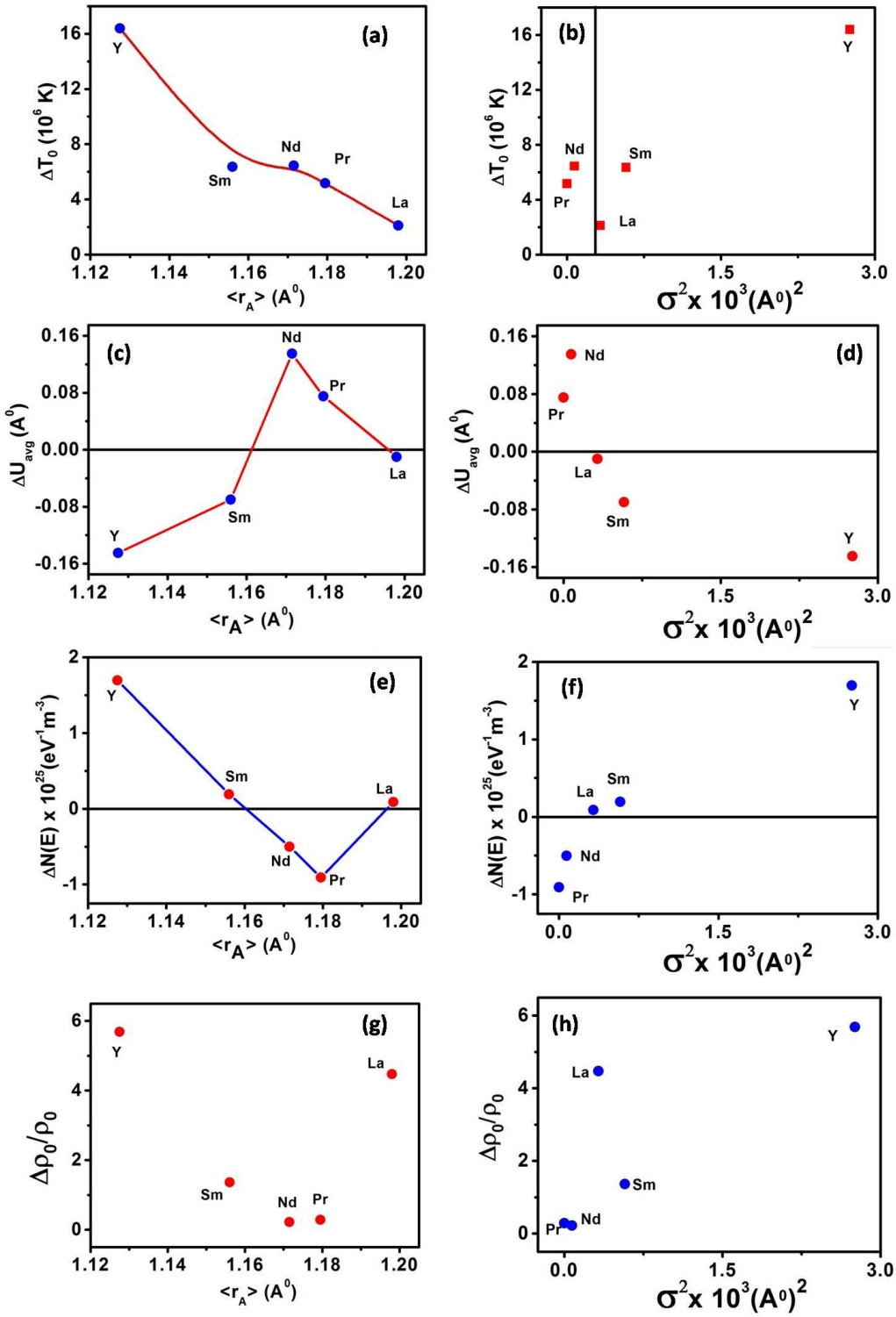

FIG. 4.9. (a) ΔT_0 change with $< r_A >$ (b) ΔT_0 change with σ^2(c) Variation of Δu_{avg} with $< r_A >$ (d) Variation of Δu_{avg} with σ^2 (e) ΔN(E)change with $< r_A >$ (f) ΔN(E)change with σ^2. (g) $\Delta\rho_0/\rho_0$ change with $< r_A >$ (h) $\Delta\rho_0/\rho_0$ change with σ^2.

In FIG.4.9.(b) ΔT_0 is plotted against σ^2. It can be seen that the dependence of ΔT_0 on σ^2 is discontinuous at $\sigma^2 = \sigma_c^2$ (marked as black line in the curve). Changes in

localization lengths ($\Delta u_{avg} = u_{avg}(S^*) - u_{avg}(S)$) which we link to the increment of the average bond length $\xi(= u_{avg})$, depend on the σ^2value (FIG.4.9. (f)). For the samples which have larger σ^2values like $La_{0.5}Ca_{0.5}MnO_3$, $Sm_{0.5}Ca_{0.5}MnO_3$ and $Y_{0.5}Ca_{0.5}MnO_3$, u_{avg} decreases after oxidation and $\Delta u_{avg} < 0$. Similarly for the samples like $Nd_{0.5}Ca_{0.5}MnO_3$ and $Pr_{0.5}Ca_{0.5}MnO_3$ which have smallerσ^2, the change of bond length $\Delta u_{avg} > 0$ or u_{avg} increases after oxidation. Using the value of T_0 and u_{avg} we determine the value of N(E) (See TABLE 4.IV.) from equation (4.4) and correspondingly $\Delta N(E) = N(E)^* - N(E)$. N(E) is smaller for the samples which have smaller value of σ^2. The variation ΔN(E) with $< r_A >$ isshown in FIG.4.9. (e). After oxidation the change in the density of state N(E) again depends on σ^2 (FIG.4.9.(f)). For the samples which have larger $\sigma^2$the change $\Delta N(E) > 0$ for smaller σ^2samples $\Delta N(E) < 0$. 11.7% increment on the value of N(E) after oxidation for $Y_{0.5}Ca_{0.5}MnO_3$. 14.7% decrement on the value of N(E) after oxidation for $Nd_{0.5}Ca_{0.5}MnO_3$. . Δu_{avg} changes oppositely with ΔN(E) as plotted with respect to the $< r_A >$ as shown in FIG.4.9. (c) and FIG.4.9. (e). The variation $\Delta\rho_0/\rho_0$ with $< r_A >$ isshown in FIG.4.9. (g) and its variation with σ^2 is shown in FIG.4.9. (h). For the samples which have larger $\sigma^2$the change $\Delta\rho_0/\rho_0 > 1$ for smaller σ^2samples $\Delta\rho_0/\rho_0 < 1$.

4.3.3 Magnetic phase transition temperature

The size reduction in half-doped manganites causes qualitative changes in the magnetic order. It has been shown [6,10-12] that the size reduction beyond few tens of nm destabilize the CO-OO ordered state that also has antiferromagnetic (AFM) spin order. This leads to onset of ferromagnetic order in the nanoparticles of half-doped manganites. In this chapter we investigate what happens to the magnetism in half-doped manganites on electro-chemical oxidation when the size of the nanoparticles is in the range of ~ 5nm.

To find the magnetic phase transition temperatures we plot $1/\chi$ vs. T curve (FIG.4.10.(a) −(j)). From the fitting of the relation $\chi = C/(T - \Theta)$. we found the transition temperature Θ and the Curie constants. For ferromagnetic (FM) sample Θ is the Curie temperature T_C. Form the plot we identify the Curie temperature T_C and the spin values (μ_{eff}) from the Curie constant (C) using the relation, $C = {\mu_{eff}}^2/3k_B$.We found the value of T_C of all the half doped nano samples (as grown and after oxidation) and the results are tabulated in TABLE 4.V. For every sample after oxidation μ_{eff} value decreases, only for $Sm_{0.5}Ca_{0.5}MnO_3$ slight increment in the value of μ_{eff} is observed.

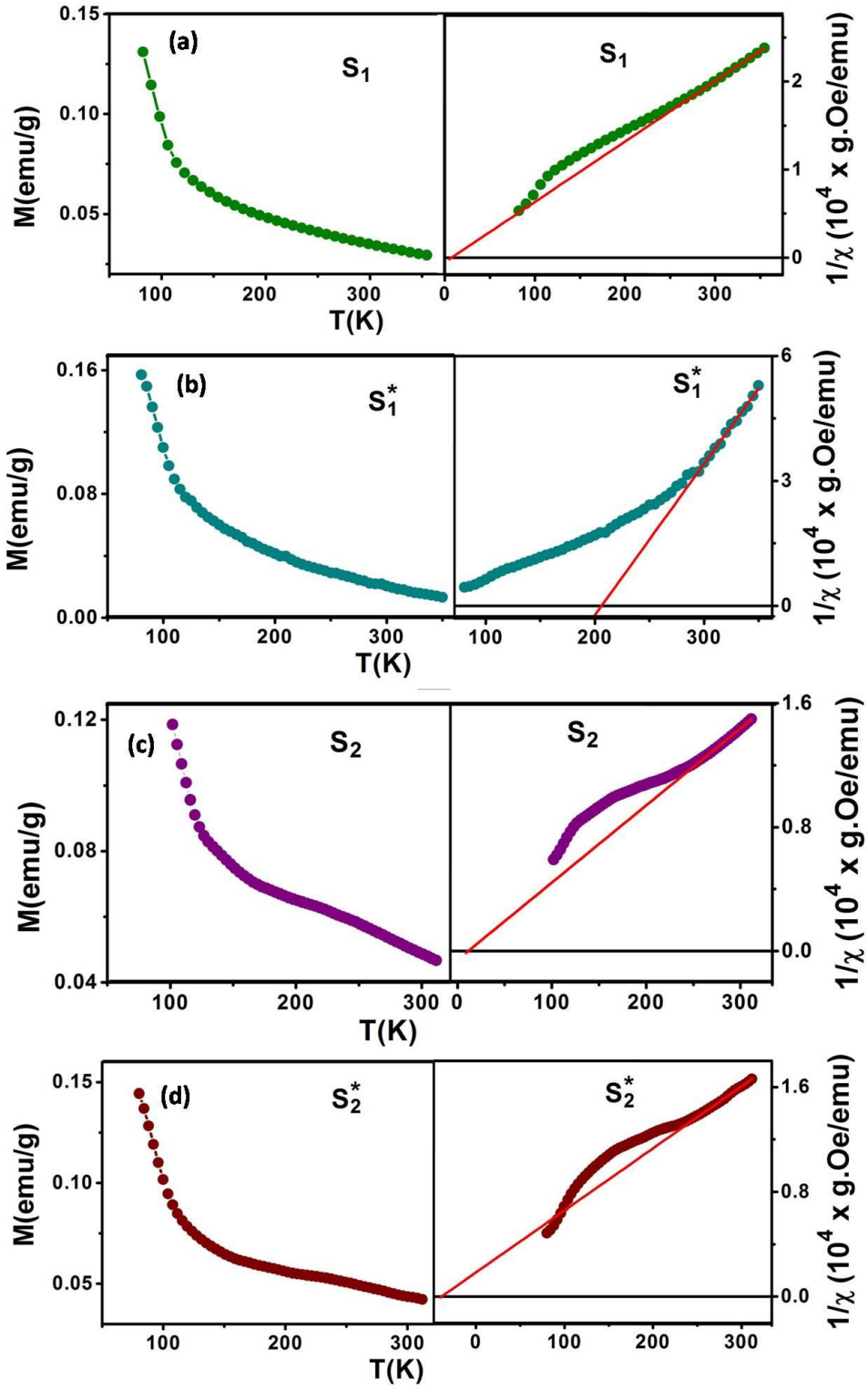

FIG. 4.10. Magnetisation versus temperature plot at a field 0.07 T and $1/\chi$ vs. temperature fitting of samples (a) S_1 (b) S_1^* (c) S_2 (d) S_2^*.

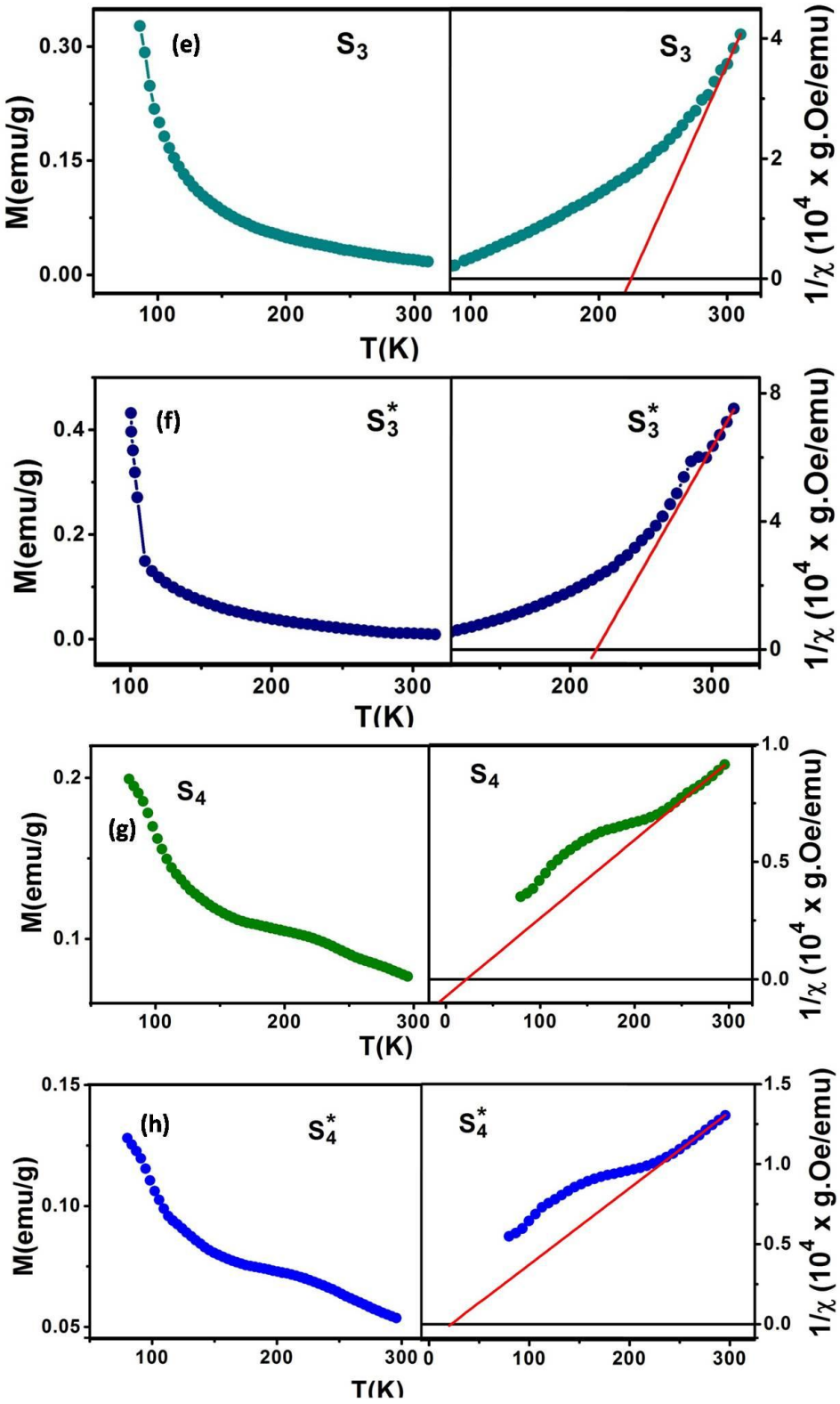

FIG. 4.10. Magnetisation versus temperature plot at a field 0.07 T and $1/\chi$ vs. temperature fitting of samples (e) S_3 (f) S_3^* (g) S_4(h) S_4^*.

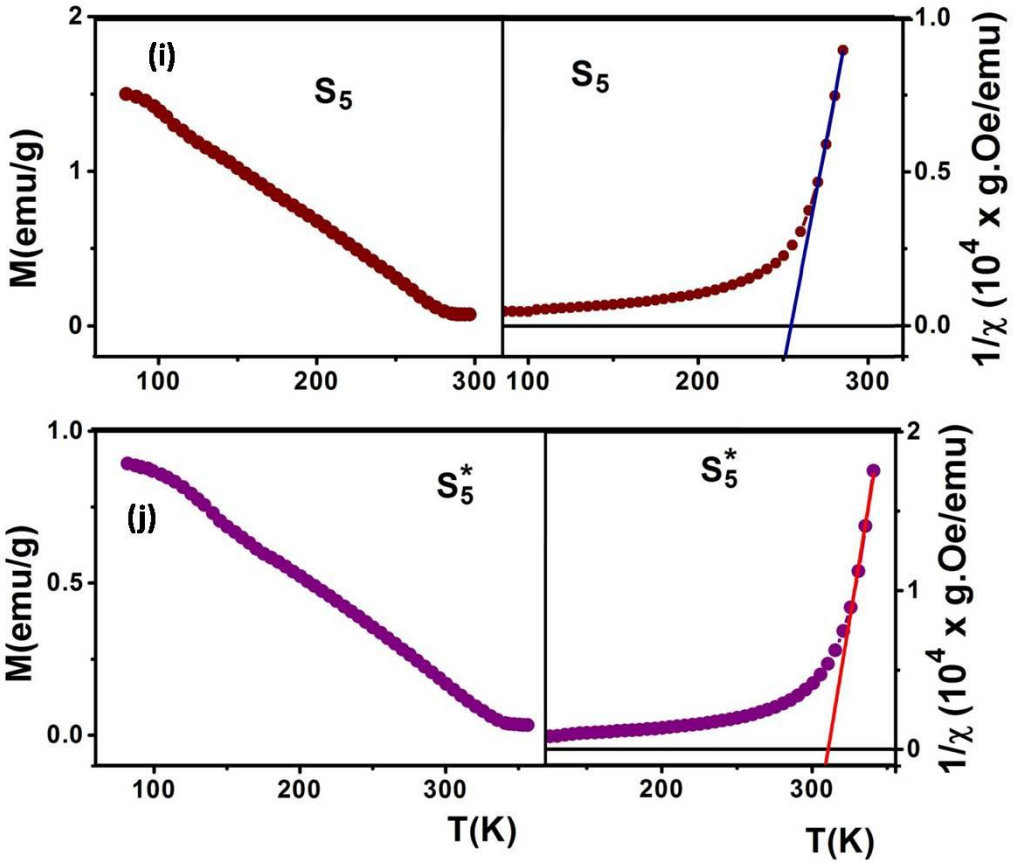

FIG. 4.10. Magnetisation versus temperature plot at a field 0.07 T and $1/\chi$ vs. temperature fitting of samples (i) S_5 (j) S_5^*.

TABLE 4. V. Magnetic transition temperatures (Θ) and effective magnetic moment (μ_{eff}) of half doped manganite nanostructure sample of grain size ~5 nm.

Sample-ID	**Θ (*S*) K**	$\mu_{eff}(S)(\mu_B)$	**Θ (S^*) K**	$\mu_{eff}(S^*)(\mu_B)$
$Y_{0.5}Ca_{0.5}MnO_3$	7.4	0.342	205.6	0.149
$Sm_{0.5}Ca_{0.5}MnO_3$	11.2	0.401	−38.9	0.411
$Nd_{0.5}Ca_{0.5}MnO_3$	225.2	0.130	218.5	0.102
$Pr_{0.5}Ca_{0.5}MnO_3$	22.2	0.489	21.3	0.410
$La_{0.5}Ca_{0.5}MnO_3$	254.6	0.166	310.7	0.118

The change of T_C for the sample which is defined as $\Delta T_C = T_C(S^*) - T_C(S)$. A plot of ΔT_C as a function of variance of cationic disorder $< r_A >$ and $\sigma^2$is shown in FIG. 4.11 (a) and FIG. 4.11 (b).

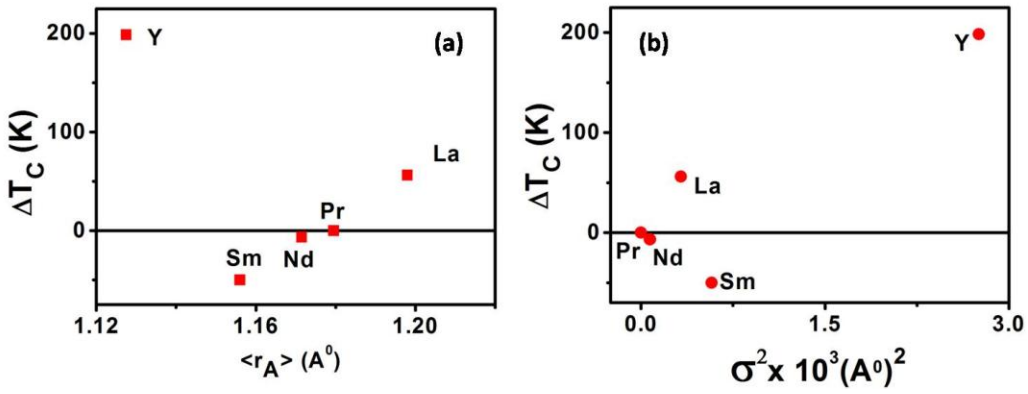

FIG. 4.11. (a) ΔT_C change with $< r_A >$ (b) ΔT_C change with σ^2.

Most spectacular change occurs for the sample with smallest A-site cation and largest variance σ^2 namely $Y_{0.5}Ca_{0.5}MnO_3$. In this sample oxidation leads to a large upward change in T_C. The T_C for the unoxidized sample is ~7.4 K and it changes to nearly 205 K on oxidation. In fact it becomes positive for the samples that are σ^2 large. Again for the samples which have smaller σ^2 ferromagnetic transition temperature decreases and ΔT_C becomes negative.

4.3.4 Change in conduction band width and its impact on the changes in transport and magnetic behaviour

In rare-earth manganites the ferromagnetic order and the electric transport are related and the physical quantity that makes the link is the band-width. The band width in its turn is related to the structural parameters like *Mn-O-Mn* bond angle. Closer the bond is to 180^0 (as it happens in a cubic structure) larger is the band width. This will have an impact on the observed physical properties. In this sub-section we make the interesting observation that the observed changes in some of the physical properties on oxidation are linked to the variance of cationic disorder σ^2which itself has a clear link to the change in the band width on oxidation.

In the manganite system the electronic conduction and magnetic properties are strongly depend on the $e_g$electron band width ω. This band width (ω) in a double exchange interaction is related to the average $Mn-O-Mn$ bond angles ($Mn-O1-Mn$) and ($Mn-O2-Mn$). We define the average angle as:

$$< \theta >= \frac{(Mn-O1-Mn)+(Mn-O2-Mn)}{2} \qquad (4.5)$$

The band width is proportional to the deviation of $< \theta >$from π and $\omega \propto [Cos\{(\pi - < \theta >)/2\}]/u_{avg}^{3.5}$, [5]. After oxidation the band width of the samples are changed since both the parameters (related to stricture) $< \theta >$ and u_{avg} change with oxidation. The changes can be obtained from the structural information and can be converted into fractional changes in the band width:

$$\frac{\Delta\omega}{\omega} \equiv \frac{\omega(S^*)-\omega(S)}{\omega(S)} \qquad (4.6)$$

We plot the ratio $\Delta\omega/\omega$ as a function of σ^2 in FIG. 4.12. We find that the change in the band width has an almost linear dependence on σ^2so that,

$$\frac{\Delta\omega}{\omega} = \left(\frac{\Delta\omega}{\omega}\right)_0 + \mathcal{M}\sigma^2 \tag{4.7}$$

Where the $(\Delta\omega/\omega)_0$value of $\Delta\omega/\omega$ is the value when $\sigma^2 \to 0$, as is expected in an ideal perovskite structure with no A site cationic disorder for the change of oxygen stoichiometry. The value of $(\Delta\omega/\omega)_0$ and slope $\mathcal{M}$depends on the oxygen stoichiometry change $(\Delta\delta)$. There is a critical value of variance $\sigma_c^2 = 0.0035(A^0)^2$ at which $\Delta\omega/\omega = 0$.

This critical value separates the half doped system in two categories. For the samples like $Y_{0.5}Ca_{0.5}MnO_3$, $Sm_{0.5}Ca_{0.5}MnO_3$ and $La_{0.5}Ca_{0.5}MnO_3$ which have $\sigma^2 > \sigma_c^2$ the value of $\Delta\omega/\omega > 0$ i.ethe conduction bandwidth increases after oxidation. On the other hand, for the samples $Nd_{0.5}Ca_{0.5}MnO_3$ and $Pr_{0.5}Ca_{0.5}MnO_3$ which have $\sigma^2 < \sigma_c^2$ the bandwidth decreases after oxidation as and $\Delta\omega/\omega < 0$. This band width "tuning" by oxidation has its effect on the electronic and magnetic properties of the samples.

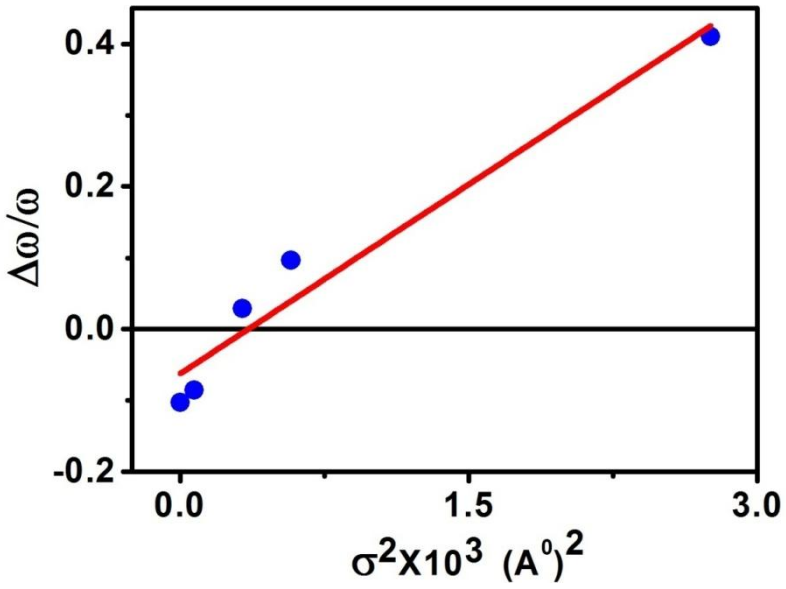

FIG. 4.12. $\Delta\omega$ vs. σ^2 for the half doped nano system. Linear fit is shown by red colour line.

In double exchange the ferromagnetic transition $T_C \propto \omega$ and enhanced band width favours the double exchange interaction and stabilizes the FM state. This can be seen from TABLE 4.V and figure FIG. 4.11.(b).We find that for materials like Y and La doped systems where, $\sigma^2 > \sigma_c^2$, $\Delta\omega/\omega > 0$ and T_C enhances after oxidation. This is spectacular for the Y substituted sample and quite large even for the La substituted sample. For Nd and Pr which have $\sigma^2 \leq \sigma_c^2, \Delta\omega/\omega \leq 0$ leading to small suppression of T_C on oxidation. For samples which have $\sigma^2 > \sigma_c^2$, $\Delta\omega/\omega > 0$, N(E) increases after oxidation like Y, La and Sm, on the other hand for samples $\sigma^2 \leq \sigma_c^2$, $\Delta\omega/\omega \leq 0$, N(E) decreases after oxidation like in Pr and Nd as shown in FIG. 4.9.(f).

4.4Conclusions

This is the first work on the controlled oxygen stoichiometry change in the nano particles (particle size 5(±1 nm)) of the half doped perovskite system. The stoichiometry change has been done at room temperature without changing the particle size. Our result shows that the changes in the structural and physical properties are strongly dependent only on the cation size disorder (σ^2) along with the average cation size $< r_A >$. After oxidation the bandwidth (ω) changes and the change $\Delta\omega/\omega$ is linearly dependent on the σ^2. There is a critical value σ_c^2= 0.0035 $(A^0)^2$. The samples are categorized by there σ^2 value. For the samples with $\sigma^2 > \sigma_c^2$ like $Y_{0.5}Ca_{0.5}MnO_3$ and $La_{0.5}Ca_{0.5}MnO_3$, after oxidation density of state N(E) and Curie temperature (T_C) both are increased. These physical parameters are decreased for the samples ($Nd_{0.5}Ca_{0.5}MnO_3$ and $Pr_{0.5}Ca_{0.5}MnO_3$) which have $\sigma^2 < \sigma_c^2$.

References:

1. Y. G. Zhao, W. Cai, J. Zhao, X. P. Zhang, B. S. Cao, M. H. Zhu, L. W. Zhang, S. B. Ogale, Tom Wu, T. Venkatesan, Li Lu, T. K. Mandal and J. Gopalakrishnan, *Phy. Rev. B.* **65**, 144406 (2002).
2. San Ping Jiang, *J Mater. Sci*. **43**, 6799 (2008).
3. L. Malavasi and G. Flor, *J. Phys. Chem B.* **107**(**50**), 13880 (2003).
4. H. Zhang, X. Yao, X. H. Zeng, *Phys. Stat. Sal.(a)201*. **10**, 2305 (2004).
5. C. N. R. Rao, Anthony Arulraj, P. N. Santosh and A. K. Cheetham, *Chem. Mater*. **10**, 2714(1998).
6. Putul Malla Chowdhury, Barnali Ghosh, A. K. Raychaudhuri, S. D. Kaushik and V. Siruguri, *J Nanopart.* Res. **15**, 1585 (2013).
7. R. D. Shannon, *Acta Crystallogr. A.* **32**, 751(1976).
8. G. Venkataiah, V. Prasad and P. Venugopal Reddy, *J. Alloys and Compounds*. **429**, 1 (2007).
9. Lide M. Rodriguez-Martinez and J. Paul Attfield, *Phy. Rev. B.* **54**, R15622 (1996).
10. Tapati Sarkar, A. K. Raychaudhuri and Tapan Chatterji, *Appl. Phys. Let*. **92**, 123104 (2008).
11. Tapati Sarkar, Barnali Ghosh, A. K. Raychaudhuri and Tapan Chatterji, *Physical Review B.* **77**, 235112 (2008).
12. Tapati Sarkar, P. K. Mukhopadhyay and A. K. Raychaudhuri, *J. Appl. Phys*. **101**, 124307 (2007).
13. S. M. Zhou, L. Shi, H. P. Yang, Y. Wang, L. F. He and J. Y. Zhao, *Appl. Phys. Let*. **93**, 182509 (2008).
14. K. Shanta Shankar and A. K. Raychaudhuri, *J. Mater. Res*. **21**, 27 (2006).
15. G. K. Williamson and W. H. Hall, *Acta Metallurgica*. **1**, 22 (1953).
16. M.Viret, L. Ranno and J. M. D. Coey, *J. Appl. Phys*. **81**, 4964 (1997).
17. N. F. Mott, *Philosophical Magazine*. **19**, 835 (1969).

Chapter 5

Migration of Oxygen by electric field in submicron strips of $La_{0.85}Sr_{0.15}MnO_3$

In this work we show that oxygen ions/vacancies can be made to migrate over a finite length even at room temperature (in a submicron strip of an oxide $La_{0.85}Sr_{0.15}MnO_3$ nanowire) when a sufficiently high-density current is applied. This process leads to change in local oxygen stoichiometry which in turn leads to nearly 90 % drop in electrical resistance, where the current flow drives oxygen ions through it. In this experiment in the oxide strip, by electrochemical oxidation process a localized source of oxygen rich region was created, using lithographic process to define the region for electrochemical oxidation. For a DC-current of density $J > J_c$, a critical value, oxygen ions were migrated and local oxygen densities were changed between two voltage probes. This leads to electrical resistance switching (RS). After RS at the low resistance state oxygen ions were trapped at the surface defects or at the vacancy sites for finite time .The release from the trap follows a stochastic signature. From an investigation of the temperature dependence of the critical current J_c we showed that the oxygen ions are stabilized against migration (by a current/Field) by a potential barrier $E_a \sim 0.12 - 0.27$ eV. This experiment showed that it is possible to migrate oxygen ions rather quickly with a current induced "forced" diffusion.

5.1 Introduction

Due to the application of any external stimulus when the resistance of a system changes between two metastable states, it is called resistive-switching (RS) phenomena. After discovery several research work had been performed to understand the physical mechanism behind this switching [1,2]. In the oxide samples oxygen diffusion plays an important role in RS mechanism [2]. In perovskite oxides oxygen diffusion in non uniform oxygenated regions follows the RS process which is often described as insulator to metal (IM) phase transition [3].

By the change of oxygen stoichiometry one can change the properties of correlated oxides like manganite and in previous work generally the oxygen stoichiometry has been tuned by heat treatment (temperature above 500 ^{0}C in film or bulk sample) with maintaining the oxygen partial pressure [4-8]. In this process the phase of the system has been changed irreversibly.

The main motivation of this work is to show whether one can migrate oxygen ions over a finite length scale (~ tens of microns) by applying a current and thus having a "forced" oxygen migration from a localized region that has high oxygen density. The experiment was carried out on submicron strip of an oxide $La_{0.85}Sr_{0.15}MnO_3$ (LSMO:0.15). Low hole doped LSMO:0.15 lies in a region of phase diagram where oxygenation leads to enhancement of hole density and large reduction in its resistance. The drop in resistance of the submicron strip on oxygen migration is like a resistance switching (RS) between two voltage probe. We use the current induced RS as a tool to probe the migration (and also trapping of oxygen). In this experiment in the oxide strip, by electrochemical oxidation process, a localized source of oxygen rich region was created, using lithographic process to define the region for electrochemical oxidation. We observe that the for a DC-current of density $J > J_C$, a critical value, oxygen ions were migrated and local oxygen densities were changed between two voltage probes leading to RS.

The oxidation was localized using lithographically defined region. This oxidation process was used in past works on $La_{0.2}Sr_{0.8}CoO_3$ [9], $La_4Ni_3O_{10}$ [10] and La_2CuO_4 [11] systems. Oxygen ions were migrated out of the localized region by application of high density DC-current flow [2].

5.2 Experimental

5.2.1. $La_{0.85}Sr_{0.15}MnO_3$ nanowire preparation

By Pulsed Laser Deposition (PLD) technique LSMO:0.15 micro strips (50 μm× 4 mm) were prepared on (100) oriented LaO substrates. The chamber oxygen pressure was maintained during the deposition and cooling process at 1 ×10^{-1} mbar. The fluence was used 1.8 J/cm^2. The optimized shot frequency was 3 Hz and the target frequency was 20 rpm. The optimized substrate temperature was 700 ^{0}C and the substrate was pre-annealed for 1 hr before deposition and after deposition it was post annealed for 5 hrs. To avoid any abrupt crack developing in the sample which may act as a fast diffusive path for oxygen ions the deposited film was cooled very slowly (0.5^{0}C/min). The thickness of the film was measured from the cross-sectional Field emission gun scanning electron microscope (FEG-SEM) images and it was ≈ 700 nm (images are not shown here). The composition was confirmed from Energy Dispersive X-Ray (EDX) analysis of the cross section or along the depth of the film. It showed the La:Sr ratio 5.66(± 0.19):1 which confirms the metal stoichiometry of $La_{0.85}Sr_{0.15}MnO_3$.

TABLE 5.I. Dimension of the samples studied (thickness ≈ 740 nm).

Sample-ID	Length (µm)	Width (nm)
A_1	20	340
B_1	30	740

The surface morphology of the film was studied by atomic force microscope (AFM) images where we found the average grain size 29 nm(± 6 nm). Two sub-micron strip samples were prepared from the films using Focused Ion Beam (FIB).The structured sub-microstrip (hence forth referred to as nanowire) is shown in FIG. 5.1 has been extracted from the micro strips of the films. Two large regions (called source and sink) were separated by the nanowire (marked as NW in the diagram).Combination of Photo-lithography, Electron beam lithography and Pt-deposition by FIB was used to make electrical contact pads. The dimension of the samples (nanowires) is given in TABLE 5.I. The as prepared samples are indicated by A and B. After oxidation they are marked as A_1 and B_1.

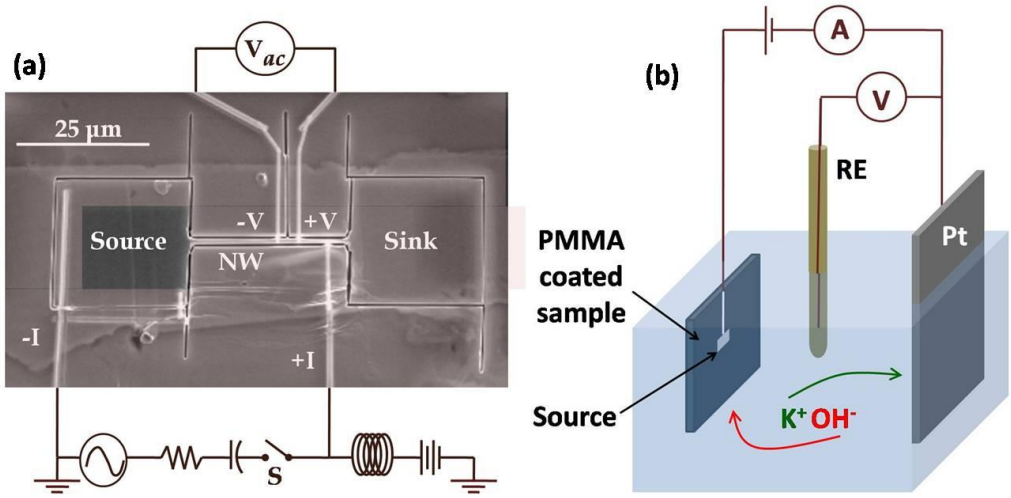

FIG. 5.1. Schematic diagram of the (a) oxidation process and (b) circuit structure of the sample. The nanowire (NW) between voltage leads are mentioned as ΔL.

5.2.2. Oxidation of sample

Except the source area the whole device was covered with PMMA resist to avoid unnecessary oxidation of the other regions. Electrochemical oxidation technique was used to introduce oxygen into the source area. In the electrochemical set-up a Pt-sheet and Hg/HgO were used as counter and reference electrodes respectively. The sample was used as working electrode. Here we used 1 (M) KOH solution as electrolyte (see FIG.5.1.(a)).As described before the total amount of oxygen transferred was estimated using Farady's Law by integrating the current in the electrochemical cell. The amount of deposited oxygen concentration in the source of the samples was 5.3×10^{26} m^{-3} (here we consider that the oxygen ions were

uniformly distributed over the sample). This indeed is a source of error. However, we show that over days there is diffusion of oxygen ions that remove inhomogeneous distribution and this leads to somewhat homogeneous. The extent of diffusion at room temperature is in scale of μm over days (measurement shown below). This being larger than sample dimension the assumption of homogeneity is reasonable.

5.2.3. Electrical circuits

After stabilization of the oxygen in the source region over days we did electrical transport measurements. Here we have used a circuit where AC and DC currents were simultaneously used (FIG.5.1.(a)). AC-current was used to measure the resistance and DC-current was utilized to migrate the oxygen ions through the nanowire. Standard four probe measurement technique was used for the resistance measurement. AC current (I_{ac}) was generated by the Lock-in amplifier (LIA). To make a constant current flow the ACcurrent was passed through a high resistance (R_H) which was connected in series with the sample. To know the value of AC-current we used a Digital multimeter (DMM) across R_H. The voltage across the sample was measured by the same LIA. DC-current (I_{dc}) was supplied and regulated by a Source Meter. I_{ac} and I_{dc} were mixed and was applied to the nanowire sample through $+I$ lead. $I_{ac} << I_{dc}$, the AC does not affect the migration process. During the measurement to make constant temperature the complete PMMA coated device was immersed into a de-ionized water bath. Using a controlled heater the bath temperature was maintained at a particular temperature.

5.3 Results and discussions

5.3.1. Lateral diffusion study

The lateral migration that would occur naturally from the oxygen rich region at room temperature (which we call thermal migration as opposed to the current induced migration).We made this study of lateral diffusion. For this we prepared another sample which is marked as C. This sample was mainly used to define the lateral diffusion length (l_d).This sample was also prepared from a PLD grown film of $La_{0.85}Sr_{0.15}MnO_3$ prepared on LaO substrate. For making electrical contact pads a rectangular Ag micro strip on the film was made by thermal evaporation. After making electrical contacts the sample was covered by SU8 photo-resist. By photolithography SU8 was removed only from the two circular regions near the Ag pad (FIG.5.2.). Then at room temperature the sample was oxidized by electrochemical method. This makes a region of the film that has well localized oxidation and is oxygen rich. After a long time (20 days) SU8 resist from the sample was removed and oxygen mapping on the surface of the film was done using spot EDX.

The extra oxygen concentration was defined by $\Delta C(x) \equiv C(x) - C_0$, where $C(x)$ is the oxygen concentration at given location $x$after oxidation and C_0 is for the as prepared sample. The colour contour plot of the relative change in oxygen concentration (expressed in %) and defined as $\Delta C(x)/C_0$ is plotted in FIG.5.3. The oxygen concentration is maximum at the middle of the circles and gradually decreases towards outside the circles. The diffused

oxygen concentration from these two circular regions can be described by the equation given below.

$$\frac{\Delta C(x)}{C_0} = M\left[\exp\left\{-\frac{(x-x_1)^2}{2l_d^2}\right\} + \exp\left\{-\frac{(x-x_2)^2}{2l_d^2}\right\}\right] \qquad (5.1)$$

, where M is a constant, x_1 and x_2 are the two positions (centre of the left and right circular region) where oxygen concentration becomes maximum and l_d is the lateral diffusion length of this material. By the fitting of equation (5.1) with the experimental results (FIG.5.4.) we find an average value of l_d = 3.38 μm.

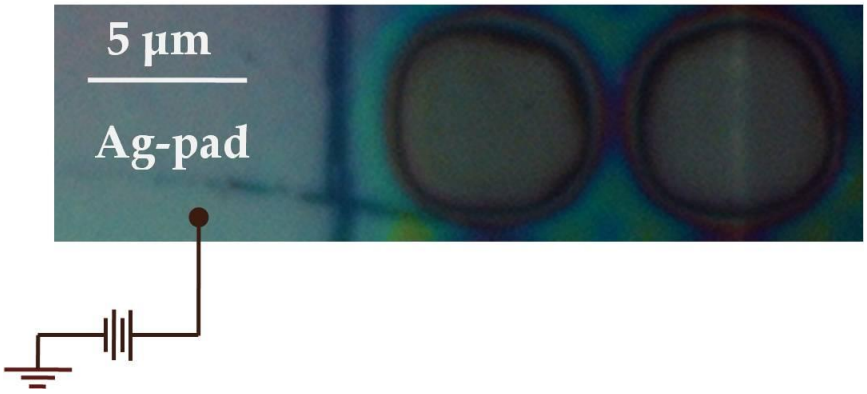

FIG. 5.2. Optical image of the SU8 covered sample *C*. Schematic electrical connection for oxidation is shown.

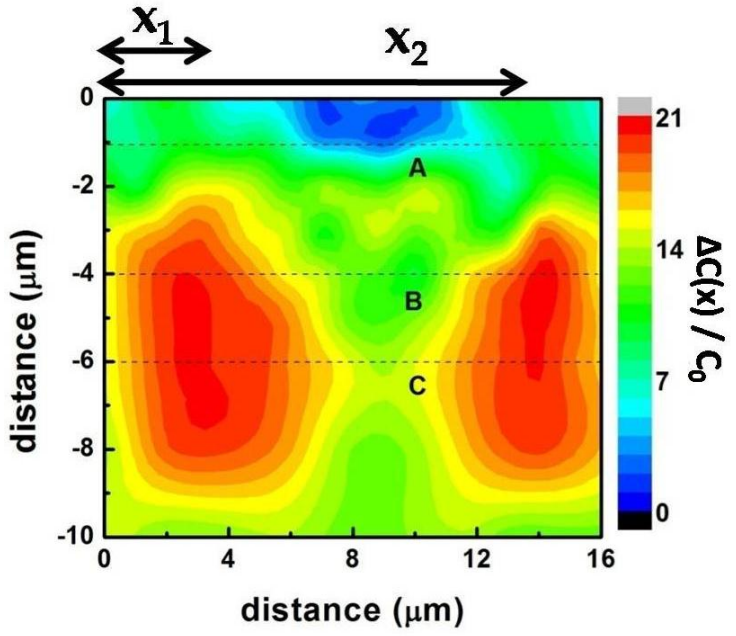

FIG. 5.3. Colour contour plot of oxygen concentration $\Delta C(x)/C_0$ from EDX result.

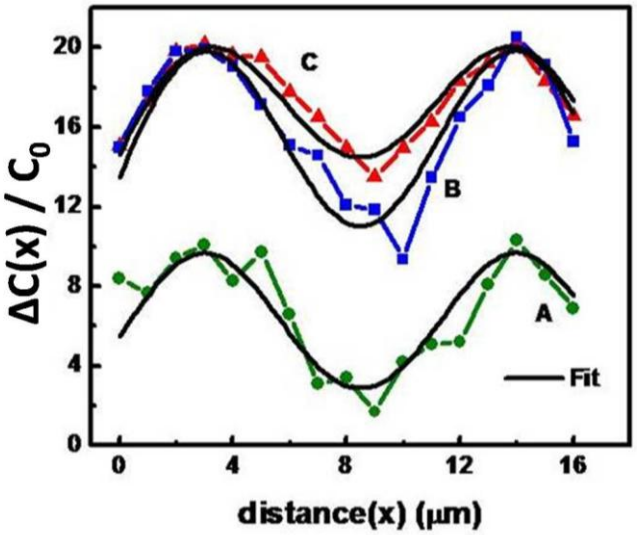

FIG. 5.4. Fit of equation (5.1) to $\Delta C(x)/C_0$ vs. distance (x) through the line A, B and C indicated in FIG.5.3.

5.3.2. DC Current-Voltage measurement

At room temperature (~ 300 K) the DC-current (I) dependence voltage (V_S) across the ΔL position (nanowire between voltage leads) of the oxidized samples (A_1 and B_1) are shown in FIG.5.5. Here DC-measurements have been done. At a critical current (I_C) the sample resistance (R) sharply falls to a lower value and it was observed clearly in the $V_S - I$curve. For $I > I_C$the DC-current is responsible for high to low resistance state switching (RS) process. Though the polarity of the current changes, the low resistance state still persist up to 50 μA current. The value of critical current density (J_C) to achieve the metallic phase for the samples A_1 and B_1 is 4.62×10^7 A/m^2 and 4.03×10^7 A/m^2 respectively. J_CValues are of the same order of the critical oxygen migration current density ($10^7 - 10^8$A/m^2) of this kind of materials [12].The experimental result shows the change occurs when the applied voltage gradient is form. This would migrate the negatively charged O_2 in the direction from the source to the sink through the test region.

The result also shows that the change is irreversible. Once the ions are migrated they get stay in the probe region and presumably trapped in site so that reverse current cannot reverse the resistance switching.

The migration of ions and the existence of the critical current for migration would suggest stabilization of the oxygen in the source region by a potential well. To explore this we measured the current induced switching as a function of current. The data are shown in FIG.5. 6. (a),(b)).

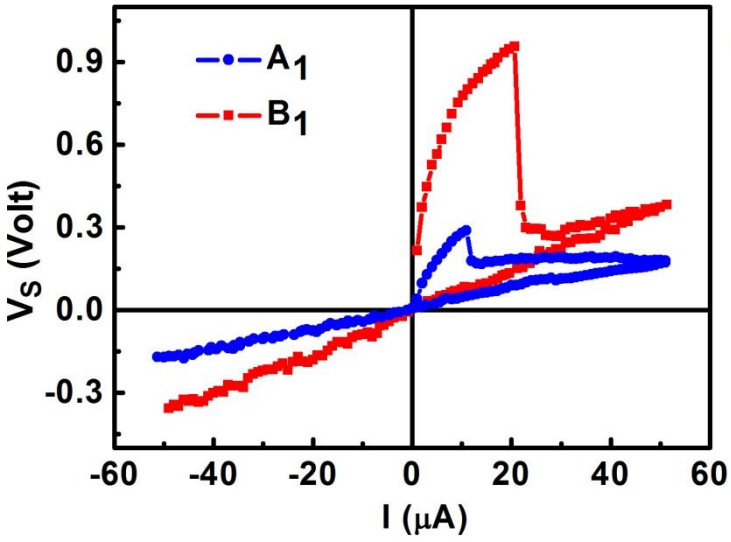

FIG. 5.5. DC-current vs. sample voltage V_S (voltage across ΔL) at 300 K for sample A_1 and B_1.

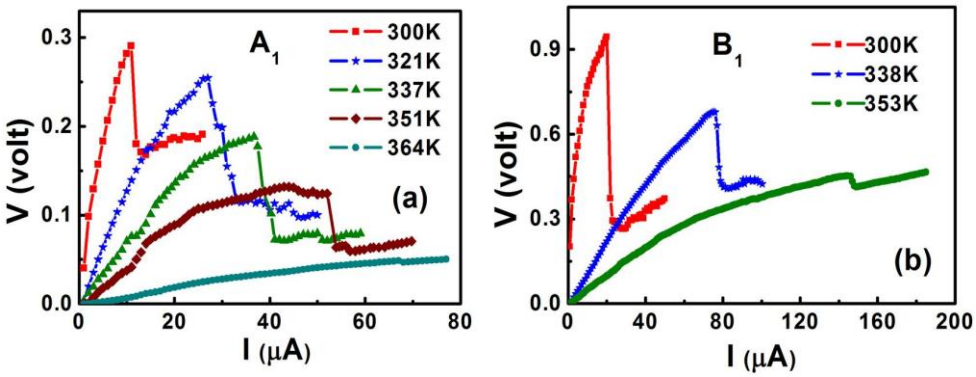

FIG. 5.6. Current (I) dependent voltage (V_S) profile for different temperatures (T) of (a) sample A_1 and (b) sample B_1.

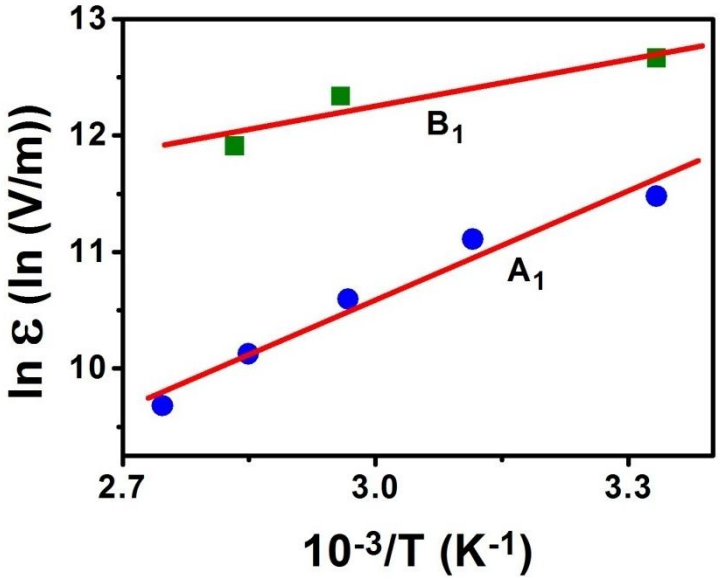

FIG. 5.7. Arrhenius T dependency of ε.

It is seen that V_S decreases with the increment of temperature. Qualitatively this would imply that the potential barrier to migration is reduced on heating leading to a lower required V_S. The Arrhenius relation of the electric field (ε) between voltage probes becomes, $\varepsilon = \varepsilon(\propto) exp(-E_a/(k_B\, T)$, where $\varepsilon = \varepsilon(\propto)$ at $T \to \infty$ and E_a is the activation energy of the process. The value of E_a calculated from FIG. 5.7, for the samples A_1 and B_1 is 266.8 meV and 117.8 meV respectively. The activation energy for migration will consist of two parts one is migration through sample bulk and other through surface. Presence of large number of surface states can act as trap sites hindering migration and thus enhancing effective activation energy. Sample A_1 has larger surface/volume ratio than B_1 and therefore it has larger number of defects.

5.3.3. Time dependent resistance change

At room temperature on the oxygenated nanowire samples (A_1 and B_1) we applied a DC-current pulse ($I_P > I_C$) of value 30 μA for 2 sec. The resistance of the samples decreased sharply to a lower value (FIG.5.8. (b),(c)). The resistance of the sample was measured by AC-current flow and simultaneously DC-current was used for resistance switching only. As an example for A_1 and B_1 the resistance decreased from ~ 16 kΩ to 4 kΩ (~1/4 times) and from ~56 kΩ to 5 kΩ (~1/11 times) respectively. But this low resistive state was unstable when the pulse current is removed. After a time, which is referred as the wait time (t_W), the system reversed back to the high resistive state again. The wait time as well as the resistance states between the switch have an element of stochastic process as we show later on. However, the aspect that there is resistance state switching when the pulse is ON and then switch back when it is OFF is repetitive.

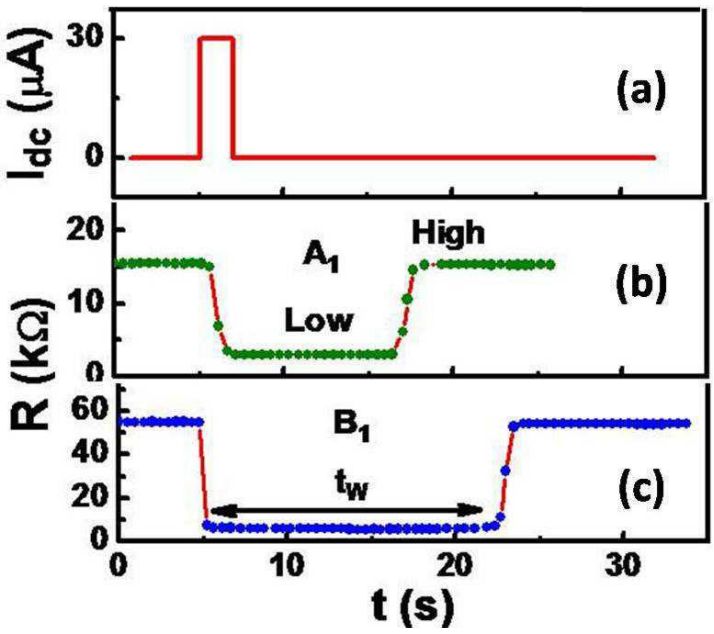

FIG. 5.8. (a) Applied pulsed DC-current I_P= 30μA. Time (t) dependent resistance (R) of sample (b) A_1 and (c) sample B_1. Wait time (t_W), High and Low resistive states are mentioned.

5.3.4. Time constants of resistance fall and recovery

After applying I_P the resistance of the samples was decreased sharply and after t_W the resistance again returned back to the high resistance state. In this section we discuss the stochastic nature of the process as quantified through the distribution of the fall and recovery time. We find that the resistance fall and rise follow time dependences that can be expressed by single exponentials. Time dependent resistance fall can be described by the relation $\Delta R = R_0 \exp(-t/\tau_F)$ and time dependent resistance rise can be described by the relation, $\Delta R = R_0\{1 - \exp(-t/\tau_R)\}$. Here we consider only the resistance change ΔR. The times τ_F and τ_R are the relaxation times for resistance fall and rise processes respectively. The value of τ was calculated from the fitting of the above relations with the experimental data (see FIG.5.9).

We find that there are distributions in the τ's when the pulse is applied repetitively. The τ's follows Gaussian distributions. In FIG.5.10we show the distribution as well as the Gaussian fit. The mean values of the distributions along with the width of the distribution are tabulated in TABLE 5.II.

TABLE 5.II. Relaxation time τ for the fall and rise processes.

Sample-ID	τ_F (s)	Width (s)	τ_R(s)	Width(s)	τ_R/τ_F
A_1	0.12	0.073	2.40	1.46	20.0
B_1	0.05	0.019	0.38	0.07	7.6

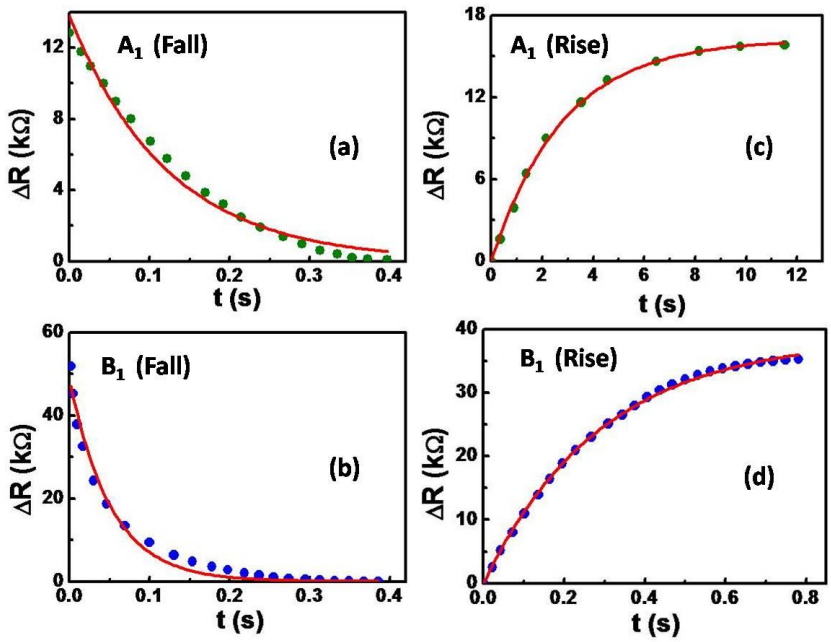

FIG. 5.9. Resistance change (ΔR) vs. time (t) for resistance fall of (a) A_1, (b) B_1. Similar graph is plotted for resistance rise of the samples A_1 and B_1 in (c), (d).

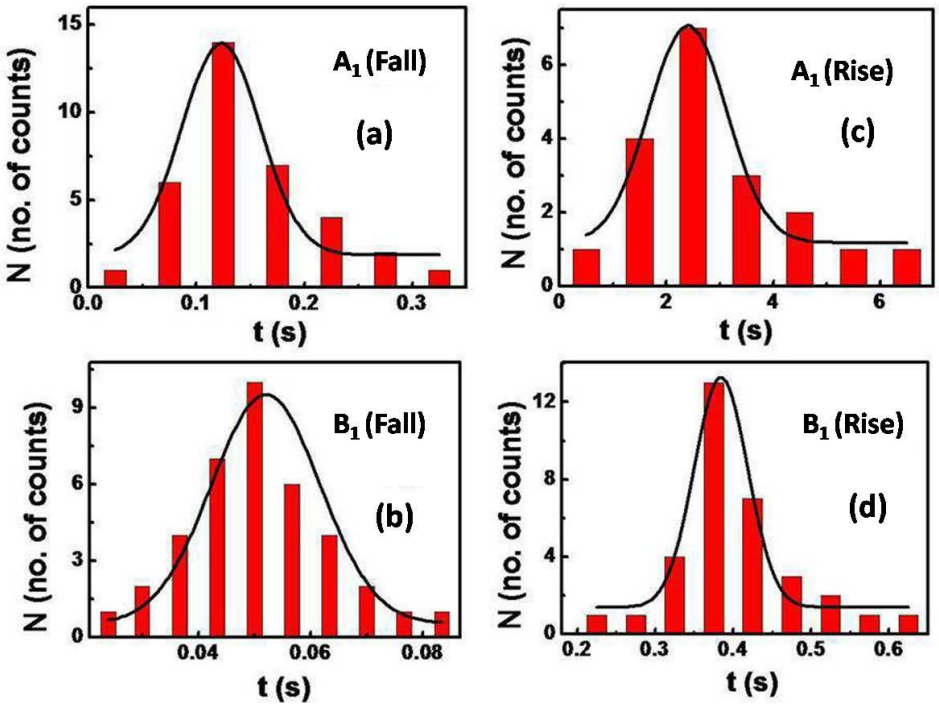

FIG. 5.10. Gaussian distribution fit of τ of sample for resistance fall of (a) A_1, (b) B_1 and Gaussian distribution fit of τ of sample for resistance rise (c) A_1, (d) B_1.

The stochastic nature of the process is clear that the rise and fall don't occur with same time constants when the process is repeated. In both samples sample A_1 and B_1, we find that $\tau_R \gg \tau_F$.When the resistance falls there is diffusion (normal) along with driving by the field while in case of the resistance rise process there is no driving field and the normal diffusion drives the process. Thus the observed asymmetry in the time constants is qualitatively understandable. Interesting however, is the observation that τ_R / τ_F for the narrower wire A_1 is much larger than that seen in the wiser wire B_1. This is due to that fact that in the sample A_1, the τ_R is about an order larger than that seen in sample B_1. One way it can be explained that the oxygen diffusion is constrained in the narrow wire leading to a large rise time.

5.3.5. Distribution in resistance jumps

The low resistance state is unstable and after t_W the resistance jumps back to the high value. When the voltage bias pulse is repeatedly applied the resistance state does switch but the values of the resistance R at the Low resistance state (LRS) (we refer as R_L) and that at the high resistance state (HRS) (referred as R_H) do vary. This is shown in FIG.5.11.

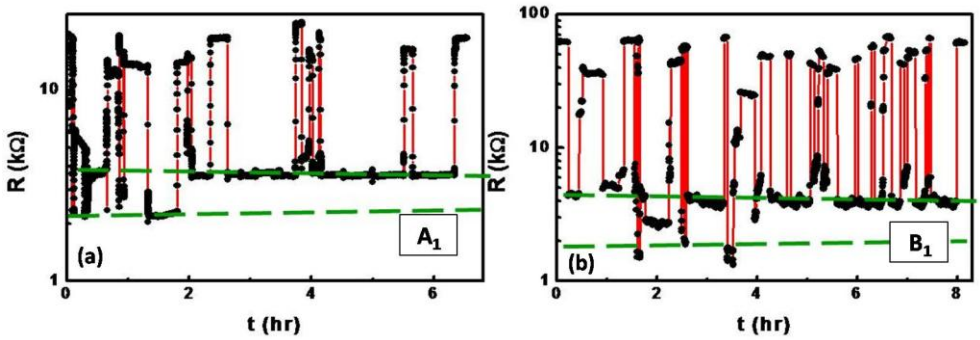

FIG. 5.11. The repetitive measurement of resistance vs. time for sample (a) A_1 and (b) B_1. Each time resistance fall occurs due to the application of current pulse I_P. Different resistive states (Low) are indicated by broken lines of green colour.

In the FIG.5.11 it can be seen that the R_L mostly has two values in both wires but the lower value of R_L is most probable. Transition to LRS occurs when the applied pulse moves oxygen in between the voltage probe sites. When the oxygen ions move in it is supposed to do a "hole" doping leading to drop in the resistance. However, it may happen that there are two different sites (bulk and the surface) where the ion gets trapped in. These two sites would have different effectiveness in hole doping that will contribute to the resistance changes. We will see below that this is reflected in the distribution in wait time t_W. The R_H appears to have probabilities of more value but they are distinct. The rise in the resistance after the pulse is turned off will of course depend on whether the ions are fully moved out of the voltage probe region when the pulse is removed. This being a field free process it can happen in either direction. For complete removal the value of R_H will be highest. It can also happen that some fraction of the released ions is re-trapped in the region between the probes in that case the recovery to full value of R_H will not occur and the value of R_H that we will get will be less. The differing values of R_H thus can be justified.

5.3.6. Wait time t_W

The resistance switching that occurs after a pulse shows that the switched LRS is a metastable state and after a wait time (t_W) the LRS makes a transition to HRS. Since there is a finite t_W it shows that there is trapping at a preferred site when the current pulse migrates the ions to the prove region. The metastability arises from the trapping process. The detrapping of the ions leads to transition. The discussion on the values of R_L and R_H showed that there is an element of stochasticity and this is expected to lead to a distribution of wait time. In FIG.5.11 we show the experimental results that show the distribution of t_W.

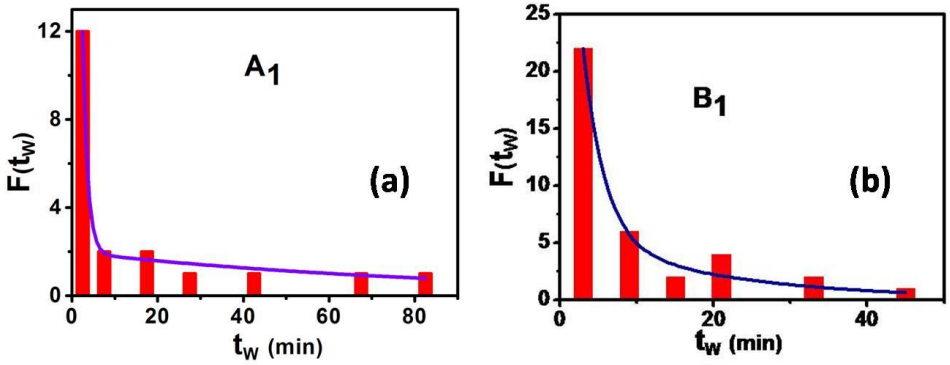

FIG. 5.12. Wait time (t_W) distribution F(t_W) for the sample (a) A_1 and (b) B_1.

Since there present two different kind of trapping sites, one is at the defect sites at the surface and another one is the vacancy sites at the volume, the distribution of t_W can be expressed by the addition of two different exponential functions.

$$F(w) = C_S e^{-t_w \sigma_S} + C_v e^{-t_w \sigma_v} \quad (5.2)$$

, where C_S, C_v and σ_S, σ_v are the constants and decay constant for the surface and volume sites respectively. The value of the constants were determined from the fitting of the experimental results (see FIG.5.12) and are tabulated at TABLE 5.III. Again [13], $t_W(i) = \exp(E_i/k_B T)/\nu$, where E_i is the trapping energy of a state 'i' and ν is the attempt frequency. The surface energy is always smaller than the volume energy and therefore from this expression it is clear that t_W of surface term is smaller than the volume term. In equation (5.2) the term where σ is greater is the surface term. Again the ratio of the constant factors C_S/C_v is greater in A_1 (~ 45) than B_1 (~ 8.3). This establishes the fact that surface trapping is more favourable in the smaller diameter nanowire sample. This corroborates our earlier finding where the activation energy for migration was found to be larger for the narrower wire.

TABLE 5.III. Constants of distribution.

Sample-ID	C_v	C_S	σ_v	σ_S	C_S/C_v
A_1	2.0	90	0.01	0.90	45.0
B_1	6.0	50	0.05	0.36	8.33

The trapping energy can be expressed as [14], $E_i = k_B T ln(P t_W(i)/\tau_0)$, where τ_0 is the life time of free carriers or it can say that the time to capture carrier by all the trapping levels [15] and P is the release probability.

$$\tau_0 = \left[\int_0^\infty c(\epsilon)\varphi(\epsilon)\, d\epsilon\right]^{-1} \quad (5.3)$$

, where $c(\epsilon)$is the transition probability of carriers between trapping and mobile states. The density of localized level of energy between $\epsilon$and ϵ+dϵ is $\varphi(\epsilon)d\epsilon$. The trapping process follows exponential decay function (resistance

fall relation) $exp(-t/\tau_F)$ and therefore 100 % trapping only possible for $t \rightarrow \propto$. Here to find out the value of τ_0 we have taken 99.9% trapping and therefore $\tau_0 = 6.9\tau_F$. Using this relation τ_0 can be found out to be 0.85 s and 0.36 s for sample A_1 and B_1 respectively. Therefore from the distribution of trapping time the range of trapping energy states ΔE_i can be calculated as $133-223$ meV and $132-202$ meV for sample A_1 and B_1.The range of trapping energy states for both wires are similar but it is somewhat larger for the narrower wire.

5.4 Conclusions

In this work we studied the current driven oxygen migration in highly inhomogeneous oxygenated $La_{0.85}Sr_{0.15}MnO_3$ nanowire. The inhomogeneous oxidation is possible due to the application of room temperature electrochemical oxidation process. By the application of electric field the excess oxygen density at different regions of the nanowire can be tuned. The process is electrically irreversible. By thermal energy after a wait time t_W oxygen ions are relaxed back again to their previous positions. This relaxed back process explore the fact that the probability to go the electrically migrated oxygen ions at the surface defects of the nanowire increases with the decrement of wire diameter. This work in future can be used in resistance switching applications.

References:

1. T. W. Hickmott, *J. Appl. Phys*. **33**, 2669 (1962).
2. Jae Sung Lee, Shinbuhm Lee and Tae Won Noh, *Appl. Phys. Rev*. **2**, 031303 (2015).
3. A. Ignatiev, N. J. Wu, X. Chen, S. Q. Liu, C. Papagianni and J. Strozier, *Phys. Status Solidi B.* **243**, 2089 (2006).
4. L. Malavasi and G. Flor, *J.Phys.Chem B.* **107(50)**, 13880(2003).
5. H. Zhang, X. Yao and X. H. Zeng, *Phys. Stat. Sal.(a)201*.**10**, 2305 (2004).
6. K. Yamamoto, B. M. Lairson, J. C. Bravman and T. H. Geballe, *J. App. Phys*. **69**, 7189 (1991).
7. S. Kittelberger, O. M. Stoll and R. P. Huebener, *Supercond. Sci. Technol*. **11**,744 (1998).
8. K. N. Tu, N. C. Yeh, S. I. Park and C. C. Tsuei, *Phys. Rev. B.* **39**, 1 (1989).
9. V. Pralong, V. Caignaert, S. Hebert, C. Marinescu, B. Raveau and A. Maignan, *Solid State Ionics*. **177**, 815 (2006).
10. M. D. Carvalho, A. Wattiaux, J. M. Bassat, J. C. Grenier, M. Pouchard, M. I. da Silva Pereira and F. M. A. Costa, *J. Solid State Electrochem*. **7** , 700 (2003).
11. H. H. Feng, Z. G. Li, P. H. Hor, S. Bhavaraju, J. F. DiCarlo and A. J. Jacobson, *Phys. Rev. B(Rapid com.)*. **51**, 22 (1995).
12. Arindam Ghosh and A. K. Raychaudhuri, *Phys. Rev. B.* **64**, 104304 (2001).
13. Y. Yang, P. Gao, S. Gaba, T. Chang, X. Pan and W. Lu, *Nat. Comm*. **3**, 732 (2012).
14. V. I. Arkhipov and A. I. Rudenko, *Philosophical Magazine B*. **45**, 189 (1982).
15. A. I. Rudenko and V. I. Arkhipov, *Philosophical Magazine B*. **45**, 177 (1982).

Chapter 6

Stability of charge and orbital order in nanocrystals of half-doped manganite $Y_{0.5}Ca_{0.5}MnO_3$

In this work, we have done a detailed study ofthe structure, magnetic, and electrical transport properties in nanocrystallites of hole-doped manganite$Y_{0.5}Ca_{0.5}MnO_3$, with the aim to study the effect of size reduction on the stability of the charge-orbital order and the antiferromagnetic spin order that are seen in the bulk samples of the half-doped manganite. The investigations have been done in the general context of investigating how size reduction affects competing interactions in complex oxides and thus, changes their ground state. The bulk sample of the material (average crystallite size ~1μm), with the smallest radius of the cation in A-site (Y), shows a robust charge and orbital ordered insulating state below the transition temperature near 290 K and an antiferromagnetic spin order at 110 K. The experiments carried out on well characterized nanocrystalline samples, with average crystallite sizes down to 75 nm, establish that the size reduction changes the structural parameters, and the charge and orbital ordering are suppressed. However, the antiferromagnetic spin order (as revealed by neutron diffraction experiments carried out down to2 K) persists in the nanocrystallites and co-exists with ferromagnetic order below 110 K. The nanocrystalline samples have significant lower resistivities (by few orders) compared to those of the bulk samples in the temperature range 10–300 K. This corroborates the formation of the ferromagnetic moments in the nanocrystallites.

6.1 Introduction

Control of the ground state of complex functional perovskite oxides by size reduction to the nanometric regime is an active area of research. This allows engineering of new properties in nanomaterials, keeping the chemical constituents and the stoichiometry unchanged. In this thesis, we investigate the effect of size reduction in a complex perovskite oxide, which in bulk form shows a robust charge and orbital ordered ground state. Charge and orbital ordering (COO) in

half-doped perovskite oxide manganites, which are also accompanied by antiferromagnetic (AFM) spin ordering, form a fascinating class of physical phenomena [1]. The COO leads to an insulating ground state. The half-doped manganites, in which these phenomena have been most investigated, belong to the system with general formula$A_{0.5}Ca_{0.5}MnO_3$, with A site being occupied by trivalent elements like La, Pr, Nd, Sm, Y, etc. It has been recognized that the orbital ordering is rather sensitive to the size of cations occupying the A-site [2]. As the radius of the A-site cation (r_A) decreases, the tendency for the formation of COO gets enhanced, leading to an increase in the COO temperature T_{CO}. The evolution of the COO ordering temperature T_{CO}, the AFM transition temperature T_N, and the ferromagnetic transition temperature T_C, that may precede T_{CO}, is shown in FIG.6.1as a function of the average ionic radius size r_A of the A-site ions. The graph shows very clearly the enhancement of the COO transition as r_A decreases. The cations A shown in FIG.6.1in order of decreasing r_A are La [3], Pr [4], Nd [5], Sm [2], and Y [6-7]. The data in FIG.6.1 are collected from references mentioned. $La_{0.5}Ca_{0.5}MnO_3$, which has the largest r_A in the series shown, shows antiferromagnetic transition that, precedes the COO transition. For other members of the series, there is no ferromagnetic state. The stability of the COO state is often measured by its sensitivity to the applied magnetic field. Generally, in $La_{0.5}Ca_{0.5}MnO_3$, a magnetic field of a few Tesla can destabilize the COO-AFM insulating state to a ferromagnetic metallic state. For sufficiently small r_A, as in $Y_{0.5}Ca_{0.5}MnO_3$, the ordering becomes so robust that it cannot be destabilized even after applying a high magnetic field of value ≈ 20 T or more. It is believed that in this case the bandwidth is very narrow so that the electrons get localized, leading to formation of a rugged insulating state at a relatively high temperature.

The orbital ordering phenomena that occur in the half-doped systems have an important synergy with structure and it is often decided by the evolution of the orthorhombic distortion in the structure with temperature. The size reduction can alter the structural parameters and thus can alter the evolution of the orthorhombic distortions, which, in turn, can affect the development of the orbital order in the systems with reduced sizes. Generally, two competing effects decide the structure that leads to orthorhombic distortion. Smaller cation radius (i.e., smaller r_A) leads to cooperative buckling of the MnO_6 octahedra which leads to orthorhombic distortion (referred as O-type) as well as reduction of the Mn–O–Mn angle that controls the electron hopping and the bandwidth. In addition, the Jahn–Teller distortion around Mn^{3+}ions can also lead to cooperative orbital ordering leading to orthorhombic distortion of somewhat different type (referred as O'-type) [6,8].For the system under consideration in this paper, $Y_{0.5}Ca_{0.5}MnO_3$, the Y ion has the smallest radius. The COO transition in bulk samples of $Y_{0.5}Ca_{0.5}MnO_3$ (i.e., samples with crystallite size ≥ 1μm) occurs in the vicinity of 290 K, which is higher than that seen in most half-doped manganites. For this particular system, the cooperative buckling of the MnO_6 octahedra plays an important role in stabilizing the O-type structure. The evolution of the structure and orthorhombic distortion in $Y_{0.5}Ca_{0.5}MnO_3$ and also the formation of the COO order have been investigated before which highlight the issues discussed above [8-10].

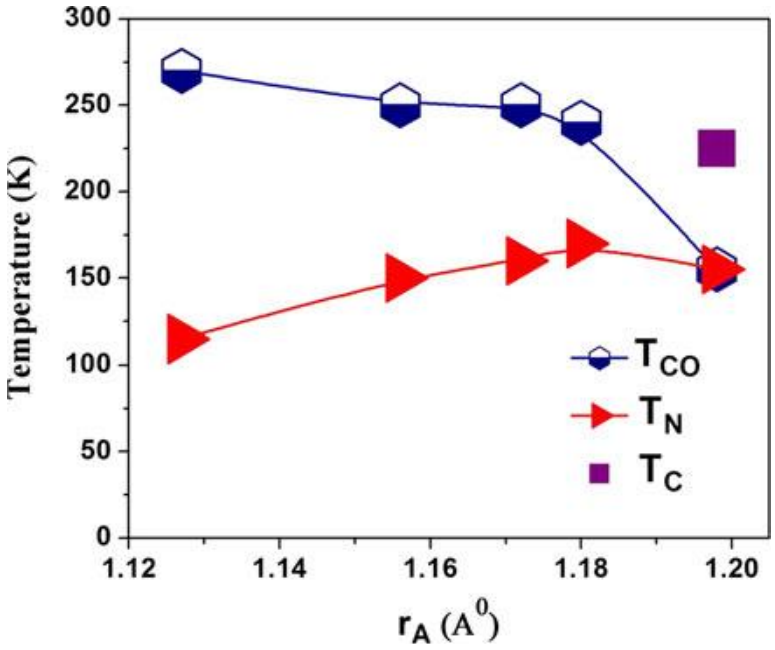

FIG. 6.1. The variation of charge ordered transition temperature, antiferromagnetic transition temperature, and ferromagnetic transition temperature with respect to average cation radius for bulk half-doped manganites $A_{0.5}Ca_{0.5}MnO_3$ are shown. The A in order of decreasing ionic radii are La, Pr, Nd, Sm, and Y. References are given in text.

In recent years, the field of COO in half-doped manganites added to it yet another exciting component, where it was observed that the ground-state properties of half-doped perovskite oxide manganites can be tuned by reduction of the size of crystallites. It had been observed in a number of manganites that the charge and orbital ordered ground state (along with the AFM spin order) can be destabilized by reducing the size of the crystallites to the vicinity of 100 nm or below [11-16]. There are reports of changes in lattice structure on size reduction [12-13]. Interestingly, this destabilization enhances the ferromagnetic interactions, leading to creation of strong ferromagnetic moments that can lead to long-range ferromagnetic ordering. Sometimes, depending on the system, this can lead to phase separation and co-existence of competing phases. So far, the effect of size reduction on the COO transition in half-doped manganites has been observed mainly on $A_{0.5}Ca_{0.5}MnO_3$ systems with A = La, Pr, Nd, and Sm [12-15]. These ions have the average A-site cation radius $r_A \geq 1.15$ (see FIG.6.1). In this paper, we address an important question whether the robust COO seen in a material like $Y_{0.5}Ca_{0.5}MnO_3$, which has the smallest r_A, can be destabilized by size reduction. We have investigated the stability of COO transition in well-characterized nanocrystalline samples of $Y_{0.5}Ca_{0.5}MnO_3$ with sizes down to 75 nm. The investigation was done using temperature-dependent X-ray studies, magnetic measurements that include magnetization measurements and neutron diffraction and electrical measurements. While the X-ray studies were done at $T \geq 300$ K to look for any changes in the important O–O' transition that might occur on size reduction, the electrical and magnetic measurements (including neutron diffraction) were carried out below 300 K and down to 5 K. We note that this is the first detailed investigation on the physical properties of $Y_{0.5}Ca_{0.5}MnO_3$nanocrystallites with size in sub-100 nm domain.

6.2Experimental

6.2.1 Sample synthesis

We have adopted chemical solution deposition (CSD) method to prepare $Y_{0.5}Ca_{0.5}MnO_3$ samples. The major advantage of this method is that the phase formation can occur at relatively lower temperatures compared to that in conventional solid-state technique, which is useful to control the smaller grain size particles [17]. High-purity yttrium acetate hydrate $[(CH_3CO_2)_3Y.xH_2O]$, calcium acetate hydrate $[Ca(C_2H_3O_2)_2.\ H_2O]$ and manganese acetate tetra hydrate $[(C_2H_3O_2)_2Mn.4H_2O]$ are mixed in stoichiometric ratio with de-ionized water and acetic acid mixture and appropriate amount of ethylene glycol $[C_2H_4(OH)_2]$ (0.3 in volume ratio). The polymer used in this process is ethylene glycol, which forms a closed network of cations from the precursor solution and assists the reaction for formation of phase. We have taken metal acetates of Y, Ca, and Mn in the stoichiometric ratio of 0.5:0.5:1. Metal acetates are dissolved in water:acetic acid:ethylene glycol in volume ratio of 1:1:0.3. The solution was heated and stirred until gel was formed. The gel was then dried overnight at temperature ~150 ^{0}C followed by pyrolysis done at temperatures 350 ^{0}C and 450 ^{0}C and finally, it was sintered at temperature 830 ^{0}C to obtain the desired phase and particle size. In the present Y-based system, the phase formation occurs at somewhat higher temperatures (compared to the La- or Pr-based systems that we investigated before [12-13], which constrains the size of the crystallites to be above 75 nm.

For comparison and to have reference data for the bulk sample, we have also made a ~ 1 μm sample by heating the pellets of nanocrystallites to higher temperature (1350 ^{0}C) for 24 h. The heat treatment at higher temperature allows grain growth to larger size. We found that these crystallites, made by the CSD method, have very similar structure and physical properties compared to the samples made by standard ceramic route. The CSD method allows us to make crystallites of varying size using the same starting batch.

6.2.2 Characterization

The samples were first characterized by powder X-ray diffraction (XRD) at 300 K. The high-temperature X-ray diffraction experiment was carried out using a PAN analytical expert pro system in the temperature range 300–1100 K using CuKa line. The structure was analyzed using Rietveld refinement with FullProf software (fullprof). The particle sizes for the samples used were determined by scanning electron microscope. The average particle size with standard deviation was obtained from the distribution. The bulk sample has average particle size 1.05 ± .05 μm, while for the nano sample average particle size is around 75 ± 10 nm.

The absolute chemical compositions were estimated by inductively coupled plasma atomic emission spectroscopy (ICP-AES). We have also used iodometric titration to determine the oxygen stoichiometry for both the samples. Spatial chemical homogeneities of the samples were checked by exploring the spatially resolved relative compositions with energy-dispersive X-ray (EDAX) analysis. The combination of these tests establishes the chemical fidelity of the samples used in this investigation.

6.2.3 Physical measurements

For magnetization and electrical measurements we used pellets made from the crystallites. The magnetization measurements were done using a SQUID

magnetometer down to 5 K. We have done electrical measurements using a standard four-probe DC set-up coupled to a closed cycle He system.

6.2.4 Neutron diffraction

To supplement the magnetic data that were taken using SQUID magnetometer, we have carried out neutron diffraction measurements on both the bulk and nano samples down to 2 K. Temperature-dependent (2–300 K) neutron diffraction (ND) measurements were carried out on samples (in powder form) using the multi-position-sensitive detector-based focusing crystal diffractometer set up by UGC-DAE Consortium for Scientific Research Mumbai Centre at the National Facility for Neutron Beam Research (NFNBR), Dhruva reactor, Mumbai (India) at a wavelength of 1.48 A° . For low-temperature data, vanadium cans filled with the samples were loaded in a Cryogenics make cryogen-free magnet system.

6.3 Results

6.3.1 Characterization of samples

The SEM images of the crystallites used in the experiments are shown in FIG. 6.2. FIG. 6.2(a) shows the representative image of the bulk sample and FIG. 6.2(b) shows the representative image of a typical nano sample. The formation of the proper chemical phase has been confirmed from room-temperature XRD for both the samples shown in FIG. 6.3[18]. The room-temperature XRD data also show that the two samples have differences in crystal structures, which we discuss later on.

The XRD data at room temperature for the bulk sample agree very well with the data given in reference [8], which are taken as standard.

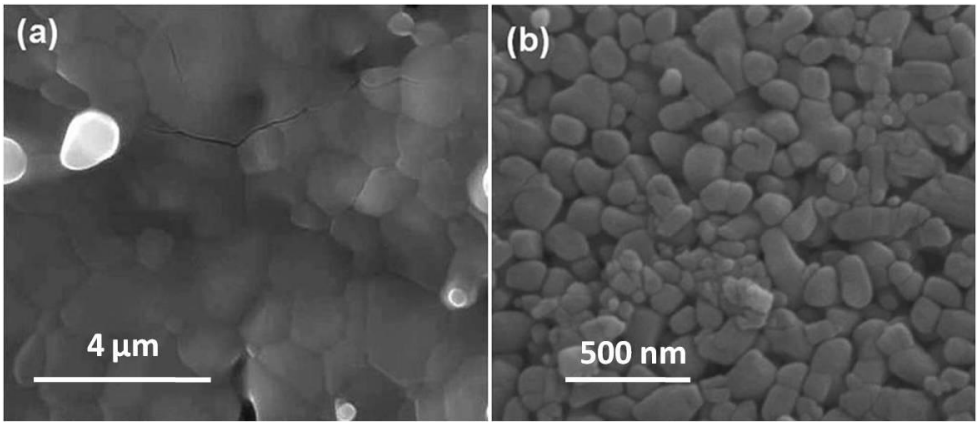

FIG. 6.2. SEM images of (a) the bulk sample (average crystallite size ≈ 1 µm) and (b) the nano sample (average crystallite size ≈ 75 nm).

The chemical tests done on the samples showed that the size reduction retains the stoichiometry. We note that this is an important observation. The Y:Ca:Mn average ratio obtained from ICP-AES is 0.502:0.498:1 which is very close to the expected ratio 0.5:0.5:1. The spatial variation of stoichiometry was checked in different regions of the samples with point EDAX. For the bulk sample, Y:Ca ratio is 1.02 ± 0.08 and for the nano sample, it is a similar number 1.05 ± 0.09. Iodometric titration results also show that the oxygen stoichiometry does not change much on size reduction. All the samples of $Y_{0.5}Ca_{0.5}MnO_{3+\delta}$ have similar small positive values of δ. The value of δ for the nano sample is ≈ 0.028 and for the bulk sample, it is ≈ 0.018. The above tests

ensure proper stoichiometry for both the samples. Since the COO in the Y-system is robust for small deviations from the exact half-doping, we expect no change in behavior due to a small variation in stoichiometry, if any.

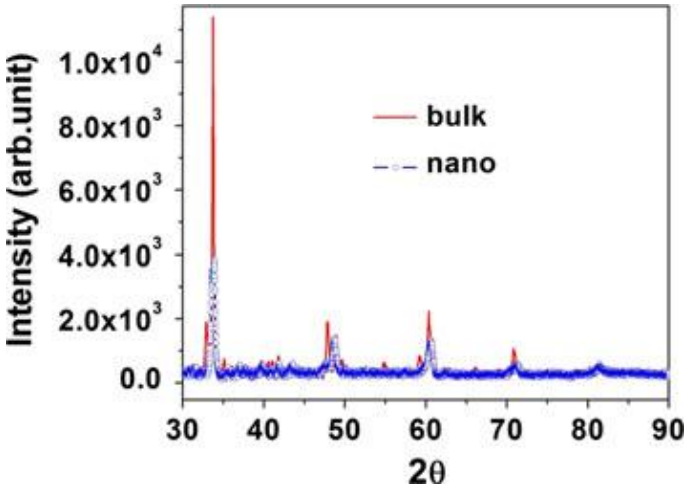

FIG. 6.3. Room-temperature XRD of bulk and nano samples of $Y_{0.5}Ca_{0.5}MnO_3$.

6.3.2 Crystal structure

One of the important structural aspects of manganites is that they generally develop an orthorhombic structure on cooling from high temperature. The formation of the COO depends on the nature of the orthorhombic distortion that develops in the system as it is cooled from high temperature. The temperature-dependent XRD data at high temperature captures this evolution. To evaluate the evolution of the orthorhombic structure in this material, the data were analyzed using Pbnm space group and the variations in the lattice constants *a*, *b*, and *c* is shown in FIG.6.4. The errors in the lattice constants are $\pm(1.5 \times 10^{-4}$ A^0 to 5.5×10^{-4} A^0), $\pm(1.5 \times 10^{-4}$ A^0 to 5.8×10^{-4} A^0) and $\pm(2.1 \times 10^{-4}$ A^0 to 8.1×10^{-4} A^0), for *a*, *b*, and *c* axes, respectively. The sizes of the data symbols in the figure are larger than the error bars. From the data, it can be seen that in the bulk sample, the Orthorhombic–Orthorhombic' (O–O') transition that shows up as a relative change in the size of *a* and $c/\sqrt{2}$ lattice constants, starts as a gradual transition at a rather high temperature $T \approx 750$ K. In most manganites (like $La_{0.5}Ca_{0.5}MnO_3$), the transition is generally sharp. The gradual onset of the O–O' transition seen on cooling is similar to that seen by previous investigations on bulk $Y_{0.5}Ca_{0.5}MnO_3$ [8-9]. In the bulk sample, the lattice constant *b* is much larger than the lattice constants, *a* and $c/\sqrt{2}$. This gives rise to a large distortion factor $D \approx 1.4$ %. (The factor D(%) is defined as $D = \left(\frac{100}{3}\right)\{\sum_{i=1.2.3}|(a_i - a_{avg})/a_{avg}|\}$, where $a_{avg} = (a \times b \times c/\sqrt{2})^{1/3}$. In the nano sample, there are important differences compared to the bulk as the temperature is varied. First of all, there is no discernible O–O' transition on size reduction and the structure is O' -orthorhombic for all temperatures, although the Pbnm space group is maintained. However, at room temperature, the distortion factor *D* is much less and ≈ 0.45 %. We will see below that there is no signature of onset of COO transition in the system as can be seen in the susceptibility data.

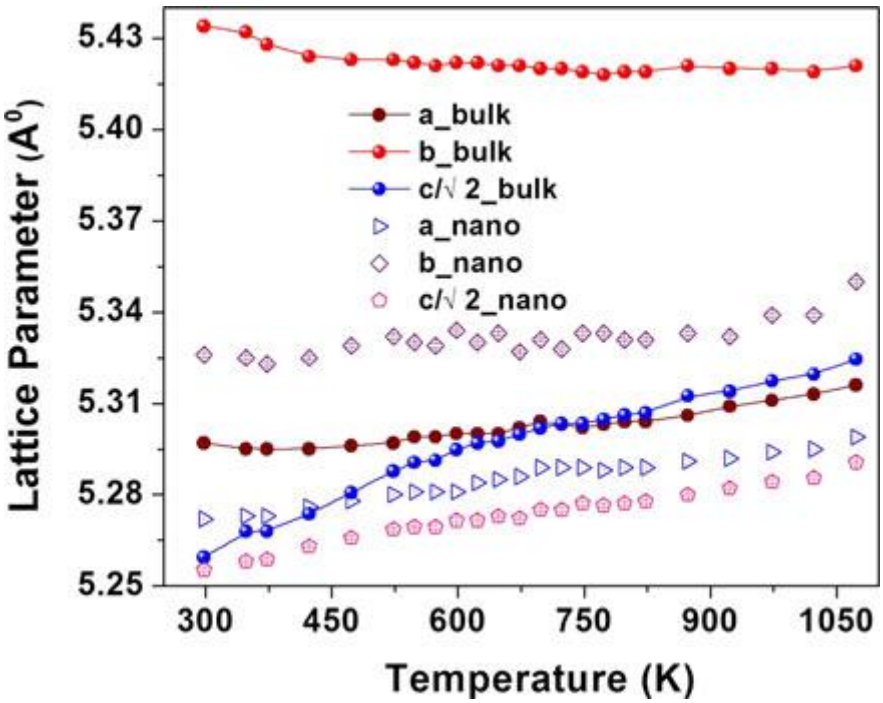

FIG. 6.4. Variation of lattice constants a, b, and c as a function of temperature in the region 300–1100K for both the samples of $Y_{0.5}Ca_{0.5}MnO_3$ as observed from the refinement of X-ray diffraction data. The error bars are smaller than the symbols. The errors in lattice constants are $\pm(1.5 \times 10^{-4}$ to 5.5×10^{-4} A^0), $\pm(1.5 \times 10^{-4}$ to 5.8×10^{-4} A^0), and $\pm(2.1 \times 10^{-4}$ to 8.1×10^{-4} A^0), for *a*, *b*, and *c* axes, respectively.

6.3.3 Magnetic measurements

In FIG. 6.5, we show the magnetic susceptibility (χ) data plotted as a Curie–Weiss plot (χ^{-1} vs. *T*). For the bulk sample, the T_{CO} is seen in the data as a change in slope at around 290 K. The low-temperature AFM transition shows up as a shallow feature in the change of slope in the vicinity of 110 K. This is similar to that observed in past investigations on bulk $Y_{0.5}Ca_{0.5}MnO_3$ [8,10]. We will show below that the presence of the AFM order can be seen clearly in the neutron diffraction data. From the high-temperature Curie–Weiss plot, we find that the Curie temperature (θ) is very small ≈ 20 K with an effective moment $\mu_{eff} \approx 0.49\ \mu_B$. The nano sample shows a distinctly different magnetic behavior compared to that of the bulk. There is no feature in the χ^{-1} versus *T* data that can be identified with the COO transition. Instead, the Curie–Weiss law is followed down to ≈150 K where it starts to show a deviation from the straight-line plot. The deviation shows formation of ferromagnetic moments and local order. The Curie constant, evaluated from the high-temperature data, however, gives a small moment $\mu_{eff} \approx 0.35\mu_B$. with a very small value of $\theta \approx -2$ K.

The value of μ_{eff} is much smaller than what one would expect from the ionic values of free moments on Mn sites. It can be appreciated that in an analogous system like $Pr_{0.5}Ca_{0.5}MnO_3$ or $La_{0.5}Ca_{0.5}MnO_3$, for both the nano as well as bulk samples, the value of θ is high (in the range of 200–250 K) and the value of the μ_{eff} is also close to what one would expect from the ionic moments [12-13].

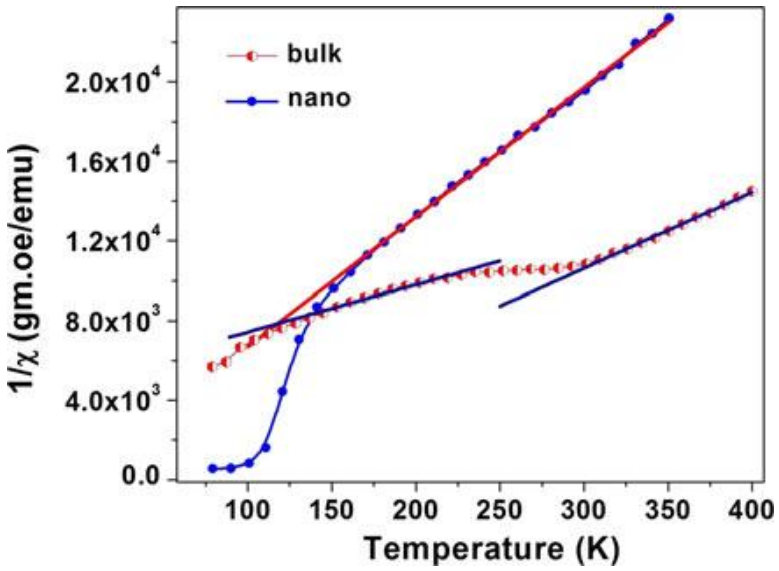

FIG. 6.5. Curie–Weiss plot for bulk and nano samples.

The differences in the magnetic behaviour of the two samples can also be seen in the magnetization data. The magnetization data measured in both field cooled (FC) and zero field cooled (ZFC) modes in a field of 700 Oe are shown in FIG.6.6. The bulk sample shows formation of very weak moment at ≈ 45 K, which is much lower than the value of T_N ≈ 110 K seen from the susceptibility data. For the bulk sample, the M–H data taken down to 5 K show weak field dependence and an absence of any hysteresis, as shown in FIG.6.7(a). The magnetization of the nano sample shows clear evidence of the formation of substantial ferromagnetic moments and a strong deviation from the bulk data. It is clearly seen that the magnetization of nano sample increases more rapidly below 100 K. The M–H curves shown in FIG.6.7(b) also show appearance of hysteresis below 100 K. Though the nano sample shows appearance of strong ferromagnetic moment, the magnetization does not saturate even up to a field of 3T. This would imply that there may be formation of canted spin order or the presence of local disorder arising from rather strong local random anisotropy field.

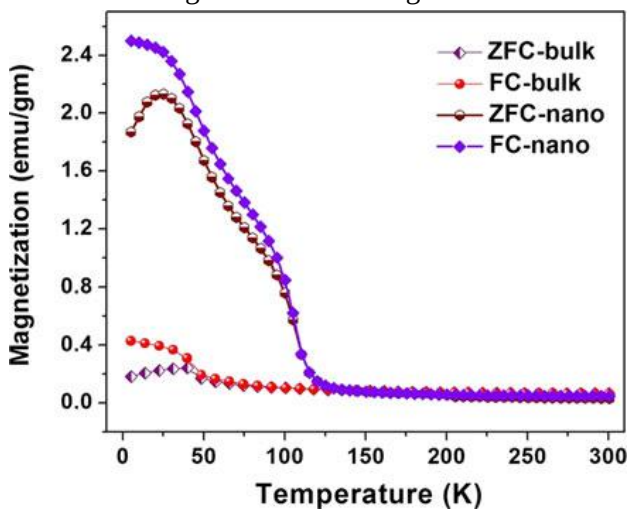

FIG. 6.6. Magnetization data measured in a field of 700 Oe.

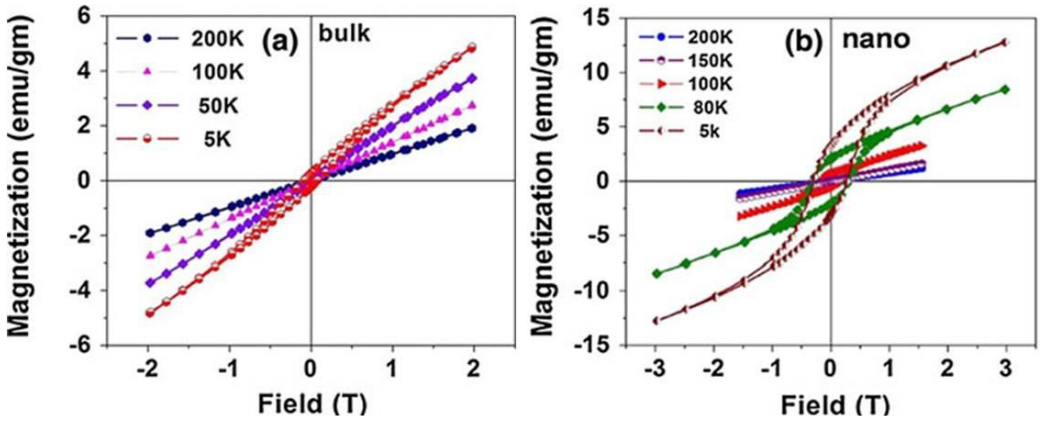

FIG. 6.7. M–H curves taken at different temperatures for (a) bulk and (b) nano sample.

6.3.4 Neutron diffraction

We have carried out neutron diffraction measurements on both bulk and nano samples with the limited scope to look for the presence or absence of AFM spin order at low temperatures. The peaks due to the AFM order appear at 2θ values below 20^0 for the wavelength of neutrons used. Examples of the magnetic peaks at 2 K are shown for both the samples in FIG.6.8. In FIG. 6.9, we plot the intensities of the lines as a function of temperature for both the samples. Appearance of the magnetic peaks due to AFM order occur below100 K. This is in broad agreement with the susceptibility data. The neutron data show that the AFM order seen in the bulk sample persists even in the nano sample, implying co-existence of a ferromagnetic moment along with the AFM order in the nano sample. This is unlike the systems $Pr_{0.5}Ca_{0.5}MnO_3$ or$La_{0.5}Ca_{0.5}MnO_3$, where the AFM order is completely suppressed when the particle size is reduced to this range [12-13]. Such strong suppression of AFM order is also seen in $Nd_{0.5}Ca_{0.5}MnO_3$ [14] as well as $Sm_{0.5}Ca_{0.5}MnO_3$ [19]. The neutron diffraction data in nanocrystals of $La_{0.5}Ca_{0.5}MnO_3$ show no peaks arising out of AFM order and there is formation of long-range FM order, similar to that seen in the ferromagnetic metallic compositions like $La_{0.67}Ca_{0.33}MnO_3$.

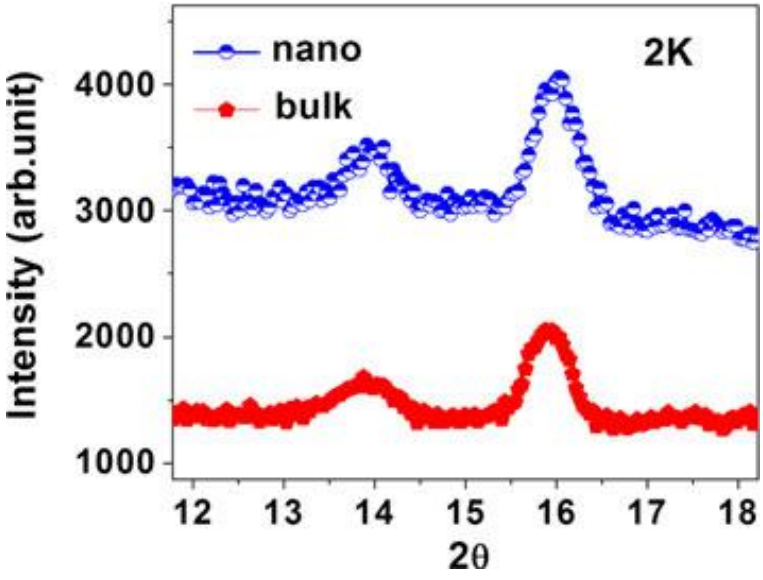

FIG. 6.8. Magnetic peaks due to antiferromagnetic order seen at 2 K by neutron diffraction for both the samples.

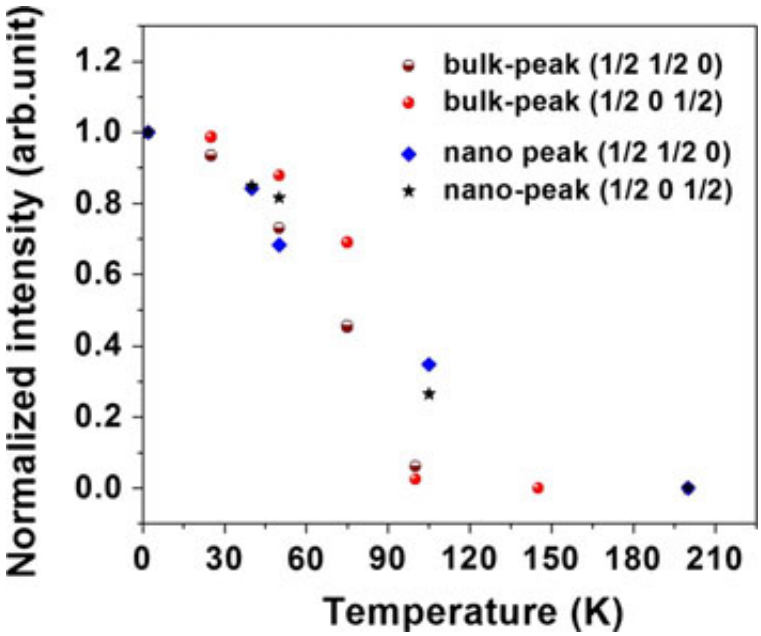

FIG.6.9. The temperature variation of the intensities of the antiferromagnetic peaks is shown. (hkl) values are shown in bracket for the bulk and nano samples. For both samples, the antiferromagnetic order sets in around 100 K.

6.3.5 Electrical Measurement

The resistivity measurements provide supporting evidence for the magnetic state of the sample. This is because formation of ferromagnetic moment leads to double exchange (DE) interaction that can lead to lower resistivity. We investigated the resistivity (ρ) as a function of T below 300 K. The data are shown in FIG.6.10. (a). For the bulk sample, even at 50 K, the resistivity reaches a very high value $\geq 10^9$ ohm.cm. In the $Y_{0.5}Ca_{0.5}MnO_3$ system, the resistivity at around room temperature is orders of magnitude higher compared to those of the bulk samples of La and Pr systems and this probably reflects small bandwidth and higher propensity of the electrons in this system to get localized. Compared to the bulk sample, the nano sample has a resistivity that is orders of magnitude less. For the nano sample, due to its significantly lower ρ, the measurements could be done down to 10 K. ρ of nano sample at room temperature is three orders less than the bulk counterpart and at lower temperature ($T \approx 50$ K), ρ is more than four orders lower.

In general, most solid oxide systems with nanocrystallites have much higher resistivity. Even in manganites that are ferromagnetic (like the CMR system $La_{0.67}Ca_{0.33}MnO_3$ or the ferromagnetic oxide $La_{0.5}Sr_{0.5}CoO_3$), the size reduction leads to enhancement of resistivity due to predominant contribution of resistivity from the grain boundaries that are much less conducting [20-21]. In the present system, when the COO is destabilized due to the size reduction, the appearance of double exchange (due to the ferromagnetic moments) makes the electrons delocalized leading to resistivity reduction in nano samples. The control of the electrical resistivity in such nanoparticle systems by tuning the ground state by size reduction is a new tool to engineer the resistivity of nanoparticles. This is in contrast to the conventional practice, where the control is done by tuning the contributions from grain boundaries.

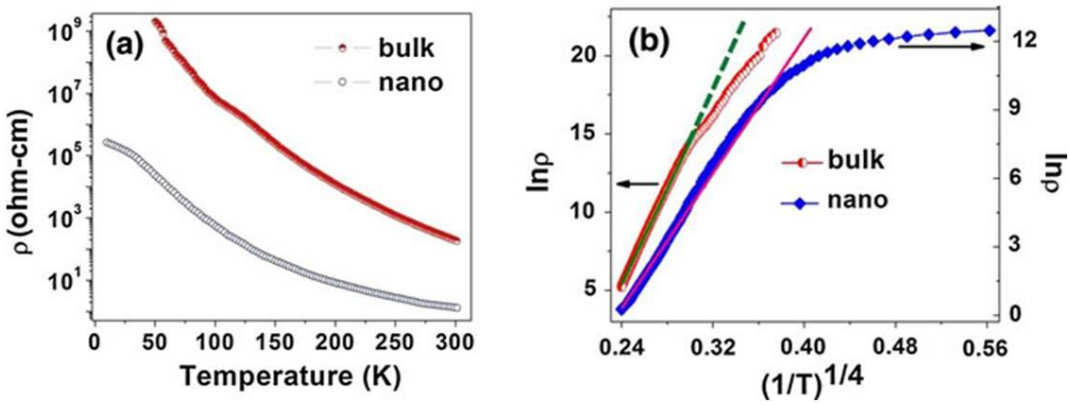

FIG. 6.10. (a) Temperature dependence of the resistivities of the bulk and nano samples. (b) ln ρ versus $T^{-1/4}$ plot shows the compliance to the variable range hopping relation.

The resistivity data for both the samples have regions in temperatures where they fit the variable range hopping (VRH) conduction (Mott and Davis Second Edition) which is given as:

$$\rho = \rho_0 \exp(T_0/T)^{1/4} \quad (6.1)$$

, where T_0 is the scale of energy which is dependent on the density of states and localization length and is given as $K_B T_0 \propto \alpha^3 N(E_F)^{-1}$ where α is the inverse localization length and N(E_F) is the density of states at the Fermi level E_F. ρ_0 is a constant giving the scale of resistivity and the carrier hopping distance. In FIG.6.10. (b), we have plotted ln ρ versus $T^{-1/4}$. For the bulk sample, the resistivity follows VRH relation over the whole temperature range, although there is a change in the values of the parameters at $T \approx 130$ K as can be seen from FIG.6.10(b). This temperature is much less than T_{CO}. It is likely that this is the temperature range where small ferromagnetic clusters may form in the system, which may not have large moments that can lead to a clear signature in the susceptibility but it may start to alter the local transport parameters. The value of T_0 is severely depressed (by nearly a factor of 5) at lower temperatures. This change can happen from an enhancement in N(E_F), or a decrease in α. It is likely that this occurs due to an increase in the localization length leading to a smaller α.

For the nano sample as well, the resistivity follows a VRH hopping relation down to ≈ 35 K and below that value, the temperature variation of ρ saturates. For the nano sample, the value of T_0 is significantly lower (by almost a factor of 20) compared to that of the bulk. This suppression is again a likely reflection of the enlargement of the localization length (α^{-1}) due to thecarrier delocalization arising from the formation of the ferromagnetic moment. Since the dependence of T_0 has a cubic power, a modest enlargement of the carrier localization length by a factor of ≈ 2.5 can lead the observed suppression of T_0.

6.4 Discussion

The data presented above show how size reduction into the nanometric regime can control the structural parameters in a nontrivial way, which in turn can change the physical properties. It is observed that thesize reduction of the system $Y_{0.5}Ca_{0.5}MnO_3$, like the other half-doped manganites of the $A_{0.5}Ca_{0.5}MnO_3$ family, can lead to significant changes in the physical properties. Compared to similar past studies on $Pr_{0.5}Ca_{0.5}MnO_3$ and $La_{0.5}Ca_{0.5}MnO_3$

systems (that have much larger average ionic radius r_A), it appears that though the COO transition is suppressed on size reduction, there are important differences. Similar destabilization of the COO state has also been reported in other systems like $Nd_{0.5}Ca_{0.5}MnO_3$ [14] and $Sm_{0.5}Ca_{0.5}MnO_3$ [19], which have the average ionic radii r_A lying between $Pr_{0.5}Ca_{0.5}MnO_3$ and $Y_{0.5}Ca_{0.5}MnO_3$. The studies presented here on the $Y_{0.5}Ca_{0.5}MnO_3$ system (which has the smallest r_A and the highest onset temperature for the COO transition) unambiguously establish that, irrespective of the system and the size of the cationic radius r_A, the COO transition observed in the half doped $A_{0.5}Ca_{0.5}MnO_3$ systems can be destabilized by size reduction of crystallites down to below 100 nm. This is a clear and unambiguous conclusion from the present investigation.

Our present investigation on the Y-based system, along with past investigations done by our group on the Pr- and La-based systems [12-13], show that the size reduction leads to a change in the lattice parameters while the space group remains unchanged. In recent theoretical studies [22] using DFT and DMFT carried out on nano clusters of $La_{0.5}Ca_{0.5}MnO_3$, it has been found that the COO ground state is destabilized with appearance of ferromagnetic state with de-localized electrons. The structure obtained by the theory was found to agree with experimental data and it was concluded that change in structural parameters on size reduction plays a dominant role in destabilizing the COO state along with the accompanying AFM spin order. From this investigation and also from the available data, it is clear that the extent of relative changes in the lattice parameters differ significantly as one goes across the series from La to Y. We can elucidate this using the changes in the orthorhombic distortion parameter (D) that changes as the ionic radius changes and also shows nontrivial distortion on size reduction. We show the variation of D as a function of the ionic radius r_A for both the bulk and nano samples in FIG.6.11. The data are taken from the lattice constants measured in this investigation, past investigations done by our group on La- and Pr-based systems [12-13], and published data on Nd-based system [14]. If we assume 300 K as the reference point, $D \approx$ 0.06 % for the bulk $La_{0.5}Ca_{0.5}MnO_3$ system, which is very small. However, it changes significantly and becomes ≈ 1.05 % when the crystallite size is taken down to below 30 nm. In bulk $Pr_{0.5}Ca_{0.5}MnO_3$, the D parameter is somewhat larger (≈ 0.18 %) and a size reduction to similar size range leads to its enhancement to ≈ 0.66 %. For the $Nd_{0.5}Ca_{0.5}MnO_3$, the D factor for both the samples appears to be close although it is somewhat smaller for the nano sample. In case of the $Y_{0.5}Ca_{0.5}MnO_3$, D in bulk has the largest value of ≈ 1.35 % at 300 K while it has a lower value of ≈ 0.45 % in the nano sample. It is interesting that the dependence of the distortion factor D on r_A is opposite in the bulk and the nano samples.

The structure and the orthorhombic distortion in the $A_{0.5}Ca_{0.5}MnO_3$ system, as stated before, depend on two competing factors, namely, the stearic effect arising from the ionic size and from the Jahn–Teller distortion around the Mn^{3+} ions. It is seen that there is a gradual increase of D as r_A is reduced, possibly reflecting the relative enhancements of the stearic effects in small r_A systems. However, the relative variation of D on size reduction appears to reflect an inverse trend and is not immediately explainable. The resulting structure and the D parameters on size reduction appear to reflect the relative strengths of the two competing effects that lead to the orthorhombic distortion.

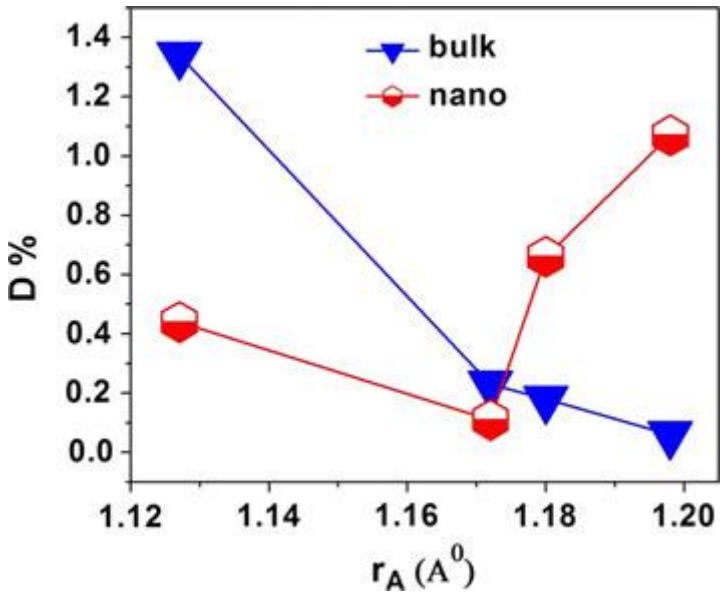

FIG. 6.11. Distortion parameter *D* (%) plotted as function of the average ionic radius r_A for half-doped manganites, for both bulk and nano samples. The ions in order of decreasing ionic radii are La, Pr, Nd, and Y. References for La-, Pr-, and Nd-based systems are given in text.

In case of $Y_{0.5}Ca_{0.5}MnO_3$, the low-temperature neutron diffraction data suggest the presence of AFM order even in the nano sample, although there is formation of weak ferromagnetic moments as well as appearance of hysteresis loop at low temperatures. The AFM spin order in $Y_{0.5}Ca_{0.5}MnO_3$seems to be more rugged compared to the other half-doped systems, where the AFM order is suppressed to a much larger degree. We also note that in the present investigation, the size could be reduced only down to around 75 nm while retaining the chemical fidelity of the sample. The magnetic phases in half-doped manganites arise from a competition of antiferromagentic superexchange interactions and strong double exchange interactions when ferromagnetic moments are present. The last interaction also delocalizes the electrons. The resulting magnetic phases will depend on the relative strengths of the two magnetic interactions which in turn are decided by the structure itself. The stability of the AFM spin order (or its absence) in size reduced systems will thus depend on details of the resulting structure.

Though the COO transition is strongly inhibited by size reduction in all the systems studied, the extent of ferromagnetic moment formation and the resulting ferromagnetic order seem to vary. In case of $La_{0.5}Ca_{0.5}MnO_3$ and $Pr_{0.5}Ca_{0.5}MnO_3$, the AFM order was strongly suppressed and though there were coexisting phases, there was long-range ferromagnetic order formation as seen by neutron diffraction studies done on nanocrystallites. Some of the previous studies on nanocrystallites of manganites $Nd_{0.5}Ca_{0.5}MnO_3$ and $Sm_{0.5}Ca_{0.5}MnO_3$ [14,19] have reported formation of core–shell structure that has AFM core and a disordered ferromagnetic shell which also shows appearance of exchange bias. In our system, such a phenomenon has not been seen. In these samples (Nd- and Sm-substituted samples), however, there is no magnetic neutron diffraction data that can rule out formation of long-range FM order.

6.5 Conclusion

To conclude, we have studied the stability of charge and orbital order in nanocrystals of half-doped manganite $Y_{0.5}Ca_{0.5}MnO_3$. The COO that takes place in the bulk close to the room temperature gets suppressed on size reduction to sizes below 100 nm. This is accompanied by

changes in lattice parameters and the orthorhombic strain. The AFM order is retained within the nanocrystallites although there is formation of strong ferromagnetic moment which leads to an observable hysteresis loop at low temperatures. The formation of the ferromagnetic moment and the onset of double exchange interaction delocalize the electrons leading to substantial reduction in ρ in the nanocrystallites.

The physics of size reduction in complex oxides is interesting because a number of competing interactions are involved and the size reduction affects the competing interactions to different degrees. The specific example discussed in this paper brings out how factors like ionic size matter in stabilizing the ground state in such systems when the size is reduced to nanometric range.

References

1. C N R Rao and B Raveau(eds) (1998). *World Scientific, Singapore*, pp 1–42 (1998).
2. A Arulraj, P N Santhosh, R Srinivasa Gopalan, A Guha, A K Raychaudhuri, N Kumar and C N R Rao. *J Phys. Condens. Matter*. **10**, 8497 (1998).
3. P G Radaelli, D E Cox, M Marezio and S W Cheong, *Phys. Rev. B.* **55**, 3015 (1997).
4. S Mori, T Katsufuji, N Yamamoto, C H Chen and SW Cheong, *Phys. Rev. B.* **59**, 13573 (1999).
5. T Vogt, A K Cheetham, R Mahendiran, A K Raychaudhuri, R Mahesh and C N R Rao, *Phys. Rev. B.* **54**, 15303 (1996).
6. E Pollert, S Krupicka and E Kuzumicova, *J Phys. Chem. Solids*. **43**, 1137 (1982).
7. A Arulraj, R Gundakaram, A Biswas, N Gayathri, A K Raychaudhuri and C N R Rao, *J Phys. Condens. Matter*. **10**, 4447 (1998).
8. M Dlouha, S Vratislav, Z Jirak, J Hejtmanek, K Knizek and D Sedmidubsky, *Appl. Phys. A.* **74**(Suppl),S673–S676 (2002).
9. M TCausa, H Aliaga, D Vega, M Tovar, B Alascio, H R Salva and E Winkler, *J Magn. Magn. Mater*. **81**, 272 (2004).
10. Y Su, Z Chen,Y Li, D Deng, S Cao and J Zhang , *J Supercond. Nov. Magn*. **23**, 501 (2010).
11. S S Rao, S Tripathi, D Pandey and S V Bhat, *Phys. Rev. B.* **74**, 144416 (2006).
12. T Sarkar, P K Mukhopadhyay, A K RayChaudhuri and Sangam Banarjee, *J Appl. Phys*. **101**, 124307 (2007).
13. T Sarkar, B Ghosh, A K Raychaudhuri and T Chatterji, *Phys. Rev. B.* **77**, 235112 (2008).
14. L. Liu, S. L. Yuan, Z M Tian, X Liu, J H He, P Li, CH Wang, X F Zheng and S Y Yin, *J Phys. D (Appl Phys)*. **42**, 045003 (2009).
15. S K Giri, A Poddar and T K Nath, *Aip Adv*. **1**,032110 (2011).
16. Z Jirak, E Hadova, O Kaman, K Knizek, M Marysko, E Pollert, M Dlouha and S Vratislav, *Phys. Rev. B.* **81**,024403 (2010).
17. K S Shankar and A K Raychaudhuri, *J Mater. Res*. **21**, 27 (2006).
18. Z Q Li, D X Zhang, X H Zhang, Y Q Gao, X J Liu and E Y Jiang, *Phys. Lett. A*. **370**, 512 (2007).
19. S K Giri, A Poddar and T K Nath, *Aip Adv*. **1**, 032110 (2011).
20. B Ghosh, S Kar, L K Brar and A K Raychaudhuri, *J Appl. Phys*. **98**, 094302 (2005).
21. T Sarkar, A K Raychaudhuri, A K Bera and S M Yusuf, *New J Phys*. **12**, 123026 (2010).
22. H Das, G Sangiovanni, A Valli, K Held and T Saha-Dasgupta, *Phys. Rev. Lett*. **107**, 197202 (2011).

Summery and Conclusion

In this thesis we have investigated properties of manganite nanoparticles with down to diameter ~5nm for their change in property when their oxygen stoichiometry is changed without changing their size. For this we used electrochemical oxidation reduction that allows change of oxygen stoichiometry at room temperature. This is unlike what happens in thermal oxidation/reduction that necessarily leads to growth of particle size. The important points of achievements are enumerated below:

1. In this thesis we have developed an apparatus to do electrochemical oxidation (and reduction) in a controlled way and used it to achieve nanoscopic control of oxygen stoichiometry in nanoparticles of manganites. The electrochemical oxidation is a valuable tool to control oxygen stoichiometry because more common thermal method leads to grain growth as the sample is heated.

2. In the nanograined sample of $La_{0.67}Ca_{0.33}MnO_{\delta}$ as its bulk sample phase diagram, T_C is maximum for $\delta = 3$ but beyond a band of hole doping (higher and lower value) the AFM phase sets in. We showed by the ferromagnetism persists for a wide range of stoichiometry δ from 2.74 to 3.20.

3. In half-doped nanoparticles of $A_{0.5}Ca_{0.5}MnO_3$ where FM state persists, we showed that the change in physical property brought about by electrochemical oxidation has a nontrivial dependence on disorder that arises from variation in A-site cationic radii.

4. We have also showed how by localized control of oxidation in a sub-micron strip of oxygen , as can be done by combining electro-chemical oxidation with Lithography, the oxygen can be moved by an electric current from a localized source.

5. We also showed stability of charge and orbital order in nanocrystals of half-doped manganite $Y_{0.5}Ca_{0.5}MnO_3$. In nanocrystalline system FM state arises and coexists with the AFM state.

Annexure

Relaxation dynamics of oxygen in manganites after electrochemical oxidation

In this work we have studied the resistance relaxation due to oxygen disorder around room temperature on the surface of two different types of perovskite systems (robust charge and orbital ordered (COO) insulating state and insulator to metal (IM) phase boundary). For COO and IM phases we have used the films of $Y_{0.5}Ca_{0.5}MnO_3$ (YCMO) and $La_{0.85}Sr_{0.15}MnO_3$ (LSMO) grown on $LaAlO_3$ (LAO) substrate. Electrochemical method has been used to oxidize the samples where isothermal resistance measurement was used to study the dynamic motion of oxygen diffusion. Experiment shows that around room temperature in the COO phase the Debye type relaxation is more favourable than the non Debye type relaxation where in IM phase non Debye is the dominant process. The large localized polaron formation in COO phase is the reason of Debye type relaxation where non Debye relaxation process governed by the formation of small mobile polarons.

A1. Introduction

The oxygen sensitivity and possible mechanisms of oxygen diffusion of perovskite oxides specially near room temperature is an unsolved problem. Whether the spontaneous diffusion of oxygen near room temperature favours the Debye or non Debye kind of relaxation in different class of perovskite system (Charge and orbital order system (COO) and insulator to metal phase boundary (IM)) is a fundamental unknown issue in the physics of manganite. Previous experiments of oxygen isotope exchange on $La_{0.5}Ca_{0.5}MnO_3$, $Nd_{0.5}Sr_{0.5}MnO$ [1], $La_{0.85}Sr_{0.15}MnO_3$ [2], $SrRuO_3$ [3], $(La_{0.5}Nd_{0.5})_{0.67}Ca_{0.33}MnO_3$ [4] etc. confirmed the polaron assisted shifting of ferromagnetic transition temperature and Charge and orbital order transition temperature of relevant compounds. In the isotope exchange of $La_{0.5}Ca_{0.5}MnO_3$ [1] showed that the replacement of O_{16} by O_{18} the charge and orbital order(COO) transition temperature was shifted towards the higher temperature and for that the COO system became more robust due to the creation of heavy polarons. Zhao et al. [3] observed in $La_{1-x}Ca_xMnO_3$ and $La_{1-x}Sr_xMnO_3$ [2] shifting in ferromagnetic transition temperature to lower temperature value due to isotope exchange of O_{16} by O_{18} but this shifting is much larger in $La_{1-x}Ca_xMnO_3$ than $La_{1-x}Sr_xMnO_3$ which addresses the issue of average cation radius of A-site cations. These studies revels that in charge ordered systems with smaller cation radius there is a possibility of the formation of large localized polarons than ferromagnetically ordered systems with larger cation radius which may have the presence of small mobile polarons. How does this polaron formation affect the diffusion mechanism of oxygen in different classes of manganite system? This unanswered question is our motivation. However oxygen diffusion in high temperature ($> 500^0$C) is a well studied work [5-9] due to its application as a ion conductor in solid oxide fuel cell. People were using electrical transport property as a tool to understand the diffusion mechanism. In most of those cases the oxygenation was done by heat treatment along with varying the oxygen partial pressure in the chamber. The oxygen diffusion at those high temperatures occurs at a very fast time scale (~ few seconds to few minutes) which is completely uncontrolled and after the oxygenation process the film became homogeneously oxygenated [5-9] and the diffusion mechanism obeys Debye type of relaxation. But this process totally looses the information regarding the spontaneous diffusion mechanism. Again there is no such study of oxygen diffusion in these systems at room temperature. Using this method the diffusion study of oxygen at room temperature is impossible. We have used electrochemical oxidation to oxidise the samples near room temperature. While electrochemical oxidation has been used in the past on $La_{0.2}Sr_{0.8}CoO_{3-\delta}$ [10], $La_4Ni_3O_{10}$ [11], $La_2CuO_{4+\delta}$ [12] to control oxygen but using it as a controlled source in diffusion study has not been done till today. After incorporation of oxygen to the system, it undergoes to a disordered situation and tries to order itself by diffusing oxygen ions to vacant sites. The electronic transport property of these perovskite oxides are strongly depends on the oxygen stoichiometry inside the material. Oxygen diffusion, dynamically changes the stoichiometry that can be perfectly studied by measuring the time relaxation of resistance.

Here we have chosen two different classes of manganite systems where one has the possibility of the formation of large size oxygen polarons and the other have the possibility of the formation of small mobile polarons. For the first case we used $Y_{0.5}Ca_{0.5}MnO_3$ (YCMO) which has the smallest cation radius and the highest charge and orbital order transition temperature ~ 290K in the half doped $A_{0.5}Ca_{0.5}MnO_3$ family [13]. On the other hand for the second case we have chosen $La_{0.85}Sr_{0.15}MnO_3$

(LSMO) which exists in the insulator to metal phase boundary [14]. The oxygen diffusion dynamics in these two different classes of systems near room temperature is a matter of interest. For a fixed temperature we have incorporated oxygen on the surface of the films by electrochemical method and after that we have studied the time dependent resistance profile of that films. To determine the diffusion length of oxygen in samples oxidized at 300K we have taken cross-sectional energy dispersive X-ray (EDX) spectroscopy and scanning electron microscopy (SEM) images. Our experimental result shows that the activation energy of Debye relaxation is small compared to the non Debye relaxation for these kinds of samples but the Debye relaxation is more favorable at lower temperature and also the strength of Debye relaxation is much greater in COO system than IM system.

A2. Experimental

The films are grown on (100) oriented LAO substrates from stoichiometric targets ($La_{0.85}Sr_{0.15}MnO_3$ and $Y_{0.5}Ca_{0.5}MnO_3$) using pulsed laser deposition technique. The chamber oxygen pressure was maintained during the deposition and cooling process at 1×10^{-1} mbar. The fluence was used 1.8 J/cm^2. The optimized shot frequency was 3 Hz and the target frequency was 20 Hz. The optimized substrate temperature was 700 ^{0}C and the substrate was pre-annealed for 1 hrs before deposition and after deposition it was post annealed for 5 hrs. We have cooled the sample very slowly (0.5 ^{0}C/min) to avoid any abrupt crack developing in the sample which may act as fast diffusive path for oxygen ions. We have used A.C technique to measure the resistance relaxation of the samples so that it will not affect the spontaneous ion motion (Oxygen ion) during the resistance measurement. We have used samples of 2.5 mm × 2 mm dimension. The thickness of the samples was measured from cross-sectional FEG-SEM images. The composition was confirmed from EDX. The surface morphology of the samples was studied by atomic force microscope (AFM) images. The average grain size obtained from AFM is ~ 29 nm(± 6 nm) for YCMO and ~ 25 nm(± 5 nm) for LSMO. The surface roughness obtained for YCMO is ~ 1.4 nm and that for LSMO is ~ 1.5 nm. So, YCMO and LSMO have near about the same surface morphology. From the cross sectional EDX data for the as prepared samples La:Sr ratio is 5.66 (± 0.19):1 and Y:Ca ratio is 1.00(± 0.007):1 respectively.

The schematic of the device structure and the experimental process is described in FIG.1. Here we used

conventional pseudo four probe method to measure the resistance of the samples. Photo lithography technique was used to make the silver (Ag) electrical contact pads on thin films. A.C current was generated by Lock-in-amplifier (LIA) and passes through the film with a high resistance (*R*) in series to make the current constant. To know the value of A.C current we used a Digital multimeter (DMM) across *R*. The voltage across the sample was measured by the same LIA. We have used standard three electrode system for electrochemical oxidation of the samples near room temperature. In the three electrode system Pt was used as counter electrode (cathode), Hg/HgO as reference electrode, sample as working electrode (anode) and 1(M) KOH solution as electrolyte. Except a window on the film surface (created by electron beam lithography), the total sample including the contact pads were covered by PMMA resist to avoid any charge deposition on the Ag pads. Metal contact pads were used for the oxidation as well as for the electrical resistance measurement. During the resistance measurement we replaced KOH electrolyte by de-ionised water (DI) to reduce the unnecessary charge deposition at the time of measurement and to make a constant thermal bath. The whole deposition system was immersed in a Julabo set-up to maintain constant temperature in the sample.

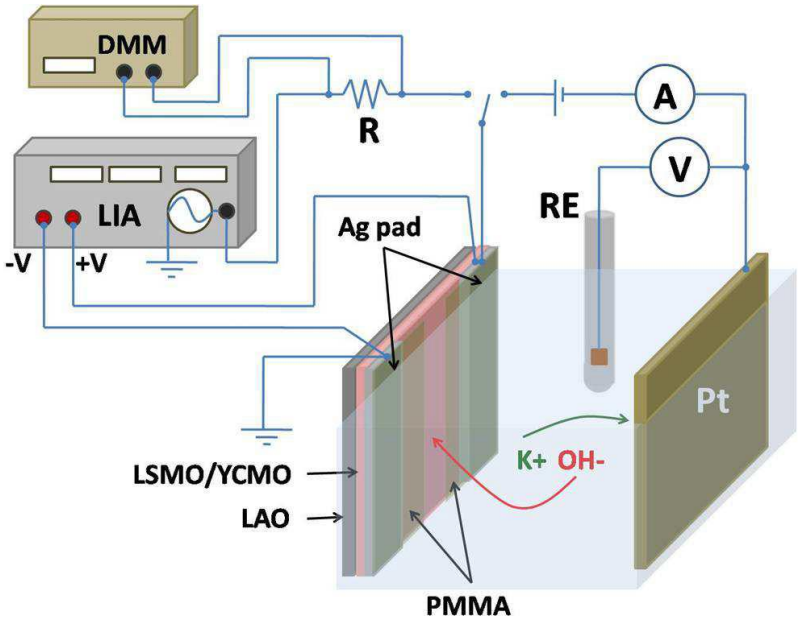

FIG. A.1. Schematic diagram of the device structure and the experimental set up.

At a particular temperature, both the films YCMO and LSMO were oxidized with a charge per unit volume ~ 10^{11} C/m^3. Immediate after the oxidation, time dependent resistance relaxation of the films has been measured. The threshold current density for electro migration of oxygen ions for these kinds of oxides is 10^3 to 10^4 A/cm^2, previously reported from our group [15]. We have used the current density for the measurement of resistance relaxation ~ 10^{-1} A/cm^2 which is far below from the threshold value of electro migration. In addition of these as we have used alternating current to capture the dynamics of oxygen motion it will not affect in any way the spontaneous oxygen ion diffusion in the sample.

A3. Results and Discussion

In FIG.2 we have plotted the resistance change $[\Delta R(t)(= R(t) - R(0))]$ with respect to time at three different temperatures for every sample. Here *R*(*t*) denotes the resistance value at time t and R(0) is the value of resistance at time t = 0 and also we have plotted colour contour plot of derivative of normalised resistance change with respect to time and temperature for each sample. Here $r = \Delta R(t = 0)/\Delta R(t = 24\,hrs)$ for YCMO and $\Delta R(t = 0)/\Delta R(t = 12\,hrs)$ for LSMO. We can see from the contour plot of FIG. A.2 that initially at higher temperature the rate of change of normalised resistance change is faster but as time increases the reverse case arises where at lower temperature the rate of normalised resistance change increases for both the samples. As the temperature increases the resistance reaches to equilibrium situation more rapidly this is because of the fact that thermal energy is helping to destroy the disorder condition developed in the system after the incorporation of oxygen.

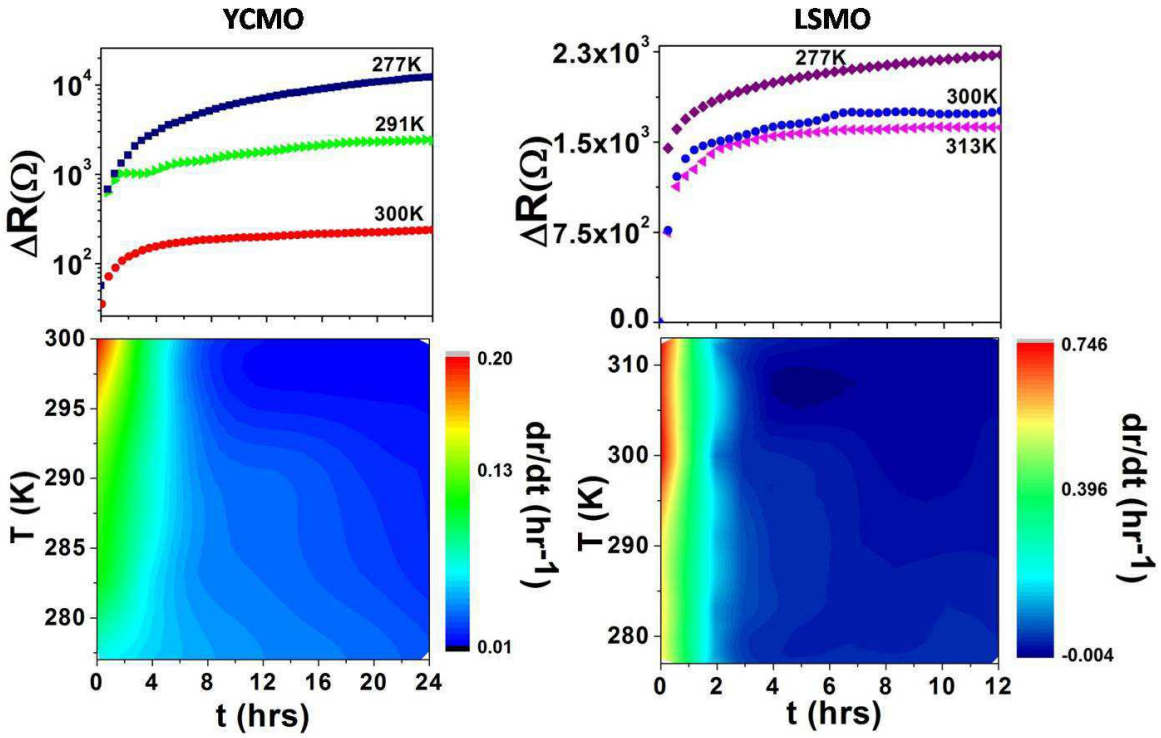

FIG. A.2. The variation of resistance change after deposition with time at three different temperatures and derivative of normalised resistance change with respect to time is shown.

Relaxations in ordered systems (like ferroelectrics undergo a second order phase transition below a critical temperature) can be explained by Debye like relaxation which follows $e^{-(t/\tau)}$ kind of dependency where τ is the relaxation time. The disordered systems like glass, where a distribution of relaxation time scales exists obeys non Debye type relaxation (namely relaxor like relaxation) which follows $e^{-(t/\tau)^{\beta}}$ with β ranges from 0 to 1. In order to obtain the quantitative evolution of time scales we have fitted our data with $\Delta R(t)(= R(t)-R(0))$ versus time with the functional form given below,

$$\Delta R(t) = A\left(1 - e^{-\left(\frac{t}{\tau_1}\right)}\right) + B\left(1 - e^{-(t/\tau)^{\beta}}\right) \quad (1)$$

The first term corresponds to Debye type relaxation and the second term corresponds to non-Debye type relaxation. Where A and B are constants. For our systems β ranges from 0.43 to 0.47. The ratio of A and B gives the strength of Debye relaxation over non-Debye relaxation. FIG. A.3 shows the fitting of equation (1) on the resistance relaxation at 300 K for both YCMO and LSMO systems. From the inset of FIG. A.3 it is clear that as the temperature increases the strength of Debye relaxation over non Debye relaxation decreases for both the COO (YCMO) and IM (LSMO) systems. But the ratio is one order greater in COO system than IM system. Which supports that Debye type relaxation is more favorable in COO systems than the IM systems.

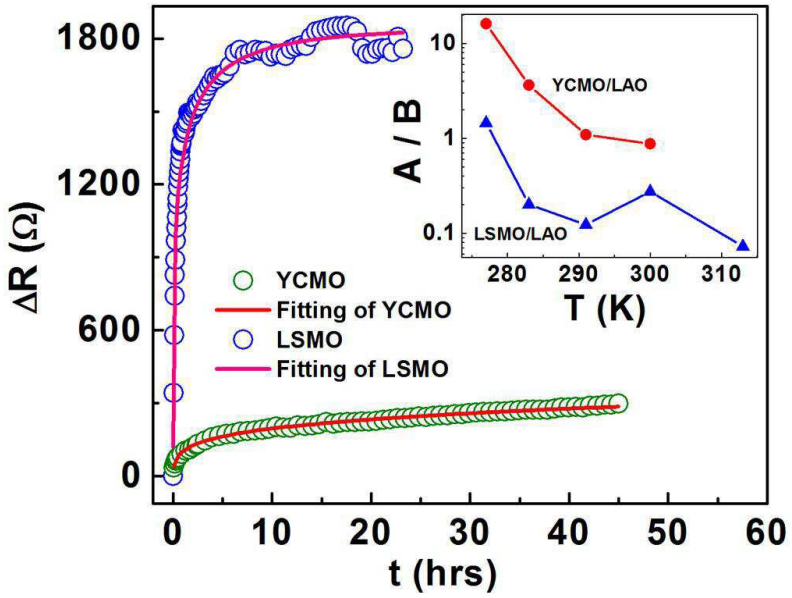

FIG. A.3. Experimental resistance relaxation and fitted curve using equation (1) at room temperature (300 K) is shown. The inset shows the strength of two relaxation processes.

The average time constant $< \tau >$ is defined as $(\tau/\beta)\Gamma(\beta)$ and the Arrhenius type of temperature dependency for the average time constant $< \tau >$ is given by,

$$< \tau > = \tau_0 e^{\frac{E_a}{K_B T}} \quad (2)$$

Using equation (2) the values of activation energy E_a and τ_0 have been found from FIG. A.4 for each relaxation processes and the results are tabulated in TABLE AI.

TABLE AI. Summary of important parameters of the samples studied.

Sample-ID	Activation energy for Debye (eV)	τ_0(sec) for Debye	Activation energy for non Debye (eV)	τ_0(sec) for non Debye
YCMO	0.25	1.58×10^{2}	0.90	1.68×10^{-11}
LSMO	0.31	1.91×10^{-3}	0.72	8.78×10^{-9}

It is clear from TABLE AI that activation energy for Debye relaxation is smaller for both the systems but in COO system Debye is favorable below room temperature the reason may be large cluster of oxygen ions near the surface of YCMO films (large static polarons) and as the temperature reaches to 300K the Debye and non Debye relaxation gets equal priority in the COO systems, this may be due to the reason that temperature is helping to break large polaron clusters in to small mobile polarons in which non Debye relaxation enhances. However at low temperature (277K) for IM system the Debye and non Debye relaxation gets equal priority and at higher temperature the non Debye process wins over the Debye. This result conclusively supports the small mobile polaron formation in the IM systems than COO system.

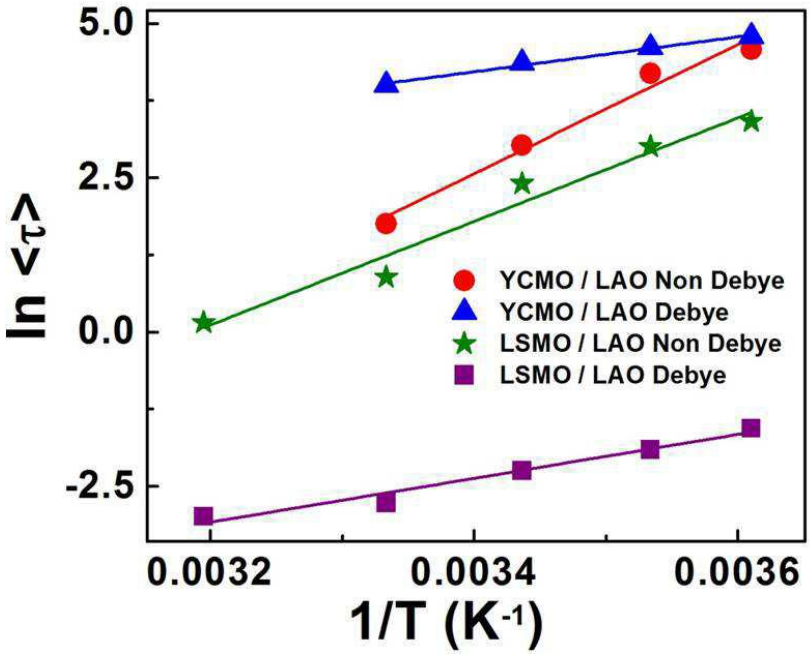

FIG. A.4. The $ln < \tau >$ vs $1/T$ plot for YCMO and LSMO films are shown.

Due to the externally applied oxygen ions, large polarons are created into the robust COO system. The oxygen diffusion length due to this large polaron formation must be less than the diffusion length due to the small mobile polarons. FIG. A.5. (a) shows the cross sectional SEM images of YCMO and LSMO films grown on LAO substrate which have oxidized at 300 K. The oxygen ions were diffused along the depth (z-direction) of the films. Inside the film we can see a clear colour contrast and EDX spectroscopy (FIG. A.5. (b) and (c)) shows that the contrast is created for different oxygen concentration. Similar observation was found by Locquet et al [16-17] on the surface of Lu_2CuO_4 thin films with locally oxidized regions. To obtain a quantitative estimation of average value of diffusion length of the oxygen ions along the thickness of the films we have fitted the normalized atomic percentage of oxygen versus depth data along the lines marked in FIG. A.5. (b) with the equation,

$$\frac{\Delta C}{\Delta C_0} = C_1 e^{-(z-r)^2/2L^2} \tag{3}$$

, where C_1 is a constant, r is the average depth of the implanted ions , L is the diffusion length. The average value of L is ~ 25 nm for YCMO and it is ~ 250 nm for LSMO. The diffusion length is one order lesser in COO system than the IM system which clearly indicates the existence of the large size oxygen polarons in COO and the formation of small mobile polarons in IM. Again Debye relaxation is more dominant process in COO phase. Therefore large polaron formation favours the Debye type of relaxation in contrast of IM phase where small mobile polaron formation favours the non Debye type relaxation.

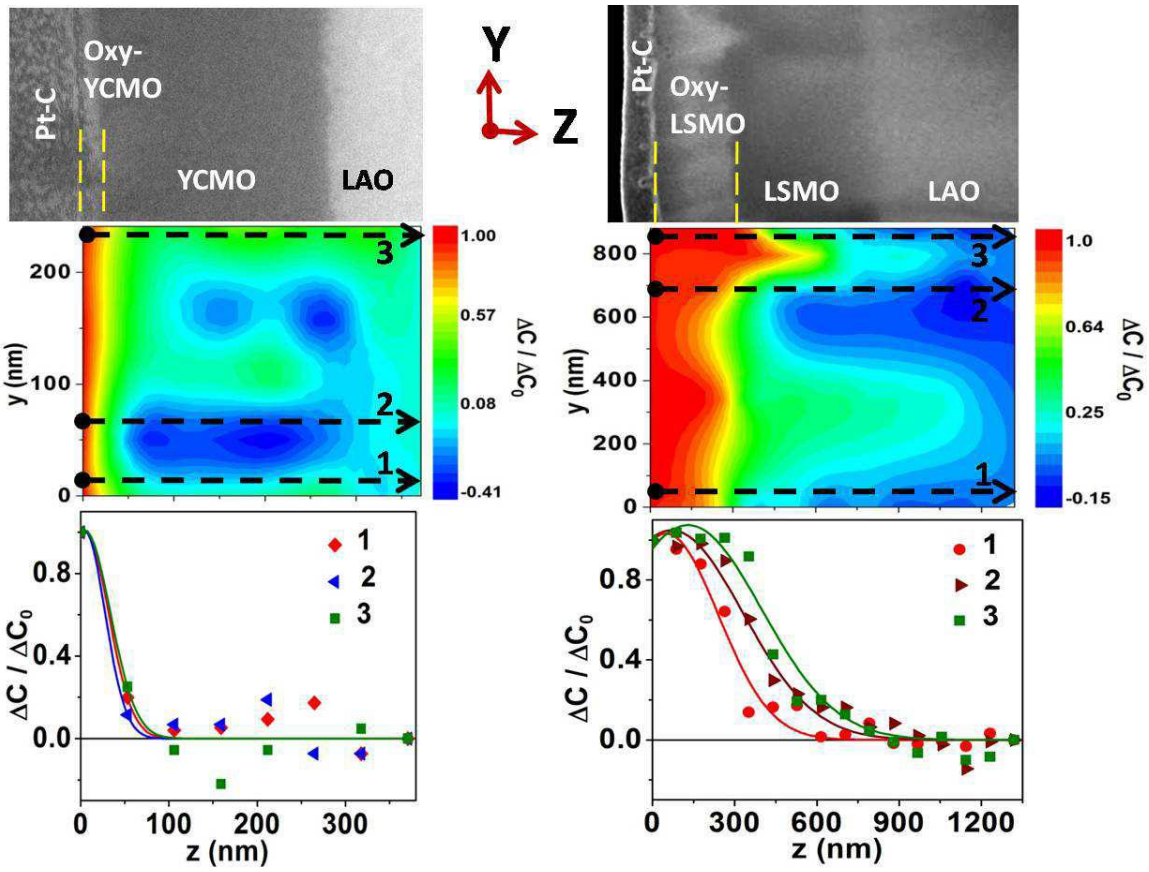

FIG. A.5. Left side is for YCMO and right side is for LSMO. (a) The cross-sectional SEM image. Distinct regions are mentioned by text. The dashed yellow line shows the diffused oxygen region (Oxy-YCMO/Oxy-LSMO). (b) Colour contour plot of normalised concentration ($\Delta C/\Delta C_0$) along the y and z direction. $\Delta C = C - Cs$, where 'C' is the atomic concentration of oxygen. Cs is the base concentration at LAO substrate and ΔC_0 is the ΔC value at z = 0 nm.(c) Line mapping of oxygen $\Delta C/\Delta C_0$ along the z-axis for three different lines indicated in (b).

A4. Conclusion

This work summarises that the activation energy of Debye relaxation is smaller than the non Debye relaxation processes in perovskite systems studied. Due to this reason the Debye relaxation dominates over the non- Debye relaxation process at low temperature. Large size polarons occurs in COO system and it favours the Debye relaxation process. The EDX spectra show that small range diffusion occurs in YCMO (COO system). It boldly supports the previous works which indicated the formation of large polarons in the COO system than IM systems. Again we did the first time investigation of the spontaneous oxygen diffusion inside the pervoskite films with different classes around the room temperature. Oxygen diffusion length strictly depends on the nature of the perovskite films. The charge ordered perovskites with small cation radius are prone to the formation of large static polarons resulting small diffusion length. Whereas the oxides with large cation size which have no charge and orbital ordering are prone to the formation of small mobile polarons with large oxygen diffusion length. The work also shows that the electrical transport property (resistance) is an excellent tool to understand the oxygen motion inside this kind of materials. It also shows that the electrochemical oxidation process is a very powerful but easy technique to locally oxidized samples around room temperature. Room temperature oxidation can create different oxygenated layer or different

conductive layers in a pervoskite film. This conclusion has been boldly supported from the EDX spectroscopy along the depth of the oxidized films. Using this electrochemical oxidation method with the integration of lithographic tools, one can make localized oxygen concentrated regions on a pervoskite film for a device structure for room temperature applications.

References

1. G. M. Zhao, K. Ghosh, H. Keller and R. L. Greene, *Phys. Rev. B.* **59**, 1 (1999).
2. Zhao G. (2007), *Polarons in Colossal Magnetoresistive and High-Temperature Superconducting Materials*. In: Alexandrov A.S. (eds) *Polarons in Advanced Materials*. Springer Series in Materials Science, vol. **103**. Springer, Dordrecht. (https://doi.org/10.1007/978-1-4020-6348-0_14).
3. G. M. Zhao, K. Conder, H. Keller and K. A. Muller, *Nature*. **381**, 676 (1996).
4. G. M. Zhao, H. Keller, J. Hofer, A. Shengelaya, and K. A. Muller, *Solid State Commun*. **104**, 57 (1997).
5. L. Malavasi and G. Flor, *J. Phys. Chem B.* **107(50)**, 13880 (2003).
6. H. Zhang, X. Yao and X. H. Zeng, *Phys. Stat. Sal.(a)201*. **10**, 2305 (2004).
7. K. Yamamoto, B. M. Lairson, J. C. Bravman and T. H. Geballe, *J. Appl. Phys*. **69**, 7189 (1991).
8. S. Kittelberger, O. M. Stoll and R. P. Huebener, *Supercond. Sci. Technol*. **11**,744 (1998).
9. K. N. Tu, N. C. Yeh, S. I. Park and C. C. Tsuei, *Phys. Rev. B.* **39**, 1 (1989).
10. V. Pralong, V. Caignaert, S. Hebert, C. Marinescu, B. Raveau and A. Maignan, *Solid State Ionics*. **177**, 815 (2006).
11. M. D. Carvalho, A. Wattiaux, J. M. Bassat J. C. Grenier, M. Pouchard, M. I. da Silva Pereira and F. M. A. Costa, *J Solid State Electrochem*. **7**, 700 (2003).
12. H. H. Feng, Z. G. Li, P. H. Hor, S. Bhavaraju, J. F. Di- Carlo and A. J. Jacobson, *Phys. Rev. B, (Rapid communications)*. **51**, 22 (1995).
13. Putul Malla Chowdhury, Barnali Ghosh, A. K. Raychaudhuri and S. D. Kaushik, *Journal of Nanoparticle Research*. **15**, 1585 (2013).
14. R. Shiozaki, K. Takenaka, Y. Sawaki and S. Sugai, *Phys. Rev. B.* **63**, 184419 (2001).
15. Arindam Ghosh and A. K. Raychaudhuri, *Phys. Rev. B.* **64**,104304 (2001).
16. Jean Pierre Locquet, Frederic Arrouy, Erich Macheer, Michel Despont, Peter Bauer and Erica J Williams, *Appl. Phys. Lett*. **68**, 14 (1996).
17. Jean Pierre Locquet, *Physica C*. **263**,160 (1996).